High Fidelity Simulation of Loss Mechanisms in Compressors

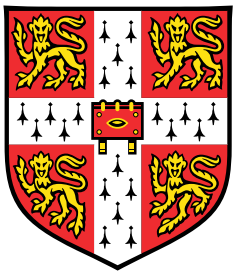

Pawel Przytarski

Whittle Laboratory
Department of Engineering
University of Cambridge

This dissertation is submitted for the degree of
Doctor of Philosophy

Darwin College

September 2020

This thesis is dedicated to my parents
Włodzimierz and Barbara

Declaration

This thesis is the result of my own work and includes nothing which is the outcome of work done in collaboration except as declared in the Preface and specified in the text. I further state that no substantial part of my thesis has already been submitted, or, is being concurrently submitted for any such degree, diploma or other qualification at the University of Cambridge or any other University or similar institution except as declared in the Preface and specified in the text. It does not exceed the prescribed word limit for the relevant Degree Committee.

The work contained within this thesis has, to date, produced the following publications:

Przytarski & Wheeler (2019). The effect of rotor-stator gap on compressor performance, ASME Turbo Expo 2019. Paper no. GT2019-91007 (in J. of Turbomachinery)

Przytarski & Wheeler (2018). Accurate Prediction of Loss Using High Fidelity Methods, ASME Turbo Expo 2018. Paper no. GT2018-77125 (in J. of Turbomachinery)

Pawel Przytarski
September 2020

Abstract

High Fidelity Simulation of Loss Mechanisms in Compressors

Pawel Przytarski

Further improvements in aero-engine efficiencies require better understanding of loss mechanisms. The rise of high performance computing is unlocking the potential of scale-resolving simulations for industrially relevant cases thus allowing new levels of simulation fidelity. As a result, previously unexplored effects of unsteadiness can be simulated and their impact on loss understood. The work undertaken in this thesis aims to establish a framework for accurate loss predictions using scale-resolving simulations and inform the field with regards to the effects of unsteadiness on loss mechanisms within the multi-stage compressors.

The lack of computational requirements for accurate industrial simulations lead to inconsistent loss predictions even for scale-resolving simulations depending on the chosen convergence criteria. This work studies aspects of loss generation by employing two test-cases: Taylor-Green vortex and compressor cascade subjected to freestream turbulence. The results show that both resolving local entropy generation rate and capturing the inception and growth of instabilities are critical to accuracy of loss prediction. In particular, the interaction of free-stream turbulence at the leading-edge and development of instabilities in the laminar region of the boundary layer are found to be important. These two outcomes allow for a formulation of resolution criteria that ensure accurate loss predictions for compressor flows.

One of the major sources of uncertainty in the current simulation methods for compressor flows is the level of unsteadiness and its impact on loss This work makes a series of steps towards understanding the nature and the origin of unsteadiness within multi-stage machines and investiages the impact of gapping on mid-span compressor loss. It is found that freestream turbulence levels rise significantly as the size of the rotor-stator

axial gap is reduced. This is because of the effect of axial gap on turbulence production mechanisms, which amplify at smaller axial gaps and drive increases in dissipation and loss. This effect is found to raise loss by between 5.5 - 9.5% over the range of conditions tested here. This effect was found to significantly outweigh the beneficial effects of wake recovery on loss.

Acknowledgements

First of all I would like to express my deepest gratitude to my supervisor Dr Andy Wheeler. I am thankful for his guidance and continued support. This work would have not been possible without his unwavering commitment and help which went above and beyond anything I could expect. His expertise, critical thinking and valuable insights into the research problems are greatly appreciated.

To all the Whittle Laboratory members for creating the most welcoming and open atmosphere. It was pleasure to work and share these years with you. In particular thanks to all the people within the second CDT cohort for making the first year in Cambridge so memorable.

Financial support for this work was provided by the Whittle Laboratory and the University of Cambridge through the Denton Scholarship fund and the CDT in Gas Turbine Aerodynamics, funded by the EPSRC $EP/L015943/1$. I would also like to acknowledge the help of UK Turbulence Consortium funded by the EPSRC grant $EP/L000261/1$ and Cambridge Service for Data Driven Discovery system operated by the University of Cambridge Research Computing Service funded by EPSRC Tier-2 grant $EP/P020259/1$, whose HPC allocations have been used to obtain the results. Parts of this work were also performed under the Project HPC-EUROPA3 (INFRAIA-2016-1-730897), with the support of the EC Research Innovation Action under the H2020 Programme; in particular, I would like to gratefully acknowledge the support of Dr Davide Lengani from the University of Genova.

On a personal level, I would like to thank all my friends that made my stay in Cambridge fun and unforgettable experience. Special mention to my amazing housemates Krish and Lachlan and the rest of the CDT gang Hans, Michael and David; to Darbar buddies Josh, Slava, Piotr and Aljaz; to CUATS committee Marcin, David and Adam; and many others I forgot to mention. Last but not least, special thanks to lovely Chiara for making Cambridge that much more special. Thank you all.

Table of contents

List of figures **xv**

List of tables **xxi**

Nomenclature **xxiii**

1 Introduction **1**
1.1 Motivation 1
1.2 Outline 4

2 Literature Review **7**
2.1 The rise of high-fidelity studies 7
2.2 Ovierview of high-fidelity studies for turbomachinery 10
2.2.1 Low Pressure Turbine studies 10
2.2.2 High Pressure Turbine studies 20
2.2.3 Compressor studies 24
2.3 Resolution considerations for scale-resolving simulations 33
2.4 Multi-stage environment 36
2.5 Concluding remarks 38

3 Computational Methods **41**
3.1 Summary of 3DNS solver 41
3.1.1 Dissipation considerations 42
3.1.2 Dispersion considerations 43
3.1.3 Aliasing considerations 44
3.1.4 Boundary schemes 45
3.1.5 Grid metrics 45
3.2 Boundary conditions 47
3.3 Inflow turbulence 52

3.4 Repeating passage model 53
3.4.1 Variation in axial gap 55
3.4.2 Wake recycling 55
3.4.3 Verification of repeating-stage condition 56

4 Accurate Loss Accounting **59**
4.1 Computational setup 59
4.2 Loss accounting using entropy generation rate 61
4.3 The effect of resolution on entropy generation rate 63
4.4 Resolution requirements for accurate entropy generation rate prediction 65
4.5 Conclusions 68

5 Compressor Cascade Loss Prediction **71**
5.1 Computational setup 71
5.2 Loss audit 75
5.3 The effect of mesh resolution on transition 76
5.4 The effect of mesh resolution on dissipation coefficient 77
5.5 The effect of mesh resolution on flow structure 81
5.6 Conclusions 84

6 Unsteady Energy Transfers in Compressors **87**
6.1 Computational setup 87
6.2 Loss summary 89
6.3 Triple decomposition of kinetic energy 90
6.4 Loss accounting 94
6.5 Energy transfer rate terms 94
6.5.1 Mean to turbulent energy transfer 95
6.5.2 Mean to periodic energy transfer 96
6.5.3 Periodic to turbulent energy transfer 97
6.6 Conclusions 97

7 Multi-Stage Compressor Loss Mechanisms - The Effect of Gapping 101
7.1 Computational setup 101
7.2 The effect of axial gap on unsteadiness 104
7.3 The effect of axial gap on loss 107
7.4 The role of turbulence production on loss 107
7.5 The effect of axial gap on wake recovery 115
7.6 Multi-stage feedback effect on turbulence production 117

7.7 Conclusions 118

8 Conclusions and Recommendations for Future Work 121
8.1 Conclusions 121
8.1.1 Accurate prediction of loss using high fidelity methods 121
8.1.2 Unsteadiness in multi-stage compressors 122
8.2 Recommendations for future work 123

Bibliography 127

Appendix A 137
A.1 Double decomposition of kinetic energy 137

List of figures

1.1 Sketch of turbulence spectrum with approximate resolution that various modelling techniques aspire to (adapted from [87]) 2
1.2 Example multi-stage turbomachinery flowfield 3

2.1 Overview of unsteady flow phenomena in turbomachinery along with limitations inherent in (U)RANS modelling approaches. Taken from Gourdain et al. [38], originally from Hodson [43]. 9
2.2 Reynolds number variation through a medium-sized gas turbine engine, from Mayle [58]. 11
2.3 Evolution of wake-induced longitudinal streaks, u': (a) intermediate-strength disturbance and strong forcing; (b) intermediate-strength disturbance and weak forcing; (c) intermediate-strength disturbance with downstream strong forcing; from [120]. 12
2.4 Schematic of the flow inside a low preesure turbine passage, from Durbin [27]. 13
2.5 Instantaneous isosurface of vorticity at four wake locations for inflow wakes from (a) 2D precursor cylinder bar simulation and (b) 3D precursor cylinder bar simulation, from Sarkar [89]. 15
2.6 Instantaneous flowfields for (a) clean inflow case, (b) clean inflow with purge flow, (c) inflow with periodic wakes and purge flow, from Cui and Tucker [20]. 17
2.7 Instantaneous z-vorticity contours in the mid-span for a range of reduced frequencies: 0, 0.31, 0.61 and 1.22, from Michelassi et al. [63]. 20
2.8 Instantaneous snapshots of HPT flow showing presence of (a) upstream moving pressure waves, (b) development of 2d spanwise instabilities over the aft suction surface, (c) fluctuations in surface heat flux due to pressure wave reflections, and (d) near-wall streaks, from Wheeler et al. [110]. 22

2.9 Instantaneous snapshots showing vortical structures on suction side for various freestream turbulence levels and turbulence lengthscales, (a) $Tu = 6.5\%, Ls = 5\%$, (b) $Tu = 6.5\%, Ls = 20\%$, (c) $Tu = 20\%, Ls = 5\%$, (d) $Tu = 20\%, Ls = 20\%$, from Zhao and Sandberg [130]. 23
2.10 Schematic of a transonic tip flow, from Wheeler and Sandberg [109]. . . 24
2.11 Schematic of boundary layer states on a compressor blade suction surface (a) and plots of turbulence production and dissipation coefficient (b), from Wheeler et al. [113]. 26
2.12 Contours of phase averaged kinetic energy at four wake phases, from Zaki et al. [126]. 27
2.13 Instantaneous tangential velocity fluctuations inside the suction side boundary layer at four wake locations for the case with strong wakes with arrows identify the locations of boundary layer separation (S) and reattachment (R), from Wissink et al. [114]. 28
2.14 Stall indicator vs diffusion parameter map, from Lei et al. [55]. 29
2.15 Instantaneous snapshots showing vortical structures on: (a) suction surface and (b) pressure surface, from Scillitoe et al. [92]. 30
2.16 Vortical structures obtained from time-averaged flow field, from You et al. [122]. 31
2.17 Instantaneous flow field close to the casing shaded with density gradient, from Gourdain [35]. 32
2.18 Instantaneous z-vorticity contours for (a) negative incidence case, (b) positive incidence case and (c) wake case, from Leggett et al. [54]. . . . 34

3.1 Dispersive properties of central finite difference schemes (left) and transfer functions of filtering schemes (right). 42
3.2 The effect of skew-symmtric splitting treatment on Taylor-Green vortex spherical spectrum. 44
3.3 Mapping between physical an dcomputational domain, from Pulliam and Steger [84]. 45
3.4 Inlet and outlet boundary conditions, and respective characteristic waves, from Poinsot and Lele [82]. 48
3.5 The effect of improved inlet characteristic boundary conditions on static pressure field, Poinsot and Lele [82] formulation. 50
3.6 The effect of improved inlet characteristic boundary conditions on static pressure field, Odier et a. [74] formulation. 51

3.7 Iso-surfaces of Q-criterion of compressor flow with inflow turbulence for representative geometry, from Wheeler et al. [113] 52
3.8 Schematic of the computational domain and wake recycling procedure. 53
3.9 Example performance of the wake recycling procedure using different number of Fourier modes. 54
3.10 Comparison of NACA65 instantaneous disturbance velocity profile (upper) and ensemble average turbulence intensity (lower) at the inlet and at the sampling plance of the domain for the NACA65 testcase with axial gap of $0.40C_{ax}$. 55
3.11 Comparison of ensemble averaged turbulence intensity evolution in the axial direction between the outlet and the inlet for the NACA65 testcase with axial gap of $0.40C_{ax}$. 56

4.1 Evolution of iso-surfaces of Q-criterion ($Q = 0.1(u_0/L)^2$) colored with the non-dimensional velocity magnitude u/u_{max}. The solution has been computed with the 8^{th} order scheme on the 128^3 grid using 3DNS. . . . 60
4.2 Comparison of volume averaged enstrophy (left) and energy spectra at $t = 9$ (right) between 3DNS and spectral solution [106]. 61
4.3 Evolution of Taylor-Green vortex from initial flowfield to the mixed-out state and associated loss generation rate. 63
4.4 The effect of resolution on Taylor-Green vortex dissipation (left) and entropy generation rate (right). 64
4.5 The effect of finite difference and filtering order on Taylor-Green vortex dissipation (left) and entropy generation rate (right). 65
4.6 Defintion of path error, L_1, i.e. deviation of entropy generation rate from the reference solution (left) and cut-off wavenumber, $k_{cut-off}$ based on dissipation spectra at $t^* = 9$ (peak entropy generation rate) defined as the smallest wavenumber for which dissipation is lower than 50% of the reference dissipation (right). 67
4.7 Path error, L_1, vs. cut-off wavelength, $k_{cut-off}$ for a range of numerical schemes and mesh resolutions for Taylor-Green vortex case. 68

5.1 Block structure and example mesh showing every 8^{th} grid line (for 73M mesh). 72
5.2 Comparison of turbulence intensity at the midpitch between 3DNS and reference solution, [127]. 73

5.3 Comparison of predicted pressure loading coefficient for three mesh sizes and and reference solution, [127]: top $Tu = 4\%$; bottom $Tu = 6\%$ . . . 74
5.4 Comparison of cell size with Kolmogorov lengthscale at peak entropy generation rate region for $102M$ mesh. 75
5.5 The effect of resolution on loss prediction. 77
5.6 Breakdown of loss with regards to different regions of the flow. 78
5.7 The effect of resolution on skin friction for $Tu_{in} = 4\%$ (left) and $Tu_{in} = 6\%$ (right). 79
5.8 The effect of resolution on dissipation coefficient (left) and turbulence production (right) in the boundary layer on the suction side for $Tu = 6\%$. 80
5.9 The effect of resolution on dissipation coefficient (left) and production (right) in the boundary layer on the turbulence pressure side for $Tu = 6\%$. 81
5.10 Suction surface (left) and pressre surface (right) flow structures indicated by yellow-colored iso-surfaces of Q-criterion $= 1 \times 10^8 s^{-2}$, iso-surface of instantaneous turbulence production $\Pi(t) = 5 \times 10^4$ colored by streamwise velocity fluctuation u' and surface shear stress for the $Tu = 6\%$ case. 82
5.11 The effect of resolution on leading edge streaks. 83
5.12 The importance of the leading edge and laminar region on accurate prediction of loss mechanisms. 84

6.1 Mesh used for this study showing every 8^{th} grid line. 88
6.2 Instantaneous spanwise vorticity flowfield of a stator row of a repeating-passage simulation for the NACA65 blade profile. 89
6.3 The comparison of integrated turbulent dissipation ($\Phi_f + \epsilon_N$) and energy transfer terms ($\mathcal{T}_{mf} + \mathcal{T}_{of}$) for three considered gaps. 93
6.4 Domain split for NACA65 testcase. 95
6.5 Time- and phase-averaged energy transfer rate between the mean and turbulent flowfield: $t_{mf} = -\overline{\rho u_i' u_j'} \frac{\partial \bar{u}_i}{\partial x_j}$ 96
6.6 Time- and phase-averaged energy transfer rate between the mean and periodic flowfield: $t_{mo} = -\overline{\rho u_i^* u_j^*} \frac{\partial \bar{u}_i}{\partial x_j}$ 97
6.7 Time- and phase-averaged energy transfer rate between the periodic and turbulent flowfield: $t_{of} = -\overline{\left\langle \rho u_i' u_j' \right\rangle} \frac{\partial u_i^*}{\partial x_j}$ 98

7.1 Loading distributions for the NACA65 (left) and the CDA profiles (right) 103
7.2 Mesh used for this study showing every 8^{th} grid line. 104

7.3 Instantaneous spanwise vorticity flowfield of a stator row of a repeating-passage simulation for the NACA65 and CDA blade profiles. 105
7.4 Velocity trace (upper) from the inlet freestream probe of NACA65 blade at two different gaps (0.3 and $0.4C_{ax}$) and associated Fourier spectrum of the signal (lower). 106
7.5 Comparison of decomposed periodic and turbulent unsteadiness for both NACA65 and CDA testcases showing increase in both as the gap is reduced. 107
7.6 Variation of loss coefficient (left) and turbulence production coefficient (right) with axial gap. 108
7.7 Contribution to turbulence production coefficient from the boundary layers and freestream for NACA65 testcase. 109
7.8 Spacetime diagram of shear stress of suction surface for all the axial gaps. Region of separated flow is outlined with a zero velocity contour (green). 110
7.9 The effect of separation bubble on turbulence production. 111
7.10 Wake boundary layer interaction increases as the gap is reduced resulting in creation of turbulent spots. 112
7.11 Turbulence production contours (upper) and vectors of principle strain (black) and principle stress (red) components (lower) at one of the rotor phases for $g_{ax} = 0.30C_{ax}$ (left) and $g_{ax} = 0.40C_{ax}$ gaps. 114
7.12 Variation of wake dissipation coefficient for NACA65 testcase. 115
7.13 The profile of wake turbulence intensity on the plane located $0.15C_{ax}$ downstream of the trailing edge for NACA65 testcase for all three gaps. 116
7.14 The comparison of loss change for NACA65 and CDA testcases due to wake recovery (green) and turbulence production (red) as the gap is reduced from 0.40 to$0.30C_{ax}$. 118
7.15 Multi-stage feedback mechanism resulting in higher turbulence production as the gap is reduced. 119

A.1 The comparison of integrated turbulent dissipation ($\Phi_f + \epsilon_N$) and energy transfer term ($\mathcal{T}_{mf}$) for three considered gaps. 139

List of tables

3.1 Points-per-wavelength for various FD schemes. 43

5.1 Test cases 72
5.2 Maximum cell size to Kolmogorov length-scale ratio Δ/η_{Kol} for suction and pressure side 76

6.1 Maximum near-wall viscous units 88
6.2 Comparison between resolved and unresolved dissipation 90
6.3 Breakdown of integrated transfer rates for a $g_a x = 0.40 C_{ax}$ gap case . . 95
6.4 Triple decomposition - mean kinetic energy budget 99
6.5 Triple decomposition - oscillating kinetic energy budget 99
6.6 Triple decomposition - fluctuating kinetic energy budget 100

7.1 Test-case details 102
7.2 Maximum near-wall viscous units 103

A.1 Double decomposition - mean kinetic energy budget 139
A.2 Double decomposition - turbulent kinetic energy budget 140

Nomenclature

Roman Symbols

C	Integrated convection of kinetic energy
c	Convection of kinetic energy
C_{ax}	Axial chord
c_d	Dissipation coefficient
c_f	Skin friction coefficient
C_p	Pressure coefficient
D	Integrated diffusion due to unsteadiness
d	Diffusion due to unsteadiness
D_k	Spherical dissipation spectra
E_k	Spherical energy spectra
F_{red}	Reduced frequency
F_{rotor}	Wake passing frequency
g_{ax}	Axial gap
k	Wavenumber
$k_{cut-off}$	Cut-off wavenumber
k'	Turbulent kinetic energy
L_1	Path error

Ma	Mach number
$\mathcal{L}$	Characteristic wave
$\dot{m}$	Mass flow rate
p	Static pressure
$P.D.$	Integrated pressure diffusion
$p.d.$	Pressure diffusion
$p.l.$	Integrated pressure dilation
$p.l.$	Pressure dilation
p_o	Stagnation pressure
Pr	Integrated Turbulence production within boundary layer
Pu	Periodic intensity
$P.W.$	Integrated pressure work
$p.w.$	Pressure work
$\rho Dx/Dt$	Material derivative of variable x
Re	Reynolds number
R_{ij}	Reynolds stress tensor
s	Entropy
S_{ij}	Strain-rate tensor
T	Static temperature
t	Time
$\mathcal{T}_{mf}$	Integrated energy transfer between mean and fluctuating flowfield
t_{mf}	Energy transfer between mean and fluctuating flowfield
$\mathcal{T}_{mo}$	Integrated energy transfer between mean and oscillating flowfield
t_{mo}	Energy transfer between mean and oscillating flowfield

T_o Stagnation temperature

$\mathcal{T}_{of}$ Integrated energy transfer between oscillating and fluctuating flowfield

t_{of} Energy transfer between oscillating and fluctuating flowfield

t^* Non-dimensional time

Tu Turbulence intensity

U_e Boundary layer edge velocity

U_{ref} Reference velocity

u, v, w Instantaneous velocity components in the x, y, z directions

$V.D.$ Integrated viscous diffusion

$v.d.$ Viscous diffusion

x Axial distance

Greek Symbols

α_{in} Inlet flow angle

Δ Cell size

δ Boundary layer thickness

δ^* Boundary layer momentum thickness

$\Delta_n^+, \Delta_t^+, \Delta_z^+$ Viscous wall units in in the x, y, z directions

ζ Enstrophy

ϵ_N Integrated artificial dissipation

ϵ_Φ Integrated dissipation function

ϵ_S Integrated entropy generation rate

k_{Kol} Kolmogorov wavenumber

λ Lengthscale

Λ Stage reaction

η_{Kol}	Kolmogorov lengthscale
λ_{opt}	Optimal disturbance lengthscale
μ	Dynamic viscosity
ν	Kinematic viscosity
Ω	Computational domain
ω	Vorticity
ϕ	Viscous dissipation $\tau_{ij}\frac{\partial u_i}{\partial x_j}$
ϕ_{flow}	Flow coefficient
$\Pi(t)$	Instantaneous turbulence production
ψ	Principle turbulent stress angle
ψ_{work}	Loading coefficient
ρ	Density
θ	Principle strain-rate angle
ξ	Entropy loss coefficient

Subscripts

$1, 2, 3$	Correspond to x, y, z directions
f	Fluctuating turbulent flowfield
in	Inflow conditions
m	Mean flowfield
o	Oscillating periodic flowfield
out	Outflow conditions

Other Symbols

$\bar{f}$	Time-averaged component of f
$\langle f \rangle$	Ensemble average of f

f' Fluctuating component of f

f^* Oscillating component of f

Acronyms / Abbreviations

CDA Leading edge

CFD Computational Fluid Dynamics

DNS Direct Numerical Simulation

DRP Dispersion-relation-preserving

FD Finite difference

HP High Pressure

HPT High Pressure Turbine

LE Leading edge

LES Large Eddy Simulation

LP Low Pressure

LPT Low Pressure Turbine

PPW Points-per-wavelength

PS Pressure surface

RANS Reynolds-Averaged Navier-Stokes

SAT Simultaneous approximation term

SBP Summation-by-parts

SS Suction surface

TE Trailing edge

URANS Unsteady Reynolds-Averaged Navier-Stokes

Chapter 1

Introduction

1.1 Motivation

Turbomachinery flows feature complex interactions between stationary and rotating blades coupled with high freestream turbulence effects. These lead to a wide range of unsteady turbulent phenomena such as separations, mixing, laminar-to-turbulent transition, flow reattachment, etc. Figure 1.1 shows a sketch of turbulence spectrum with turbulence model type as a function of cut-off frequency. Standard modelling techniques such as Steady/Unsteady Reynolds-Averaged Navier-Stokes simulations (RANS/URANS) are unfit to reliably capture these effects as the scales occupied by periodic and unsteady disturbances are mostly modeled and their dynamics are lost. Despite their inherent limitation these methods are a workhorse for design and validation of current engine designs, Slotnick et al. [94] . However, unsteadiness can plays a major role in determining the performance and becomes ever more important as engines are moving towards more compact designs that require higher loadings and shorter inter-row distances, Tyacke et al. [104] . In fact, current design trends often render methods such as URANS inappropriate due to a lack of spectral gap between deterministic and stochastic unsteadiness, Sandberg and Michelassi [87] .

Understanding flow physics in turbomachinery flows is key to unlocking further efficiency improvements in technologies such as aero-engines and gas turbines. These technologies play a major role in decarbonisation of propulsion and power generation required for a sustainable growth. This is emphasized by emission targets on civil turbofan engines set by, e.g. The EU Flightpath 2050 report, [18]. However, realizing further improvements in efficiency comes hard due to the current aerodesign maturity. Modelling uncertainties present in (U)RANS simulations render gains of an order of

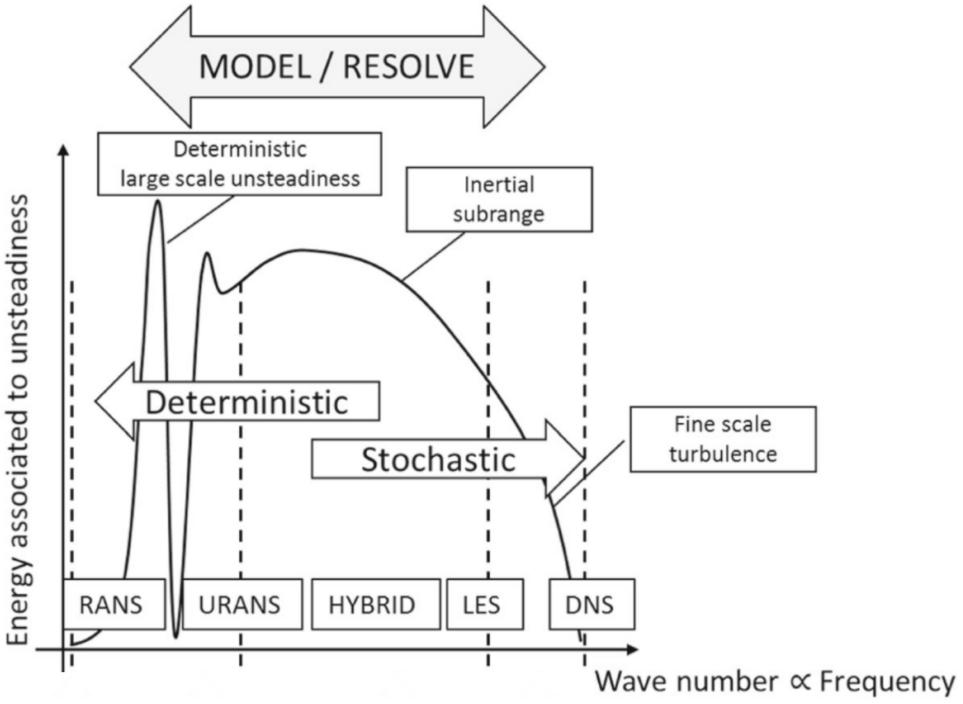

Figure 1.1: Sketch of turbulence spectrum with approximate resolution that various modelling techniques aspire to (adapted from [87])

0.1-1% elusive. To realize these goals, extremely accurate high-fidelity computational fluid dynamic (CFD) simulations are required such as Large Eddy Simulations (LES) or Direct Numerical Simulations (DNS), [87]. These simulations aim to resolve a part or an entire turbulence spectrum to capture the flow dynamics and will be referred to as scale-resolving simulations.

Up to now scale-resolving methods which minimize modelling uncertainties have been prohibitively expensive. The advent of high performance computing clusters is now unlocking the potential of parallel scale resolving simulations for industrially relevant cases. As a result, there is now a potential to achieve new levels of simulation fidelity and accuracy. This resulted in proliferation of high-fidelity studies providing invaluable insight into certain physical mechanisms, but the simulation cost still remains too high for scale-resolving simulations to be used as a design tool, [94]. Consequently, high-fidelity studies have been poised as a replacement or complimentary to the experimental studies for industrial flows. When their potential as virtual experiments is realized the insights offered through the scale-resolving simulations promise further improvements in gas turbine efficiencies which are key to reducing the environmental impact of aviation and power generation.

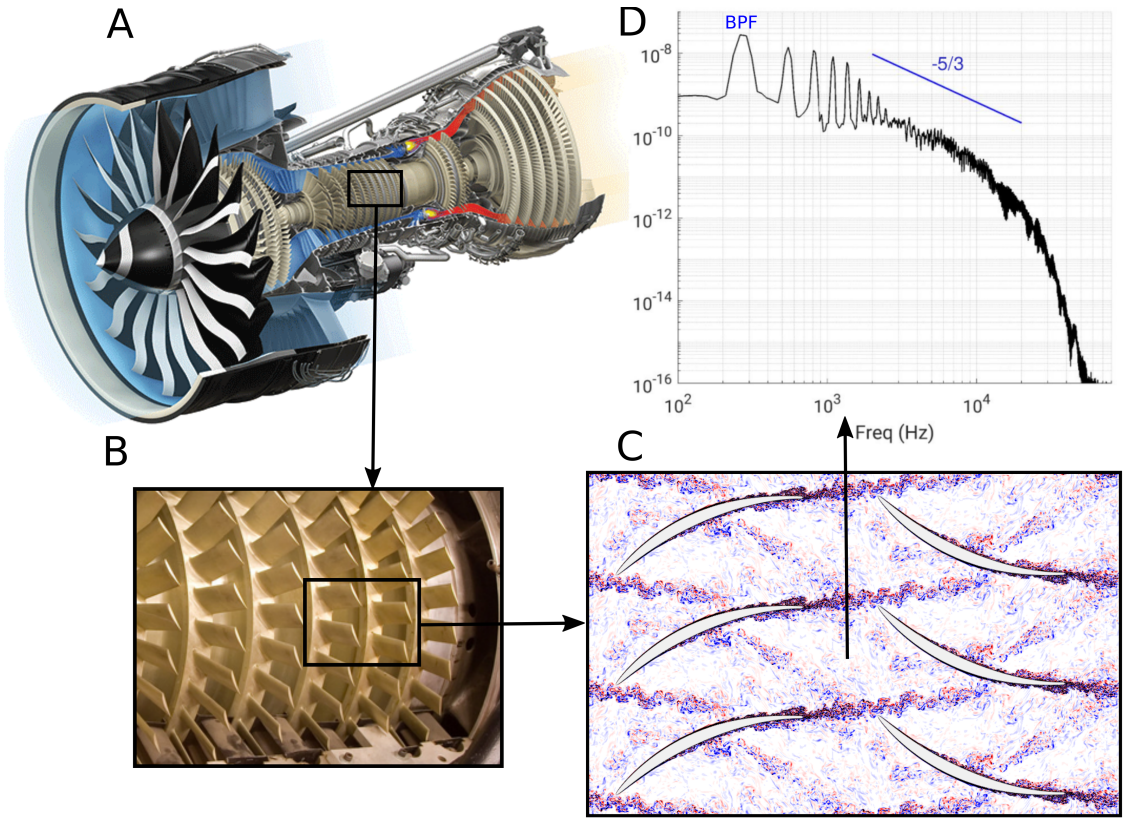

Figure 1.2: Example multi-stage turbomachinery flowfield

One area that is expected to benefit from the high-fidelity simulations and inform industrial practice are compressor flow aerodynamics. Compressors play a vital role in gas turbines and their stability and efficiency are critical to safe and sustainable operation. Subject to adverse pressure gradients they are prone to instabilities such as surge and rotating stall which limit their performance. On the other hand, their efficiency has large effect on the entire machine as 1% of compressor adiabatic efficiency can be worth 0.5% of cycle efficiency. Majority of the losses in compressors i.e. over 80% are also generated in the proximity of the boundary layers, [87]. As standard modelling techniques are not equipped to capture the full complexity of the compressor flows, scale-resolving simulations can open new avenues for efficiency improvements and help decrease flow uncertainty to allow for smaller compressor safety margins with regards to its operability. While the LES of multi-stage compressor at engine representative conditions remain unrealistic until 2035 as noted by Gourdain et al. [38], current HPC capabilities allow for compressor flow simulations at conditions approaching engine conditions for simplified or idealized test-cases.

One of the major sources of uncertainty in the current simulation methods with regards to compressor flows is the level of unsteadiness. As mentioned before, this becomes ever more important as designs become more compact. Figure 1.2 shows an example of a multistage compressor along with an example mid-span flowfield and resulting freestream turbulence spectrum from simulation performed for this thesis. It can be seen that the unsteadiness has both deterministic and stochastic contributions. The former unsteadiness is driven by the stator-rotor interactions due to convecting upstream wakes. The latter is turbulence driven and its origin and nature is less understood. What is even less understood is their interaction and its effect on flow irreversibilities and thus loss. Including effects of unsteadiness can have significant implications on predictive capabilities of models, especially with regard to compressor flows as demonstrated by Montomoli et al. [69].

The objective of this work is to investigate compressor flows at industrially relevant conditions using high-fidelity simulations. This will be done with a focus on unsteadiness and its effect on loss mechanisms. The study aims to establish a framework for accurate loss predictions using scale-resolving simulations for compressors and inform the field with regards to the effects of unsteadiness within the multi-stage compressors.

1.2 Outline

The thesis starts with the overview of relevant literature in Chapter 2. This includes the overview of high-fidelity simulation studies for turbomachinery flows, resolution considerations for scale-resolving simulations as well as a discussion of aspects of multi-stage compressor flowfield relevant to this work. Chapter 3 introduces computational methods used in the thesis, specifically with regards to the in-house solver. Chapters 4-7 discuss the studies carried out for the purpose of the thesis and present the findings.

Chapter 4 starts from the introduction of loss accounting methodology based on the entropy generation rate. This methodology is validated on Taylor-Green vortex canonical test-case and used throughout the thesis. Results from this study allow to assess the performance of various low- and high-order numerical schemes and their effect on the flow field. Consequently, resolution criteria ensuring correct entropy generation rate are demonstrated.

In Chapter 5 the effect of flow physics on loss generation is investigated by using a transitional $NACA65$ compressor cascade subjected to freestream turbulence (stochastic unsteadiness). Here, the effect of freestream turbulence on boundary layer is of utmost importance and its effect on entropy generation rate is studied.

In Chapter 6 a novel method able to mimic the multi-stage compressor environment is used to recreate the inflow condition observed by an embedded blade-row. This is done for $NACA65$ blade geometry at identical conditions as in Chapter 5, but now also including the effect of deterministic unsteadiness (wakes). The sources of loss are are identified by computing the kinetic energy transport equation budgets.

Chapter 7 examines the effect of gapping on loss at realistic multi-stage conditions. This is done using previously studied $NACA65$ geometry and modern Controlled Diffusion Airfoil (CDA) geometry at three different axial gaps. The results show how gap affects unsteadiness within the machine and affects its performance.

In the final chapter, conclusions and recommendations for future work are given. The results are important in particular with regards to resolution requirements for accurate loss predictions for turbomachinery flows and understanding of the role of unsteadiness in loss generation.

.

Chapter 2

Literature Review

2.1 The rise of high-fidelity studies

Computational Fluid Dynamics (CFD) simulations are central in aiding turbomachinery design. These methods evolved heavily from throughflow calculations and inviscid 2D blade to blade calculations developed in 1960's to 3D unsteady RANS multistage computations in 2000's. As fidelity of these methods increased, the need for expensive experimental testing decreased. One common example of this is given by Fischberg et al. [30] who reported that the use of RANS in new compressor design brought $37M of savings in reduced testing alone. More generally, according to the US Department of Energy, the rapid development of CFD helped reducing the reliance on high-pressure rig testing required for engine certification by 50% at Pratt&Whitney between 1980's and 1990's, [105]. Despite CFD's overall positive impact on the industry, its benefits have not come easy. The impact of the initial push for reduced physical testing and overly high confidence in early CFD predictions had catastrophic consequences for PW6000 programme, Bowen [8]. The Pratt&Whitney designed engine turned out not to meet the fuel consumptions targets forcing the company to replace high pressure compressor and re-certify the engine leading to millions of dollars in losses. This example serves as a cautionary tale and highlights the risks of over-reliance on CFD in the design process.

As (U)RANS methodology matured, it became indispensable in the development of aero-engines and, together with 0D and 1D proprietary empirical correlations, formed a backbone of modern design systems, [53]. However, despite its prominence, CFD potential has not been realized yet and industry saw only moderate further reduction in required engine testing in the last two decades e.g. Pratt&Whitney reduced engine testing only by 10% between 2000's and 2010's, [105]. This has been credited to

many deficiencies of current modelling methodology that lead to higher modelling uncertainties than efficiency gains (of an order of 0.1% - 1%) pursued by the designers nowadays, [87]. Denton [25] discussed in detail various sources of error in CFD that limit its impact on turbomachinery design, however, one most singled out by various authors is turbulence modelling and its inability to capture turbulence physics, Moin [68], Sandberg and Michelassi [87].
Turbulence affects mixing, transition, separations, heat transfer, drag generation and many other processes and so plays a vital role in determining the performance and lifetime of turbomachinery components. As noted by Denton [25], reliable prediction of turbulent phenomena is critical for turbomachinery design, but turbulence modelling is notoriously difficult for turbomachinery applications due to the complex geometry, presence of curvature and strong pressure gradients. Turbulence modelling is further impacted by the complex physics driven by the flow unsteadiness within turbomachines. This unsteadiness is comprised of two components: deterministic (periodic) due to rotor-stator interactions and stochastic (chaotic) due to turbulence. Figure 2.1 shows an overview of unsteady phenomena in turbomachines and highlights (U)RANS limitations, especially with regards to capturing non-periodic behavior associated with turbulence.

Beyond (U)RANS inherent inability to directly represent turbulence, there are other factors that limit predictive capabilities of currently used methods even with regards to periodic phenomena, such as lack of validation of turbulence models for new configurations. As discussed by Tucker [103], even small-scale flow features can have profound effect on main gas path flow invalidating existing calibrations. Another limitations is related to the spectral gap required for the use of URANS. While it's able to capture large-scale unsteady interactions between the blades, it relies on the assumption of spectral gap, i.e. that deterministic (periodic) and stochastic (turbulent) unsteadiness occupies separate scales and there is limited interaction between them. This concept, which is described in detail by Tucker [102] and Michelassi [62], explains why turbulence models are unfit to deal even with the periodic flows within turbomachines. This issue is further exacerbated by the current design trends towards more compact machines with higher work coefficients meaning the interaction between deterministic and stochastic unsteadiness is unavoidable. In addition, errors caused by inaccurate accounting for this effect will compound when considering multi-stage environments. Thus, as stated by Sandberg and Michelassi [87], *"the greatest challenge for accurate simulations of main gas-path flows in turbomachinery is the presence of turbulence and its interaction with deterministic unsteadiness"*.

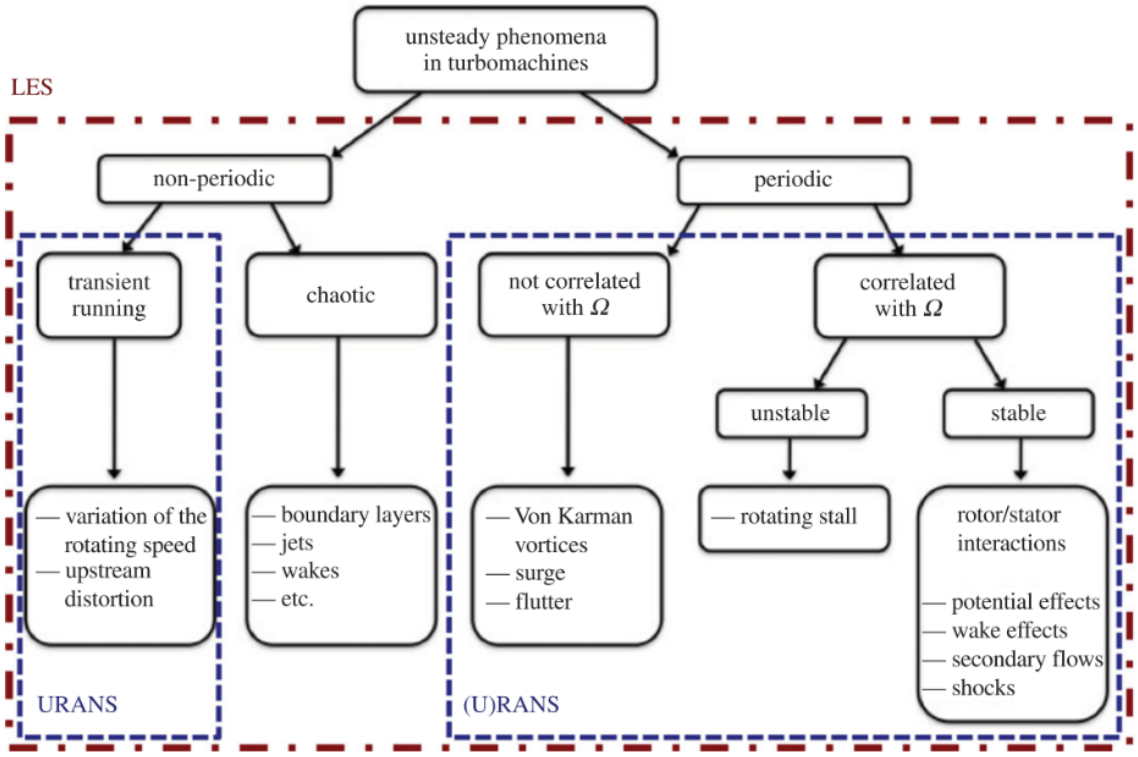

Figure 2.1: Overview of unsteady flow phenomena in turbomachinery along with limitations inherent in (U)RANS modelling approaches. Taken from Gourdain et al. [38], originally from Hodson [43].

As shown in Figure 2.1, scale resolving simulations such as LES or DNS can overcome problems with capturing chaotic turbulent behavior, but it comes at a high computational price. The exact cost depends on the running conditions and desired resolution, but estimates put the ratio of LES/DNS cost to RANS cost at between 100× for simplified geometries as reported by Laskowski et al. [53] to 10,000× for isolated compressor vane at Reynolds number of 10^6 and up to 1,000,000× for a compressor stage with full annulus as reported by Gourdain et al. [38]. With these estimates in mind, Gourdain et al. projects that LES for industrial compressors will not be available until 2035. To bridge the cost gap and unlock the potential of high-fidelity methods approaches such as hybrid methods or wall-modeled LES were suggested, Slotnick [94]. However, these methods suffer from similar modelling limitations as RANS, especially with regards to laminar-to-turbulent transition.

It is unlikely that universal turbulence model will be ever created, but, as noted by Denton [25], efficiency improvements can come through better understanding of flow physics when quantitative predictions are not available. This sort of physical understanding can be derived from the scale-resolving simulations. Despite their cost,

LES/DNS simulations can act as virtual experiments with an added benefit of a full access to three dimensional unsteady flow field data, thus opening new avenues for knowledge extraction and more physics driven development of low order models. Simulations of mid-span sections of the blades and isolated blades are already routinely done in academia and have been heavily used to inform the physics of e.g. transition, separation and mixing within turbomachines. However, questions remain with regard to what resolution is required to ensure correct physical behavior is captured, especially as scale-resolving simulations are known to be sensitive to grid resolution. There has been also little progress with reference to multi-blade and multi-row effects which are crucial for determining flow unsteadiness. Montomoli et al. [69] showed that including effects of unsteadiness can have significant implications on predictive capabilities of models.
In the next section overview of high-fidelity simulation use for turbomachinery applications is given. While not exhaustive, it shows a range of problems that were addressed using scale-resolving simulations. Later, resolution considerations regarding scale resolving simulations are discussed.

2.2 Ovierview of high-fidelity studies for turbomachinery

2.2.1 Low Pressure Turbine studies

As the cost of scale resolving simulation is strongly dependent on Reynolds number, high-fidelity studies initially focused on low-pressure turbine (LPT) flows. These flows are characterized by relatively low Reynolds numbers in a range of 5×10^4 to 5×10^5, [44], that are lower than Reynolds numbers experienced by other aero-engine components as shown in Figure 2.2. The low Reynolds numbers in LPT flows stem from low turbine air density and small aerofoil chord-sizes. As a consequence, these flows are prone to separations and accurate prediction of boundary layer state on the blade is key to limiting profile losses and improving LPT design. To aid this task early high-fidelity studies focused on understanding the mechanisms of transition on LPT blades and the effect of unsteadiness in determining the state of the boundary layer.

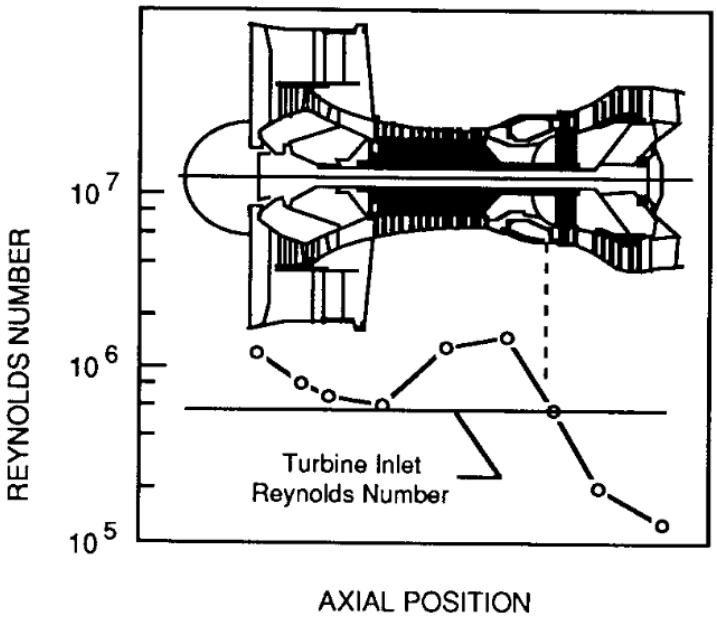

Figure 2.2: Reynolds number variation through a medium-sized gas turbine engine, from Mayle [58].

Flow physics

Wake-induced transition One of the earliest scale-resolving studies targeting turbomachinery aerodynamics was an incompressible DNS study of Wu et al. (1999) [120]. The authors of the study investigated an effect of periodic wakes on the developing laminar boundary layer on the flat plate and found that the wake-induced transition mechanism was similar to that of bypass transition. Notably, they observed the emergence of wake-induced longitudinal streaks (puffs) near the inlet of the domain. These streaks underwent either decay or led to a turbulent spots as shown in Figure 2.3. Their evolution depended on the initial streak strength and the amount of forcing due to wake eddies impinging on the boundary layer downstream of the streak inception. This work provided important insight into the wake-induced transition, however, the use of flat plate geometry and idealized freestream conditions meant that some critical effects were not taken into account such as curvature, variable pressure gradients or the interaction between the wakes and freestream turbulence.

Wu and Durbin (2001) [119] addressed some of these limitations by applying a similar incompressible DNS simulation to the T106 turbine cascade at $Re \approx 150k$ subjected to periodic cylinder wakes. They investigated how wakes interacted with the boundary layer and studied the inception of wake-induced turbulent spots. In

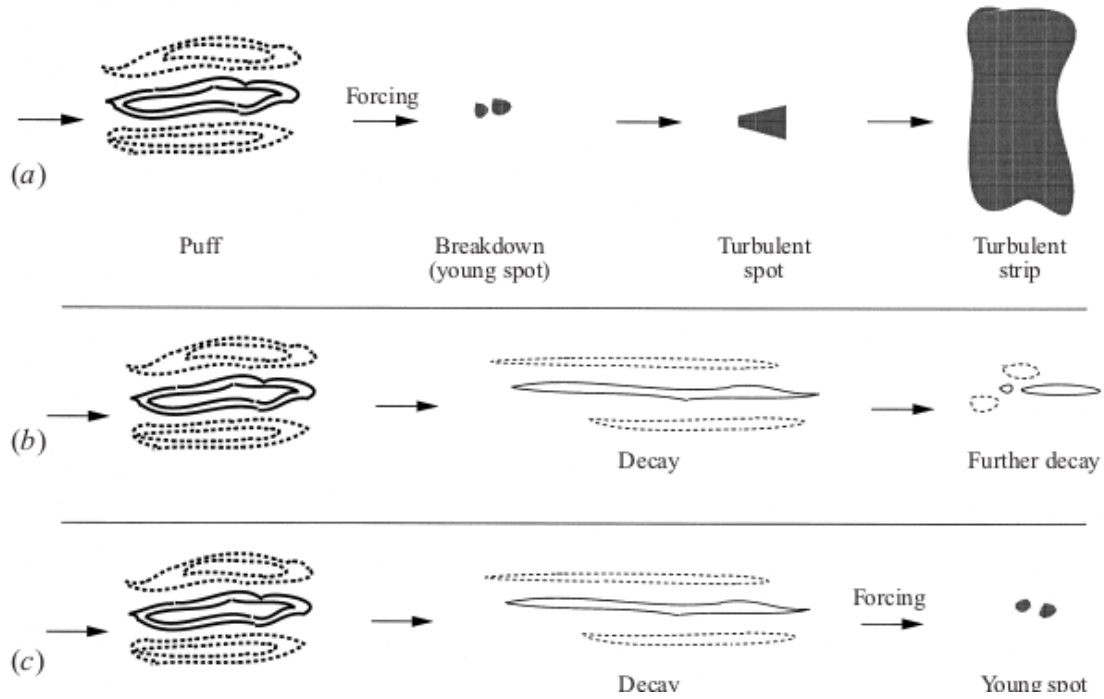

Figure 2.3: Evolution of wake-induced longitudinal streaks, u': (a) intermediate-strength disturbance and strong forcing; (b) intermediate-strength disturbance and weak forcing; (c) intermediate-strength disturbance with downstream strong forcing; from [120].

addition, they identified longitudinal streaks as primary drivers for laminar-to-turbulent transition on pressure surface. Those vortices came about as a result of irrotational strains acting on the wake in the freestream as it convects through the passage and drags over the blade pressure surface. This was of importance as previous studies, [98], showed that these streaks may result in higher heat transfer, thus offering a potential explanation for higher operating temperatures on pressure surfaces of high pressure turbine vanes which share similar flow physics with LPT cascades.

Wissink (2003) [115] also studied T106 turbine cascade subjected to periodic wakes, but at a lower Re of approximately $50k$. The author focused on the boundary layer separation on suction surface and the impact of incidence on flow stability. In the studied case, boundary layer on suction surface separated periodically and the author identified Kelvin-Helmholtz instability as responsible for separated flow transition and reattachment. The author also found that streaky structures were present on both pressure and suction side, however, they dissipated quickly on the latter at considered conditions.

Wissink and Rodi (2006), [116] extended that study by considering three different test

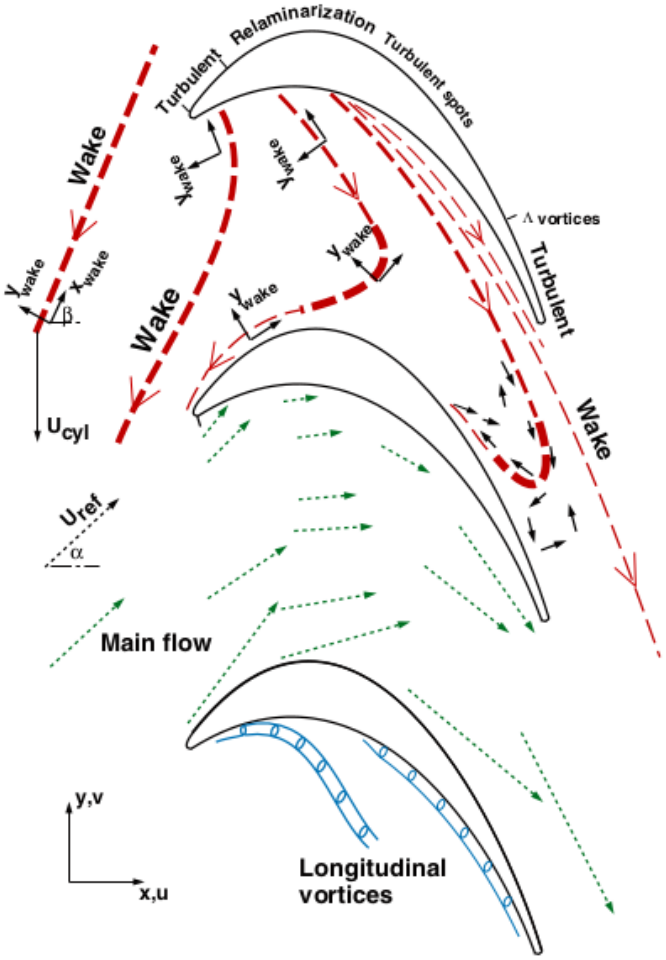

Figure 2.4: Schematic of the flow inside a low preesure turbine passage, from Durbin [27].

cases: separating flow over a flat plate with a variety of inlet conditions, T106 turbine cascade with periodic wakes and the MTU cascade with periodic wakes and freestream turbulence. Their results for the first two cases were in line with previous studies on LPT transition mechanisms. For the third case (MTU cascade) the authors found that wake-induced bypass transition process played an important role for the state of suction side boundary layer. They also found that periodic wakes had profound effect on heat transfer, rising it significantly near the trailing edge of the suction side and on the pressure side. Durbin (2007) [27] offered a composite picture summarizing low-pressure turbine physics based on those early studies shown in Figure 2.4.

Nagabhushana Rao et al. (2013) [72] considered a concerted effect of periodic wakes with elevated freestream turbulence levels on flat plate with pressure contouring representative of suction side for two different high-lift designs. They confirmed that streaky structures originate at the leading edge and showed that streaky structures generated by the wakes were stronger than those generated by the freestream fluctuations. Nonetheless, both freestream turbulence and wakes contributed towards suppression of the separation bubble and were important for accurate loss prediction. They also showed that for both pressure profiles freestream turbulence and wakes reduced separation bubble, but the reduction was more pronounced for the higher lift design.

Wake structure In previous studies wakes were superimposed on the uniform flow either from the precursor planar wake simulation or the simulation of wake behind the cylinder bar. Such wakes differ considerably from the wake left behind by a turbine blade. Wissink, Rodi and Hodson (2006) [117] investigated the impact of wake structure on T106 turbine cascade at similar conditions as previously considered by Wissink [115]. They achieved it by filtering out small-scale fluctuations carried by the wakes and found that small-scale fluctuations play an important role in destabilizing Kelvin-Helmhotlz roll-ups as well as contribute to turbulence production at the apex of the deformed wake. The mechanism of turbulence production within the deformed wake was later explained by Stieger and Hodson (2005) [97] and examined in more detail by Michelassi and Wissink (2015) [67]. Both studies showed that the TKE production is driven by the relative orientation of the stress-strain tensors highlighting the key role of turbulent shear stress in this process.
Sarkar (2009) [89] performed a similar study to the one of Wissink, Rodi and Hodson, but used 2D and 3D precursor simulations of a cylinder bar to generate wakes with different structure (instead of filtering). Much of his findings matched those of Wissink, Rodi and Hodson confirming that suction side behavior depends on the intensity and the length scale of turbulence carried by the passing wakes. He also showed that pressure oscillations along the rear of the suction side depend on the velocity deficit of the migrating wake and are independent of small scale fluctuations.

The effect of wake structure was further investigated by Hammer et al. (2018) [40] who generated different wake profiles by spinning the cylinder bars upstream. This was done for the purpose of generating asymmetrical wake profiles with lower

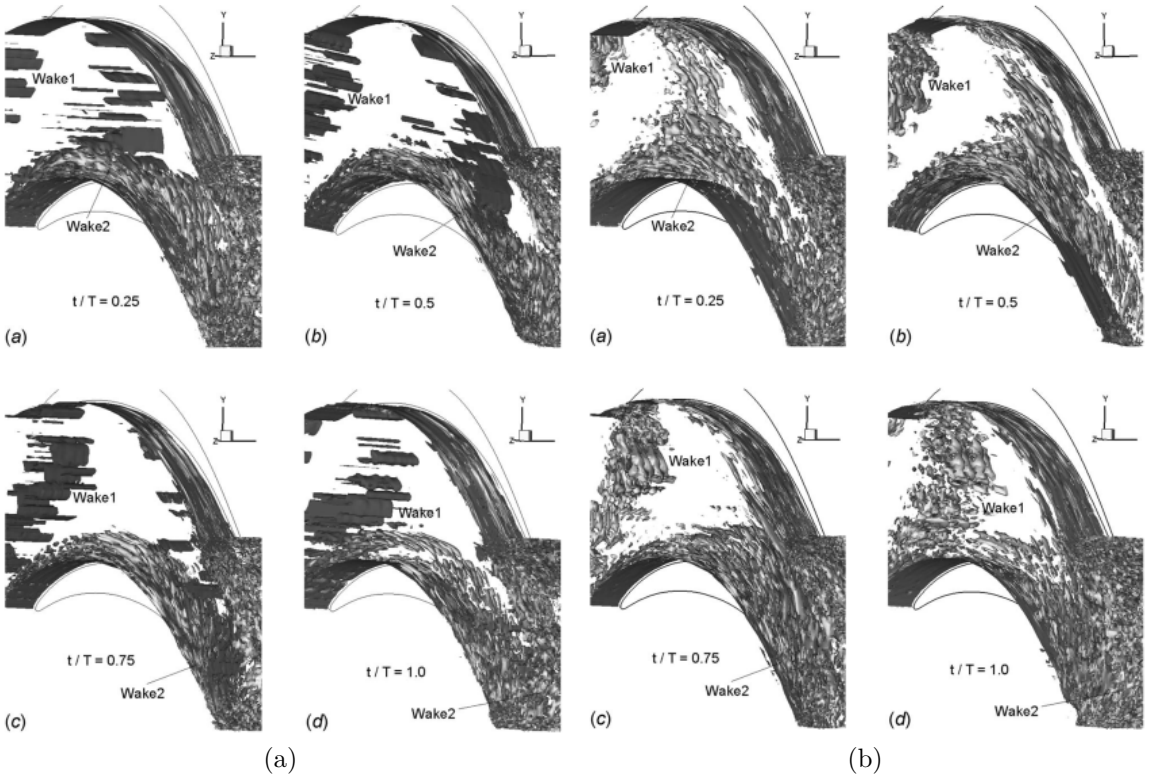

Figure 2.5: Instantaneous isosurface of vorticity at four wake locations for inflow wakes from (a) 2D precursor cylinder bar simulation and (b) 3D precursor cylinder bar simulation, from Sarkar [89].

turbulent kinetic energy levels which are more akin to wakes behind turbine blades. The authors found that counter-clockwise rotating cylinder bar generated wake profiles most similar to those of low-pressure turbine blades. They also demonstrated how this setup led to larger separation bubble than that found for the non-rotating or clockwise rotating bars and how it affected the amount of loss generated by the blade.

Frestream turbulence induced transition Moving away from the wake-induced transition Ravedy et al. (2003) [85] investigated T106 turbine cascade under the influence of freestream turbulence alone at subsonic conditions ($Ma = 0.1$). They observed that the transition process on suction side followed a similar path as one observed earlier by Alam and Sandham (2000) [2] on a separating flat plate, i.e. laminar bubble followed by Kelvin-Helmholtz instability and turbulent reattachment.
Matsuura and Kato (2006) also focused on the effect of freestream turbulence on T106 turbine cascade, but at a higher Mach number of 0.59 to investigate the behavior of

pressure waves that originated near the trailing edge. They found that at high levels of freestream turbulence the separation bubble was highly unsteady, but the effect of unsteady pressure fluctuations was negligible and that transition was mostly driven by the freestream fluctuations.
Recently, Hosseini et al. (2015), [45] revisited LPT transition mechanisms to better understand the evolution and decay of streaky streaky structures under low and high freestream turbulence levels, while Zhang et al. (2015) [129] demonstrated that even high levels of freestream turbulence cannot fully suppress separation bubble for high-lift LP turbine blades operating at low Reynolds numbers ($Re \approx 60k$).

Roughness induced transition Similar to freestream turbulence, roughness also injects inabilities into the boundary layer. Nagabhushana Rao et al. (2014) [71] considered the individual and coupled effects of incoming freestream turbulence and surface roughness on contoured separating flat plate. They used roughness representative of surface damaged by spallation of the thermal barrier coating and showed that roughness promotes near-wall mixing. This mixing was thanks to roughness generated streaky structures that further aided early transition and reduced the size of the separation bubble.

Endwalls Around $30-40\%$ of losses in the low pressure turbines are generated by the interaction of the blade profile with the end-wall boundary layer [81]. Such flows are difficult to understand due to their inherent three-dimensionality. Scale-resolving methods are well positioned to help understand them as they offer insight into full 3D flowfield, consequently, endwall flows received considerable attention. Koschichow et al. (2014) [50] used LES simulation to study the impact of periodic wakes on low pressure turbine endwall flowfield. The authors reported a substantially different vortex system compared to one at mid-span resulting in the reduction of secondary flows and the absence of the horseshoe vortex.
Cui et al. (2017) [20], [19] also investigated endwall flows in low pressure turbines. They considered a blade with an aspect ratio of 2.2 and performed a series of LES simulations to study the impact of purge flows, incoming secondary flows and periodic wakes as well as their interaction with endwall boundary layer on loss generation. They showed that the introduction of purge flow (of 1% leakage rate) increased loss generation by 10% for the considered case. Further still, they reported that the wakes

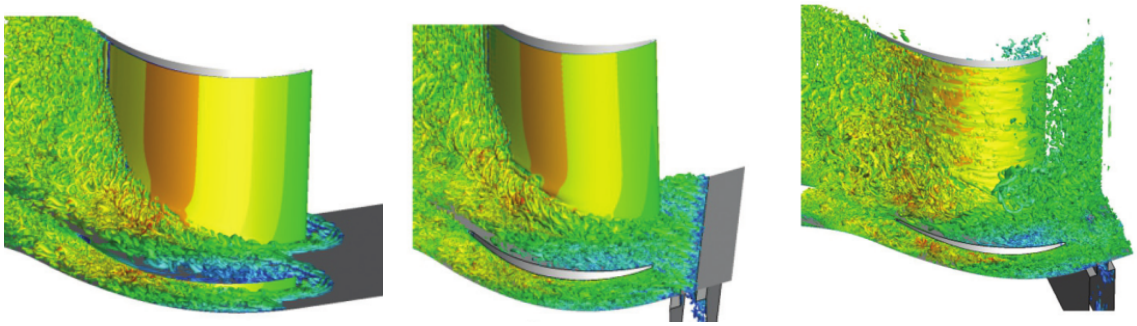

(a) (b) (c)

Figure 2.6: Instantaneous flowfields for (a) clean inflow case, (b) clean inflow with purge flow, (c) inflow with periodic wakes and purge flow, from Cui and Tucker [20].

and secondary flows contributed to a further increase of loss by 20% highlighting the importance of inflow conditions for accurate loss predictions.

Pichler et al. (2018) [81] also addressed LPT endwall flows using LES. They studied LPT blade passage under freestream turbulence conditions with two inlet boundary layer profiles. Their results showed how endwall boundary layer affected the development of vortex system and thus secondary flows. Specifically, they found that higher momentum thickness endwall boundary layer at the inlet was able to push vortex system associated with secondary flows away from the endwall. This proved to have a large effect on generated loss.

(U)RANS comparisons

Given the prominent role of (U)RANS methods in design of turbomachinery components and large uncertainties with regards to the state of the boundary layer, scale resolving simulation results were used to validate and benchmark (U)RANS performance. Wu and Durbin (2000) [118] used their results of wake-induced boundary layer transition on flat plate from the previously described study [120] to benchmark several turbulence models. They reported that certain turbulence models ($\nu^2 - f$) were relatively successful at capturing gross features of wake induced transitional flow.
Michelassi et al. (2003) [66] performed a similar comparison, but of a turbine cascade under periodic wake flow and showed that URANS performs mostly well when compared to LES and DNS solutions. However, they pointed out that URANS struggled with capturing some of the wake dynamics near the suctions side of the turbine blade

especially with regards to spanwise flow gradients.
Durbin and Wu (2007) [27] summarized the early efforts toward simulating and predicting transition and noted that lower fidelity methods like RANS are generally not well suited to correctly predict transition unless coupled with a separate transition model, e.g. based on intermittency transport equation or empirical correlation.
Many other similar studies that used high-fidelity data as reference for RANS benchmarking followed. A markedly different approach was offered by Michelassi et al. (2015) [63] who, instead of comparing first order statistics, examined the validity of Boussinesq eddy viscosity assumption within LP turbine passage with periodic wakes using DNS. To better understand the limitations of Boussinesq approximation they used optimum eddy viscosity formulation as computed from DNS data and demonstrated areas of the flow in which linear stress-strain coupling was violated. They found that this assumption produced significant errors in large portion of the flow, especially in regions with large anisotriopic stress contributions such as around the leading and trailing edge and within boundary layers.
Interestingly, despite above mentioned limitations, Pichler et al. and Marconcini et al. (2018) [81, 56] in their two-part paper reported surprisingly good agreement between LES and RANS simulations of LPT cascade with endwalls under freestream turbulence conditions. Having used best RANS practices, they were able to obtain satisfactory agreement with regards to flow structure, extent of secondary flows, loss distribution and several turbulent quantities. One area for which RANS was not able to reproduce LES statistics was wake development. RANS under-predicted the amount of wake mixing and thus resulted in slower wake decay. Their results suggest that RANS methodology may be currently sufficient for single blade-row analyses, but is inappropriate for multi-blade-row simulations in which wake mixing errors compound and lead to incorrect flowfield evolution downstream and thus loss generation.

LES as design tool

Considering high computational cost of fully resolved DNS, research focus was shifted to under-resolved DNS solutions such as explicitly and implicitly filtered LES and their ability to reproduce DNS solution at a fraction of a cost. Michelassi et al. (2003) [66] and (2003) [65] provided early comparisons between DNS and LES solutions of T106 turbine cascade under periodic wake flow at two different Reynolds numbers ($Re \approx 50k \,\&\, Re \approx 150k$). The authors showed that LES solution was close to DNS at less than 1/5 of the mesh size with minor differences present on the suction side leading

to a delayed transition location by approximately $10\%C_{ax}$. However, they concluded that the outlook for LES use for industrial applications is positive.
Several subsequent studies performed one-off LES simulations asserting its appropriateness for industrial use, but the simulation cost was still prohibitively high for its use as a design tool until recently. One of the first works demonstrating LES use for design was possible was a study by Medic and Sharma (2012) [61] who performed a sweep of high-fidelity simulations to investigate the performance of low-pressure turbine aerofoils at a range of Reynolds numbers and inflow conditions. Further still, Chen et al. (2013), [14] used scale resolving simulation to characterize LP turbine blade performance in terms of loss generation with respect to a combined effect of periodic wakes (with varying frequency) with inflow turbulence. The focus on loss generation was continued in a paper by Sandberg et al. (2015), [88] who looked at the kinetic loss profile downstream of turbine cascade. Additionally, they characterized mixed-out losses and identified dominant loss mechanisms for separated and attached cases.
Building upon the work of Chen et al. and Sandberg et al., Michelassi et al. (2016) [64] performed a sweep of high-fidelity simulations over a range of flow coefficients and reduced frequencies to understand their impact on loss generation in low-pressure turbines, Figure 2.7. They performed detailed loss-breakdown analysis to differentiate between boundary layer and wake distortion losses. They concluded that optimum blade profile design needs to take into account a concerted effect of both flow coefficient and reduced frequency to minimize overall losses.

Another difficult design aspect to study that high-fidelity simulations are well-positioned to address is the effect or stator-rotor gap. Pichler et al. (2018) [79] simulated a turbine stage at two different axial gaps to understand how potential effects and wake-profile evolution impacts loss generation. They found that potential effects had little effect on vane kinetic losses for the considered configuration. On the other hand, the gap had a substantial effect on stator wake mixing and, consequently, on the amount of turbulent kinetic energy entering the rotor passage. Smaller gap led to a higher content of TKE carried by the wake which, in turn, led to an increase of TKE production in a rotor passage as it was subjected to distortion and dilation. The authors reported that the increase in TKE loss outweighed the benefit of more attached suction side boundary layer due to stronger wakes.

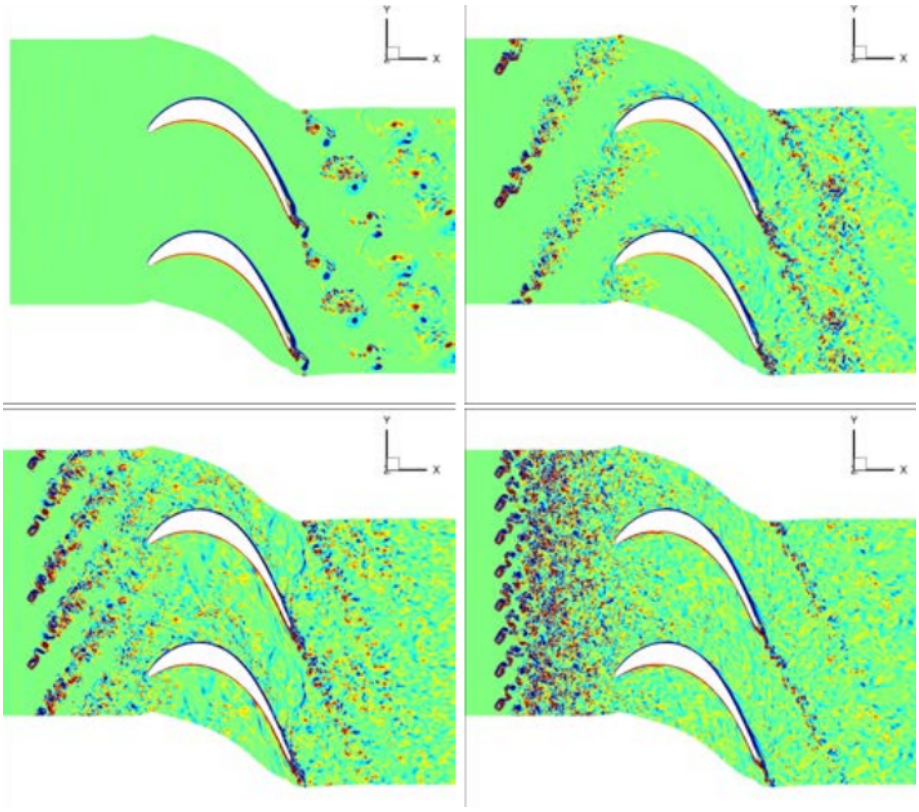

Figure 2.7: Instantaneous z-vorticity contours in the mid-span for a range of reduced frequencies: 0, 0.31, 0.61 and 1.22, from Michelassi et al. [63].

2.2.2 High Pressure Turbine studies

High-pressure turbines operate at much higher Reynolds and Mach number regime. In addition, they are subjected to a turbulent combustor flow characterized by very high freestream turbulence intensity levels and large turbulent length-scales. As a consequence, the flow in HPT does not suffer from suction side separation (as in the LPT case), but transitions via bypass transition process, which has been shown to be very sensitive to freestream turbulence conditions in HP turbines, [4]. Given the constant drive towards higher turbine inlet temperatures, accurate prediction of flows physics and heat transfer is of vital importance to ensure efficiency and reliability of gas turbine engines.

High Reynolds numbers of an order of $Re = 1,000,000$ translate to extremely high costs of scale-resolving simulations. Consequently, studies utilizing scale-resolving simulations are considerably less common for high-pressure turbine flows. Almost the entirety of those studies were also done for the purpose of better physics discovery. Fundamental to these studies was a database developed at the von Karman

Institute by Arts et al. (1992) [4] who performed experimental measurements on high-pressure uncooled inlet guide vanes under various running and inlet conditions ($Re_{ex} = 500k - 2M, Ma_{ex} = 0.9 - 1.1, Tu = 1 - 6\%$). This database has been used extensively to validate and benchmark numerical studies of HPT flows investigated thus far [6, 31, 37, 17, 75, 110, 46, 77, 93, 33].

Flow physics

Frestream turbulence induced transition The study of Bhaskaran and Lele (2010) [6] was the first successful demonstration of an application of high-fidelity simulation to one of the cases from Arts. et al. The authors show an excellent agreement with the experimental data and explored the role of freestream turbulence in triggering transition. They observed, previously reported in low-pressure turbines, streaky structures on both pressure and suction sides. These led to bypass transition on suction side and resulted in augmented heat transfer on both surfaces. They also traced their origins to vortices stretching around the leading edge which then get injected into the boundary layer.
Wheeler et al. (2016), [110] performed the first DNS simulation of HPT inlet guide vanes from Arts et al. for the case with $Re = 570,00$ and $M = 0.9$. They found that for the considered case the breakdown to turbulence on suction surface was achieved via the growth of 2D Kelvin-Helmholtz roll-ups and their development into Λ-vortices, while pressure surface behavior was governed by the presence of longitudinal streaks that extended from the leading edge to the trailing edge, Figure 2.8. Wheeler et al. also performed loss analysis and found that contributions from time-mean strain field, TKE dissipation and heat fluxes accounted for around 40%, 20% and 40% of the total irreversible entropy generation rate, respectively, with a majority of it localized around the trailing edge region.

Pichler et al. (2016, 2017), [78, 77] also carried out a study of the same case showing that their LES setup showed no differences to the DNS by Wheeler et al. [110]. In addition, the authors extended the study to conditions beyond those presented in Arts et al. by considering larger and more representative of flow behind the combustor turbulence intensities (up to 20%) and lengthscales (up to 20%). They found large differences in suction side transition location and length depending on inlet conditions. In addition, they reported that suction side transition process was highly intermittent and local with parts of the flow across the span remaining laminar even close to the

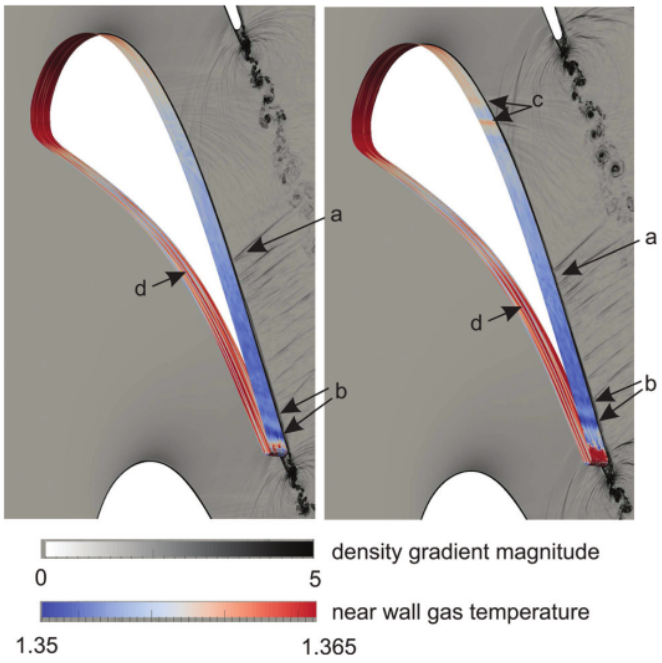

Figure 2.8: Instantaneous snapshots of HPT flow showing presence of (a) upstream moving pressure waves, (b) development of 2d spanwise instabilities over the aft suction surface, (c) fluctuations in surface heat flux due to pressure wave reflections, and (d) near-wall streaks, from Wheeler et al. [110].

trailing edge.

Zhao and Sandberg (2020) [130] continued with the same case at elevated freestream turbulence levels and characterized bypass transition mechanisms and their dependence on inlet conditions in detail. At lower freestream turbulence levels (6.5%) they reported suctions side transition via streak instability. This instability was found to be absent at higher freestream turbulence levels (20%) for which transition happened earlier through the interactions between vortical structures that triggered local turbulent spots, Figure 2.9.

Tip gap Separate to those studies was an investigation by Wheeler and Sandberg (2016) [109] who performed a DNS of an idealized turbine blade tip, Figure 2.10. Their findings pointed to the great complexity of the endwall and tip flows which are generally ignored in high-fidelity studies. They showed that the flow within the gap is highly intermittent in nature and can change dramatically in the presence of cross-flows. They also reported high heat transfers even in the regions of low skin friction, thus

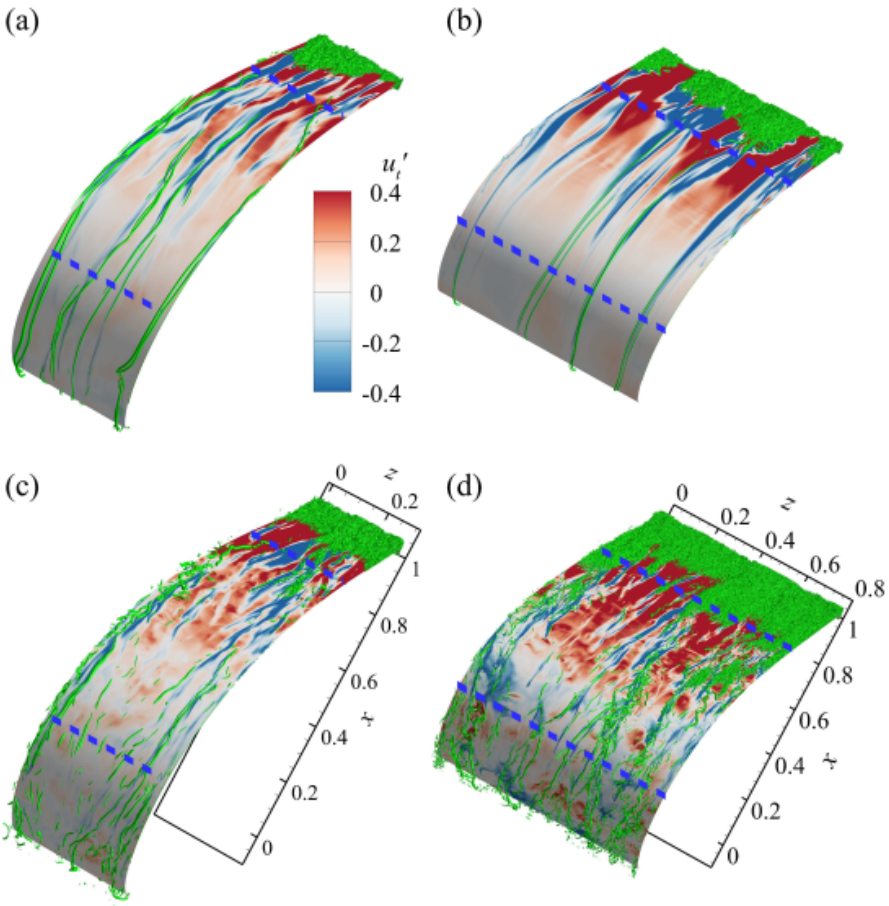

Figure 2.9: Instantaneous snapshots showing vortical structures on suction side for various freestream turbulence levels and turbulence lengthscales, (a) $Tu = 6.5\%, Ls = 5\%$, (b) $Tu = 6.5\%, Ls = 20\%$, (c) $Tu = 20\%, Ls = 5\%$, (d) $Tu = 20\%, Ls = 20\%$, from Zhao and Sandberg [130].

invalidating often used Reynolds analogy.

(U)RANS comparisons

Because of the complex process of bypass transition, RANS simulations were found to be unfit to capture the HPT flowfield and heat transfer. Fransen et al. (2011) [31] carried out an LES vs RANS comparison for two cases: inlet guide vane flow from Arts et al. and internal cooling channel. For both cases RANS failed to correctly reproduce the flowfield and accurately predict the heat transfer. For the inlet guide vane case RANS shortcomings were pinpointed to its inaccurate prediction of transition location and length, especially with regards to the suction side boundary layer. Similar findings

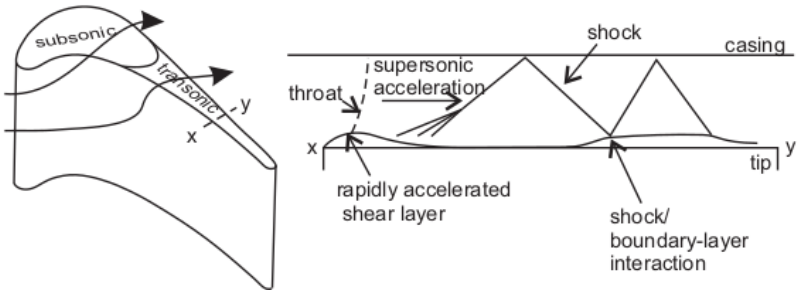

Figure 2.10: Schematic of a transonic tip flow, from Wheeler and Sandberg [109].

were echoed by Gourdain et al. (2012) [37] who noted that RANS was able to predict wall heat transfer when boundary layers were either fully laminar or turbulent, but not when the boundary layer was transitioning or its behavior was intermittent. Garai et al. (2018) [33] also attempted a similar comparison and as in the study of Fransen et al. [31] found that RANS was unable to reproduce experimental data on suction side and predicted earlier and shorter transition and consequently a thicker boundary layer.

LES as design tool

Currently both DNS and LES simulations are prohibitively expensive for the use in HPT design process. However, hybrid approaches are being evaluated such as wall-modeled LES. One such study was performed by Papadogiannis et al. (2014) [75] who investigated the effects of mesh resolution and sub-grid scale model choice on wall-modeled LES results. The outlook given by the authors, however, suggests that such methods are not yet appropriate for industrial use as results varied wildly with regards to boundary layer state, shock structure and resulting unsteadiness depending on sub-grid scale model choice, especially for coarser meshes.

2.2.3 Compressor studies

Compressor design faces multiple aero and aero-mechanical challenges. Its operation at adverse pressure gradient means the flow is prone to separation and instabilities such as stall and surge which have major impact on compressor efficiency and operability. The potential role of transition in compressor stability, especially at near stall conditions, motivated the early use of scale resolving simulations for compressor flows. This motivation was further strengthened as axial compressor design trends moved towards

increased loadings, higher tip speeds and more three-dimensional blading rendering existing empirical correlations unfit to capture these effects on new design choices [87]. Fundamental to early high-fidelity studies was experimental work of Hilgenfeld and Pfitzner (2004) [42] who performed experiments with grid turbulence and periodic wakes on NACA65 V103 blade profile. This setup was extensively studied using scale-resolving simulations in a series of publications by Zaki et. al [124–127] to describe transition mechanisms in compressors. The details of these studies along with subsequent works on compressor physics using high-fidelity simulations are discussed below.

Flow physics

Frestream turbulence induced transition The effect of freestream turbulence on compressor transition was studied by Zaki et al. (2006, 2010) [124, 125, 127] who used NACA65 cascade at $Re \approx 140k$ at a range of different turbulence intensity levels $(0-10\%)$. They observed a range of transition mechanisms on both pressure and suction side which differed depending on the turbulence level. When inflow conditions were laminar (i.e. not inflow turbulence), the authors found that the flow on both surfaces separated. At moderate freestream inflow turbulence levels of around 3.5%, pressure side boundary layer underwent attached transition which carried signatures of both natural and bypass type. Suction side boundary layer separated similarly as for the laminar inflow case, but the separation was followed by Kelvin-Helmholtz instability and breakdown to turbulence leading to boundary layer reattachment. Despite transition being of separated type, the authors reported a strong presence of streaky structures which modulated the instantaneous flowfield which had an effect on the size of separation bubble. At high inflow turbulence levels of 6.5% and above, boundary layer on both sides was found to shift towards bypass transition scenario. Notably, on suction side, higher freesrteam turbulence level resulted in stronger streaky structures; these structures led turbulent spots which suppressed separation bubble locally. At sufficiently high freestream turbulence level, the frequency of turbulent spots was such that separation was almost entirely suppressed. These works highlighted the rich transition phenomena present in compressors as well as its sensitivity to inflow conditions.

Recently, Wheeler et al. (2018), [113] performed a DNS study of CDA compressor cascade at a range of Reynolds numbers ($Re \approx 100-400k$) and explored the non-equilibrium behavior of boundary layer. Non-equilibrium behavior tends to give rise to a lag between turbulence production and dissipation. The authors demonstrated that this lag affects loss by reducing dissipation coefficient, as compared to an equilibrium

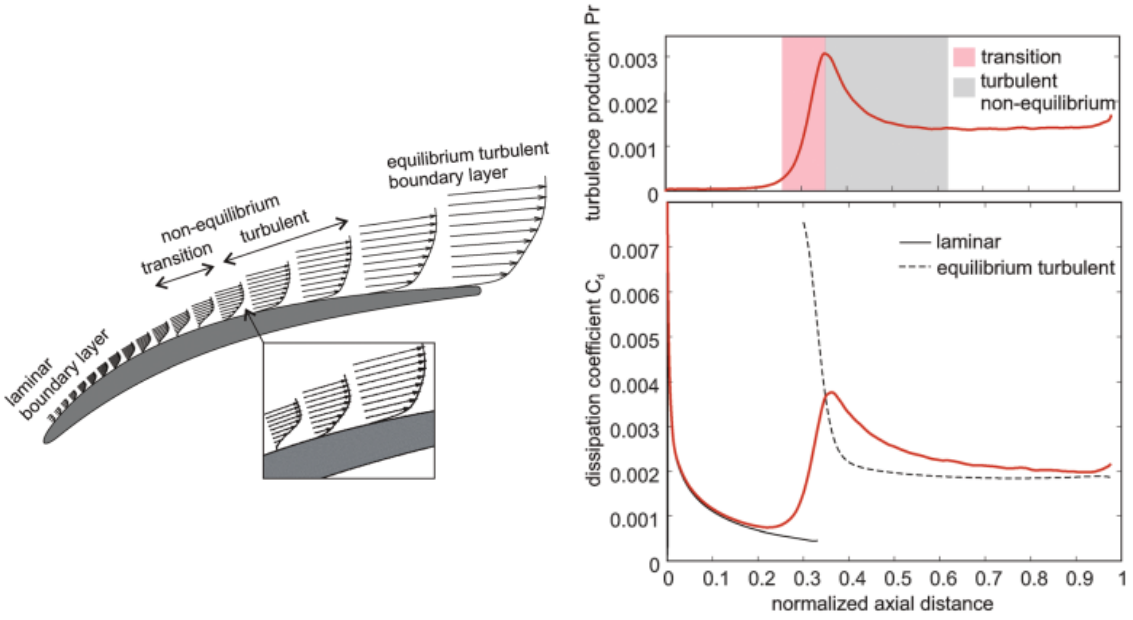

(a) (b)

Figure 2.11: Schematic of boundary layer states on a compressor blade suction surface (a) and plots of turbulence production and dissipation coefficient (b), from Wheeler et al. [113].

boundary layer, but can also increase loss where separation bubbles occur by delaying reattachment. This is important because most turbomachinery turbulence models assume that production and dissipation are largely in balance. Wheeler et al. showed that up to 30% of suction side boundary layer exhibited non-equilibrium behavior, Figure 2.11. This has a potential to significantly alter compressor performance when compared to equilibrium turbulence behavior.

Wake-induced transition The effect of wakes on NACA65 cascade was studied by Zaki et al. (2009) [126] and Wissink et al. (2014) [114], Figure 2.13. These studies concerned the same setup with periodic wakes, but no freestream turbulence ($Re \approx 140k, F_{red} = 1.4, \phi = 2.48$) and featured wakes of different strength and turbulence intensity. For both cases wakes were obtained from a precursor simulation of a cylinder bar flow, but in the case of Zaki et al. [126], the wakes were rescaled to decrease the mean wake velocity deficit (from 16 to 14% of inlet velocity and decrease the maximum turbulence intensity within the wake (from 6 to 3.6%). As a consequence, the authors of both studies were able to differentiate between the effect of weak and strong wakes

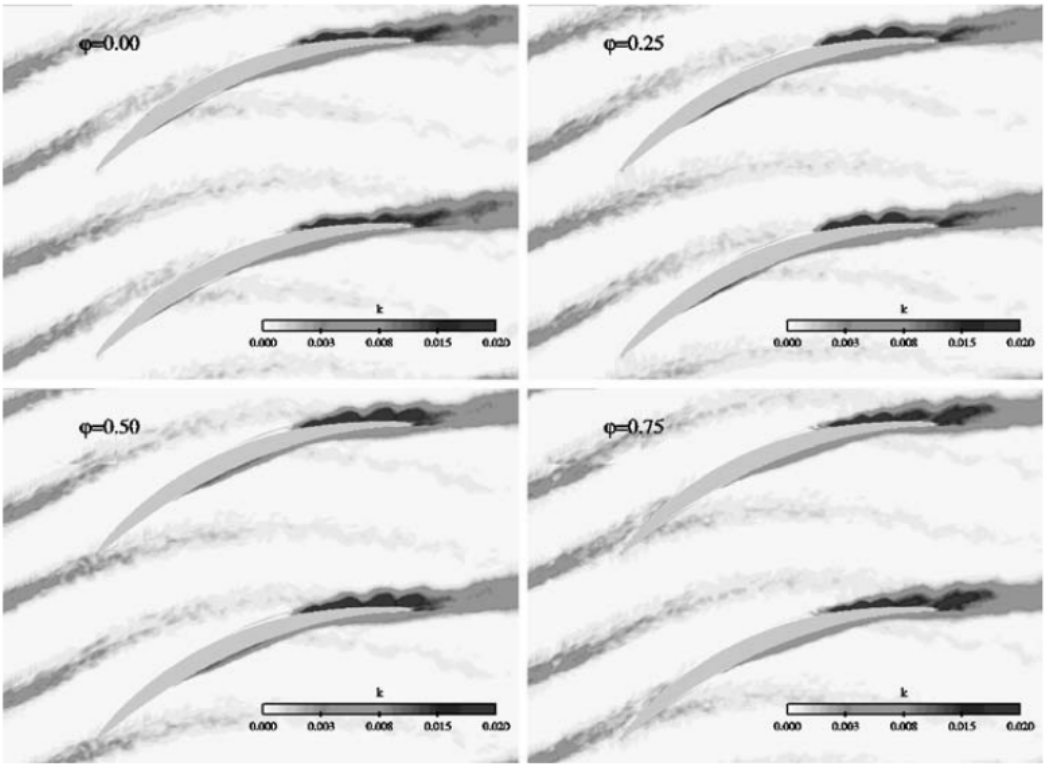

Figure 2.12: Contours of phase averaged kinetic energy at four wake phases, from Zaki et al. [126].

on compressor transition mechanisms.

Both weak and strong wake cases were able to trigger bypass transition on the pressure side close to the leading edge. This poses a modelling challenge as the results suggest that correlation between instantaneous freestream turbulence and transition location is not appropriate in the presence of passing wakes. Suction side was found to separate for both cases, however, strong wakes, were able to suppress the separation bubble due to local forcing. In addition, transition was intermittently triggered in between wake periods through streak instability. These streaks were found to originate from the disturbances introduced inside the boundary layer by the passing wakes and led to turbulent spots. As a consequence of the interaction between turbulent spot and separated shear layer, the flow underneath the turbulent spot locally reattached and shortened the separation bubble.
However, relevance of these studies to turbomachinery applications is limited due to the unusual choice of nondimensional parameters. In particular, the value of flow coefficient used for the simulation, $\phi = 2.48$, far exceeds the range of values typically

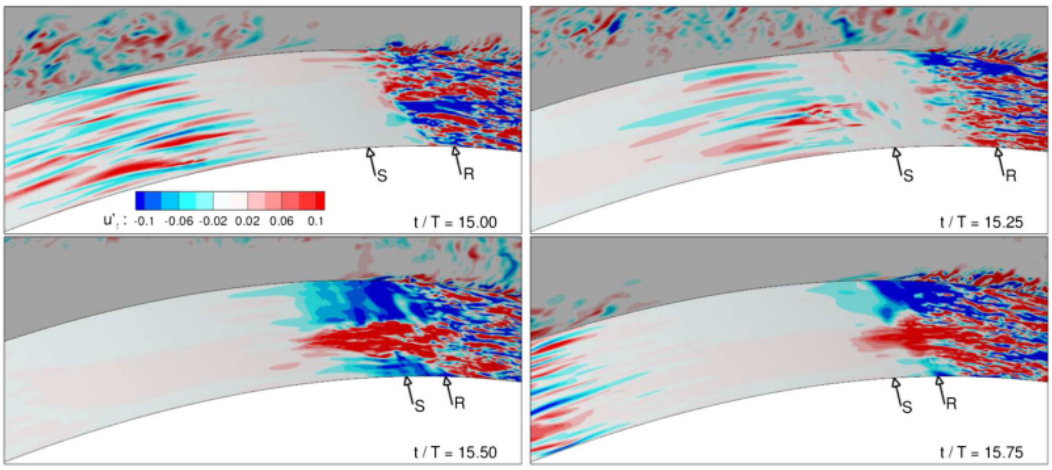

Figure 2.13: Instantaneous tangential velocity fluctuations inside the suction side boundary layer at four wake locations for the case with strong wakes with arrows identify the locations of boundary layer separation (S) and reattachment (R), from Wissink et al. [114].

found in axial compressors of $\phi = 0.4 - 1.0$. As a result of such combination of the flow coefficient and reduced frequency, the upstream wake orientation is drastically different from the one with more conventional choice of these non-dimensionals, e.g. such as in the simulation of Legget et al. [54], Figure 2.18 (c). Consequently, the impact of the wake on the boundary layers and wake-induced transition mechanisms presented in these studies may be unrepresentative of the engine conditions.

Wake-induced transition on compressor blades was further considered in works by Legget et al. (2018) [54] and Scillitoe et al. (2019) [91]. Unlike previous studies, these authors used inflow conditions featuring both: periodic wakes and accompanying freestream turbulence. Both simulations were also more representative of conditions found in aero-engines.
Legget et al. embedded a series of cylinders in their domain to represent the upstream wakes and considered NACA65 cascade at engine representative conditions ($Re \approx 300k, F_{red} = 1.9, \phi = 0.89$). Their analysis, however, was limited only to reporting phase-locked Mach number and skin friction distributions. Scillitoe et al. used rescaled wakes following methodology of Zaki et al. [126] and considered CDA cascade at comparable flow conditions ($Re \approx 230k, F_{red} = 1.2, \phi = 0.9$). They also reported phase averaged skin friction, but, in addition, commented on the important role of streaky structures in between wake periods. They found these structures convected at around 70% of freestream velocity and triggered turbulent spots which were responsible for

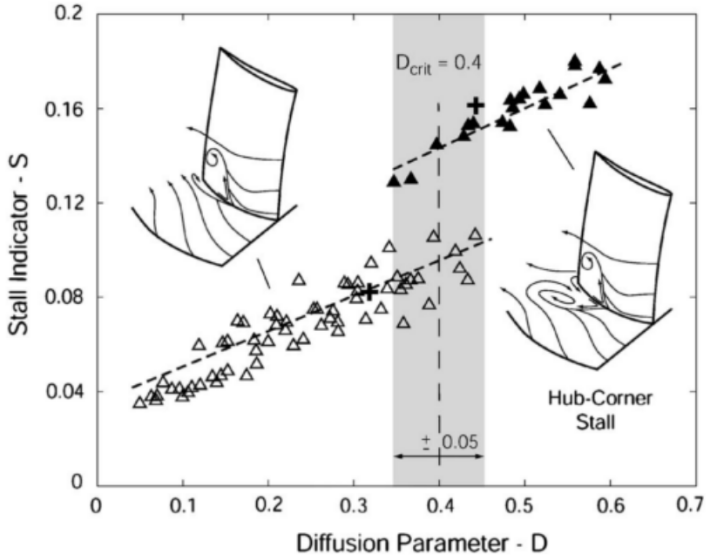

Figure 2.14: Stall indicator vs diffusion parameter map, from Lei et al. [55].

periodically shortening the suction side separation bubble.

Endwalls Endwalls are notoriously difficult to accurately predict in compressors. Compared to turbines compressors feature thicker endwall boundary layers and are more prone to separation due to the adverse pressure gradients they operate in. When endwall flow separates, it merges with suction side separation and is usually of complex three dimensional nature. As explained by Lei et al. [55], this corner separation may take on one of two states and be of closed and open separation topology. Interestingly, Gao et al. (2015) [32] used LES of NACA65 cascade at $Re \approx= 400k$ to demonstrate that corner separation can switch between these two modes in an intermittent and a-periodic fashion.

Scillitoe et al. (2017) [92] also examined compressor corner separation, but focused on its dependence on freestream turbulence levels and endwall boundary layer state by considering NACA65 and CDA linear cascades, e.g. Figure 2.15. The authors found only limited sensitivity of corner separation to freestream turbulence, but reported on a critical role of endwall boundary layer state. They showed that a laminar endwall boundary layer separates earlier that turbulent, thus leading to a larger passage vortex and increased loss. Their analysis also revealed a critical role LES subgrid scale model can play in accurate flow prediction, especially for relatively coarse grid resolutions.

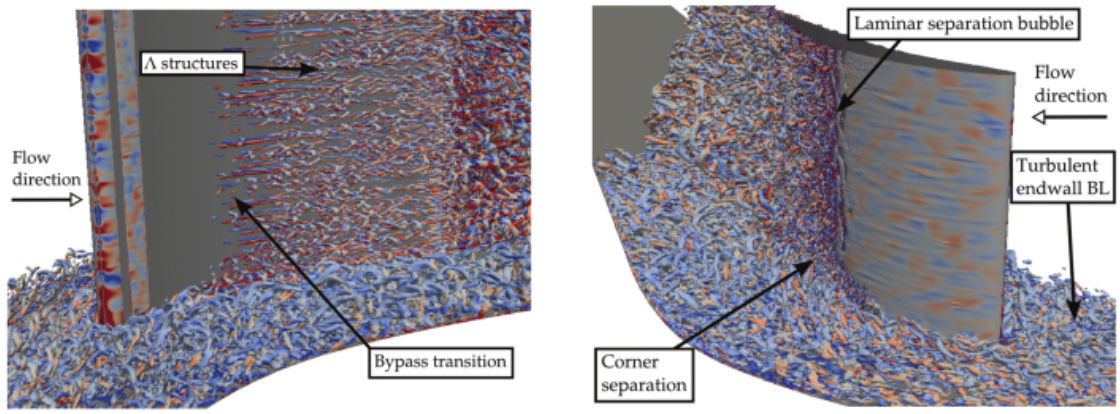

(a) (b)

Figure 2.15: Instantaneous snapshots showing vortical structures on: (a) suction surface and (b) pressure surface, from Scillitoe et al. [92].

Tip gap The subject of rotor tip gap and loss mechanisms associated with it was addressed by You et al. (2006, 2007) [121, 122]. Their setup consisted of a linear cascade at $Re \approx 400k$ with tip clearance and a moving endwall with turbulent boundary layer at the inflow. The authors identified vortex system associated with tip clearance flow and identified tip-leakage vortex and tip-leakage jet as major sources of viscous losses, Figure 2.16. These flow features were driven by the pressure difference between suction and pressure side and resulted in significant mean strain field, especially in spanwise direction. The strains gave rise to enhanced production of vorticity and turbulent kinetic energy which then dissipated downstream resulting in large viscous losses. The tip-leakage vortex and tip-leakage jet were, in fact, found to produce majority of Reynolds stresses and TKE. Interestingly, the authors reported that tip-gap size did not significantly affect the mechanisms outlined above, only noting that smaller tip-gaps led to reduced magnitudes of vorticity and TKE within tip-leakage vortex and jet.

(U)RANS comparisons

As the costs of sufficiently resolved high-fidelity simulations for compressors are still too high for the wide-spread adoption of them within the industry, many authors wondered whether idealized case studies or under-resolved LES simulations may offer advantages over currently used URANS methods for design purposes. These questions were addressed by Gourdain et al. (2014) [38] who highlighted the high sensitivity of

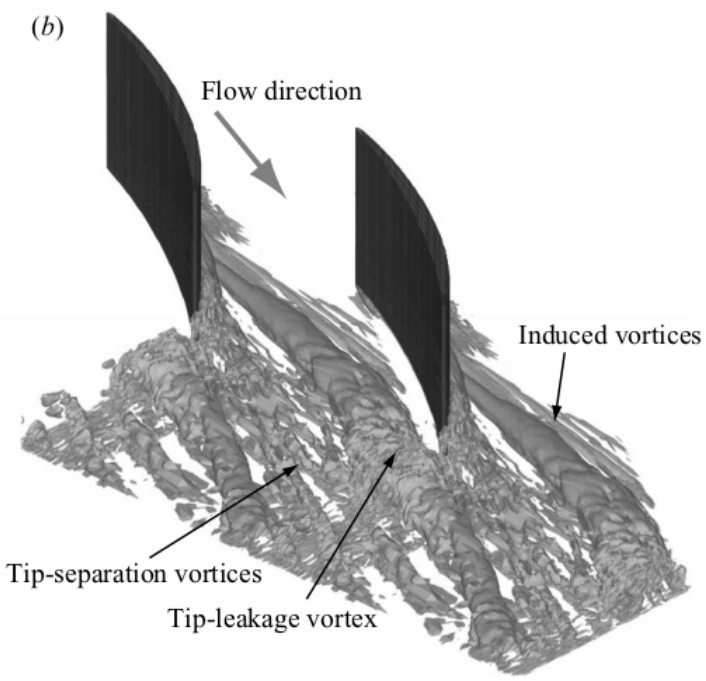

Figure 2.16: Vortical structures obtained from time-averaged flow field, from You et al. [122].

LES simulations to grid resolution, but noted that its attractiveness lies in its ability to help better understand compressor flow physics.
The differences between URANS and LES were further explored by Gourdain (2015) [35, 36] who performed one of the largest compressor LES studies to date by simulating a full compressor stage at $Re \approx 700k$ using almost 860M cells, Figure 2.17. Nonetheless, the final grid was still fairly coarse for high-fidelity study standards and the comparison with experimental measurements showed only limited improvement for LES over URANS in terms of overall pressure ratio and efficiency. However, LES advantages lied in its improved prediction of wake evolution and boundary layer behavior. In addition, LES revealed presence of a frequency peak in tip-leakage flow spectrum at frequency different than blade passing frequency (or its harmonics) which was missing from URANS analysis. This highlights URANS inherent inability to capture complex behavior that result from the interaction between deterministic and stochastic unsteadiness as mentioned before. Gourdain also notes that his results indicated an important role of transition in determining compressor performance accounting for over 2% of efficiency when compared to URANS results that assumed fully turbulent boundary layers.

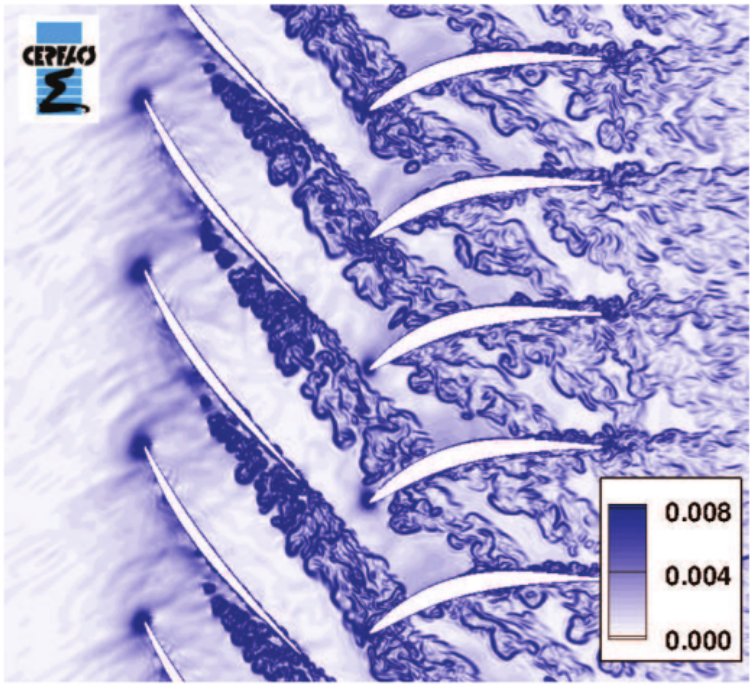

Figure 2.17: Instantaneous flow field close to the casing shaded with density gradient, from Gourdain [35].

Leggett et al. (2018) [54] carried out a comparison between LES and RANS for a range of incidences for NACA65 cascade at $Re \approx 300k$ and showed that by following RANS best practices, they were able to match the overall loss and pressure distribution results for both methods. A more detailed analysis revealed that while overall performance was well predicted by RANS, the split between pressure and suction side loss was considerably different from the one predicted by LES. RANS was also unable to accurately predict wake shape and its evolution which is of great importance when considering multi-stage environments.

LES as design tool

Early studies in this area focused on LES ability to reproduce complex physics of boundary layer transition compared to more expensive DNS studies. Lardeau et al. (2012) [52] carried out such comparison, notably, using the case of Zaki et al. [127]. He showed that LES can offer accurate representation of the flowfield at 10% of the equivalent DNS resolution given appropriate subgrid modelling. However, the authors only compared NACA65 cascade at two lowest freestream turbulence levels of 0 and

3.25% that were easier to match for LES and featured separated flow transition on suction side. A comparison featuring higher freestream turbulence level was included in the study by Scillitoe et al. (2019) [91] who was also able to obtain a close agreement with DNS by Zaki et al. at a fraction of a cost using a grid $10x$ smaller. In their case, most of the grid reduction stemmed from a relatively coarse mesh in wall normal direction but wall units were representative of wall resolved LES simulations (50/1/15 maximum wall units in streamwise, normal and spanwise directions).
Another aspect of LES use for industrial applications that was inspected by various authors was its reliability in predicting cascade's loss bucket, i.e. cascade performance against the incidence which is crucial for understanding compressor's off-design performance. McMullan and Page (2011) [60] did such analysis for CDA cascade at $Re \approx 700k$ and reported good agreement near the design angle, but growing discrepancies at both high positive and negative incidences owing to a coarse grid used in the study. Leggett et al. (2018) also performed a similar analysis and generally considered how LES can aid understanding of loss generation in compressors at off-design conditions by considering a NACA65 cascade at $Re \approx 300k$ under various incidences and with periodic wakes, Figure 2.18.
A comprehensive overview of LES studies used in industrial practice is offered by Gourdain [38] and further extended by considering more recent works by Scillitoe (2017) [90]. Gourdain summarizes the state of the LES for compressor industrial studies as split between idealized highly resolved academic studies and under-resolved studies of complex geometries carried out by the industry practitioners. He suggests that combining experiences from both ends may result in major progress towards the use of high-fidelity simulation in compressor design.

2.3 Resolution considerations for scale-resolving simulations

Despite the success of high-fidelity methods for some applications these methods suffer from the lack of resolution guidelines. To reach their full potential as virtual experiments the accuracy has to be ensured. To directly solve Navier-Stokes equations DNS resolution must be sufficient to resolve all the scales in the flow down to the Kolmogorov length scale ($\eta_{Kol} = (\nu^3/\epsilon)^{1/4}$). The estimate of the number of grid points required to achieve DNS can be obtained by comparing the Kolmogorov length scale to the large eddy characteristic velocity and length scales, Davidson [21]. This leads to a well-known

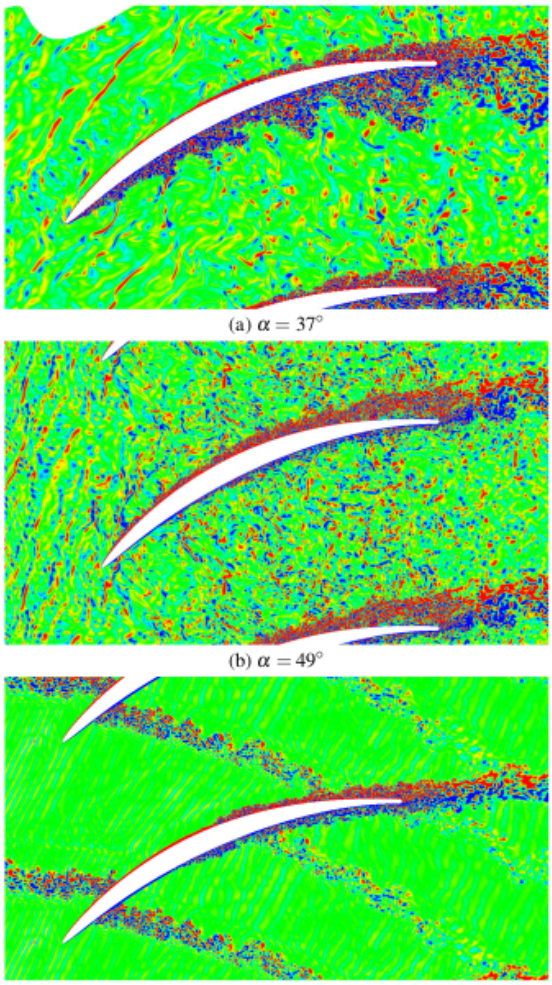

Figure 2.18: Instantaneous z-vorticity contours for (a) negative incidence case, (b) positive incidence case and (c) wake case, from Leggett et al. [54].

scaling of $N \propto Re^{9/4}$ for the number of points needed for a turbulence simulation. This estimate was further revised to $N \propto Re^{37/14}$ by Choi and Moin [15] for the wall bounded flows. Given these estimates it is easy to see why DNS is rarely used for industrial applications. It is therefore of interest to understand whether full resolution is needed for such simulations, what the impact of resolution on scale-resolving simulations is and what resolution guidelines one should follow.

Traditional RANS guidelines are not applicable in this case and there is no consensus on resolution requirements for such simulations. The lack of computational requirements for capturing correct flow physics is leading to inconsistent loss predictions even for scale-resolving simulations depending on the chosen convergence criteria. In the context of turbomachinery setting, as noted by Sandberg and Michelassi [87], this assessment

has been mostly based on first-order statistics, which is much less stringent measure of accuracy than in most of the other canonical studies.

Historically, DNS simulations were performed on idealized cases such as those of incompressible turbulent channels using spectral methods, e.g. Kim, Moin and Moser [48]. The resolution of such cases was assessed using energy spectra that demonstrated no energy accumulation at high wavenumbers and an energy reduction of over three-four orders of magnitude over the resolved scales. However, these criteria are difficult to implement for industrially relevant cases and cannot be extended to studies of transitional flows as noted by Zang et al. [128].

Various authors investigated different aspects of how resolution affects the solution accuracy. Souza et al. [96] studied resolution requirements for correct prediction of natural transition (via Tollmien-Schlichsting waves) in Poiseuille flow using a variety of numerical schemes. Their recommendations were in line with dispersive properties of respective schemes they tested. Geurts and Fröhlich [34] presented a framework for assessing LES accuracy in terms of resolved kinetic energy evolution and viscous dissipation. Celik et al. [13] created an index of resolution quality for LES, while many other authors reported on the complexities of assessing LES accuracy and LES errors, e.g. [39, 49]. More recently Rezaeiravesh and Liefvendahl [86] developed an uncertainty quantification framework and gave resolution recommendations based on viscous wall units that result in acceptably low errors for turbulent channel flows.

Early studies of industrially relevant turbomachinery cases were primarily focused on transition mechanisms and the effect of resolution on accuracy was not reported in them. Wu and Durbin [119] were first to apply DNS type simulation to low pressure turbine (LPT) flow to study laminar-to-turbulent transition on the pressure surface. Their resolution was based on their previous flat plate simulations which were validated using mean pressure distribution experimental data. This study was later followed by Wissink [115] who focused on the behavior of boundary layer separation on suction surface. In this case the study was validated using mean pressure distribution and wake loss experimental data.

In a series of studies Zaki et al. [125–127] performed incompressible simulations of a NACA65 compressor cascade at moderate Reynolds number with varying levels of freestream turbulence. Zaki et al. reported viscous wall units which were in line with DNS standard, but noted that the pressure distribution from the DNS and the experiments were not in quantitative agreement, but key features of the mean flow were consistent between the numerical and physical experiments.

More recently, scale resolving simulations were used to characterize the blade perfor-

mance in terms of loss generation. Chen et al. [14] performed a compressible simulation of LPT flow and characterized blade performance in terms of loss generation with respect to a combined effect of wakes with varying frequency with inflow turbulence. The focus on loss generation was continued by Michelassi et al. [63] who identified dominant loss mechanism for separated and attached flow cases. Loss generation within a high-pressure turbine (HPT) vane was studied by Wheeler et al. [110] who performed an HPT simulation and looked at the integrated entropy generation rate in the passage. All these studies also primarily relied on mean pressure distribution and wake loss measurements, with an exception of Wheeler et al. who also used heat flux at the wall to validate their results.

Notably, Pichler et al. [80] studied resolution requirements in LPT flows. They found that to reach grid convergence for turbulence dissipation is ten times more computationally costly than to reach it for turbulent kinetic energy. They also noted the disparity in convergence criteria for canonical and turbomachinery studies. More generally they report on the lack of formal guidelines of what appropriately resolved/mesh-converged simulation entails.

Given the challenging resolution requirements posed by the scale resolving simulations, another area of research that received considerable attention was the use of high-order methods. Unsteady flow simulations demand long time-integration coupled with the need for minimal dissipation and dispersion errors. This is particularly true in the case of computational aeroacoustics for which standard low-order methods are insufficient to compute and accurately propagate acoustic waves, [99, 7]. High-order schemes have also become a popular choice for scale resolving simulations for their ability to better preserve vortical structures, Ekaterinaris [28]. Such schemes prevent excessive numerical diffusion and allow for more accurate simulation of complex vortical fields. This is crucial when it comes to viscous dissipation computations and loss predictions. High-order schemes can also reduce computational requirements of scale resolving simulations by offering considerably better solution accuracy for the same mesh size, Wang et al. [108].

2.4 Multi-stage environment

Scale-resolving compressor simulations have mostly concerned isolated cascades and their performance under a variety of inflow conditions. These inflow conditions were mostly based on synthetically generated turbulence or precursor simulations of cylinder flows. Given compressor sensitivity to inflow conditions, such studies, while offering

insight into fundamental mechanisms, may not be appropriate for gas turbine designers and practitioners. Modern gas turbines consist of multiple axial compressor stages to achieve high pressure ratios; it is, therefore, likely that inflow conditions and unsteadiness seen by the latter stages of the multi-stage compressor is purely determined by the interactions between upstream blade-rows and dependent on the gaps between these blade-rows. Considering current compressor design trends, understanding the impact of blade-row interactions (including the effects of upstream blade-rows) and quantifying the impact of rotor-stator gap on compressor performance are of critical importance for efficient design of future multi-stage compressors.

The size of the rotor-stator axial gap in a multi-stage compressor is also important in determining the overall size of the machine as well as the aspect ratios of the blading. Nonetheless, the effect of the axial gap on performance is not well understood. In order to reduce weight it may be desirable to minimize axial gaps, however this is likely to lead to strong interactions between rotors and stators, driving high levels of unsteadiness and potentially increasing loss. On the other hand, larger axial gaps may lead to increases in overall machine size and more significant endwall losses.

The size of rotor-stator axial gap is likely to influence several loss mechanisms including wake mixing loss and transition. The effect of axial gap on wake mixing loss has been discussed by several authors. Smith [95] reported measurements on a multi-stage compressor, which indicated a reduction in loss when axial gaps were reduced and suggested this was linked to the kinematic effect of wake stretching. Adamczyk [1] later developed the model confirming that the process is primarily of kinematic nature and related it to the wake vorticity. The effect of axial gap on steady-state performance was further explored numerically by Deregel and Tan [26], while Van Zante et al. [107] showed experimentally that the inviscid wake recovery effects dominate the wake viscous effects in high-speed axial compressors and gave design recommendations based on their findings.

The choice of axial gap will also affect the boundary layer development and transition. Rotor wake interactions are well known to promote transition (see for example Henderson and Walker [41], Wheeler et al. [111, 112], Zaki et al. [126] and Legget et al. [54]). Thus shorter axial gaps will tend to increase the strength of wake interactions and drive earlier transition, leading to increases in turbulent wetted area and loss.

Another aspect which has received little attention in the literature is the effect that rotor-stator axial gap has on the nature of turbulence within a multi-stage machine. Camp and Shin [10] measured turbulence levels in several multi-stage machines and reported turbulence levels in the range of $3.6 - 11\%$ depending on stage loading coeffi-

cient. It is very challenging to test the effect of rotor-stator axial gap in a real machine. High fidelity (scale-resolving) simulations offer a potential solution to capturing the true nature of turbulence within the machine. However DNS and LES are typically performed for single passages or stages (for instance [126, 54, 91]) and multi-stage effects are thus not captured. Furthermore, these high-fidelity simulations have imposed inflow turbulence which required a-priori knowledge of the incoming turbulence intensity and length-scales.

2.5 Concluding remarks

The studies summarized in this chapter focused mostly on building up the understanding of flow physics and their sensitivity to inflow conditions. They showed that scale resolving simulations may bring new quality to design practice, but their potential has thus far remained untapped. One of the main problems with the use of scale-resolving simulations for industrial practice is lack of confidence in the accuracy and quality of the results. Even though, authors of DNS/LES studies successfully explained the mechanisms at work, resolution considerations were rarely addressed. In Chapter 4 and Chapter 5 the requirements for accurate loss predictions are considered. Specifically, the aim of these chapters is to answer questions regarding:

- the effect of resolution (discretization and scheme order) on loss accounting
- the effect of resolution on the physical mechanisms generating loss

It will be demonstrated in these chapters that accurate prediction of entropy generation rate can be achieved without the need for resolving the full dissipation spectrum. In fact, it is shown that the accuracy of a simulation with regards to loss, is to large extent dependent on capturing the correct physical mechanisms driving loss. In the cases discussed here, this depended on capturing the correct mechanisms driving transition, and the subsequent turbulence production.
This chapter also highlighted the relative lack of understanding of compressor multi-stage effects. High-fidelity simulations made inroads in helping to understand multi-stage effects for low-pressure turbines. This has not yet been achieved for compressors. However, the observation of the repeating-stage phenomenon (see Smith [95]) suggests that for a repeating stage, the turbulence is likely to develop an equilibrium state, neither growing in intensity nor decaying through the machine. Chapter 3 makes use of this phenomenon by establishing a repeating-passage simulation in order to study the flow representative of multi-stage environment. The simulation relies on a new wake

recycling method. This method is shown to successfully replicate a repeating-passage flow field, albeit for the mid-span section of a compressor stator. In addition, the method does not rely on a-priori knowledge of the turbulence. This fact is used in Chapters 6 and 7 to study the flow as observed by an embedded blade-row of 50% reaction machine. The results are used to demonstrate and quantify the effect of axial gap on a multi-stage environment and compressor performance. It is further shown that in multi-stage environment rotor-stator gap controls a feedback mechanism that determines the overall flow unsteadiness.

Chapter 3

Computational Methods

An in-house solver 3DNS has been used for the studies discussed in this thesis. The solver has been developed by Dr Wheeler and has been previously employed to investigate non-equilibrium turbulence behaviour in compressor cascades, Wheeler et al. [113]. The code has been implemented with a focus on minimising numerical errors which is of particular importance for time-dependent problems. This chapter discusses the key features of the code and code additions that were implemented to carry out simulations presented here.

3.1 Summary of 3DNS solver

3DNS is a fully-parallel, multi-block, structured body-fitted compressible Navier-Stokes solver implemented in FORTRAN. Simulation domain is made up of multiple blocks and each block is subdivided into smaller domains. Each such subdomain is assigned to a single core. Each core stores only grid and flow information that is related to its subdomain. Parallelisation and communication between these subdomains is managed using MPI libraries.

The equations are discretised and solved for the conserved quantities using finite differences and selective spatial filters. A range of central finite difference schemes were used for this study and are discussed in more detail below. To solve the equations for complex geometries, e.g. compressor airfoils, the grid in each block is transformed from physical to computational space using grid metrics, also explained below. Time stepping is implemented with a 4-stage fractional step Runge-Kutta. To minimise the amount of allocated memory low storage Runge-Kutta scheme is used.

To minimise numerical errors, several considerations were taken into account when developing the code. These considerations are discussed below.

3.1.1 Dissipation considerations

Numerical dissipation often plagues CFD codes. This extra dissipation is added via discretisation errors present in the numerical scheme. It affects the amplitude of the convected waves by smoothing them out and decreasing the gradients within the flow. That smoothing effectively acts as an additional viscosity, thus lowering a local Reynolds number. As Reynolds number is decreased the behaviour of the flow may change by, e.g. excessively dissipating the instabilities, stabilising the flow and delaying transition.

One way to address this problem is to use non-dissipative schemes such as central finite difference schemes. These schemes, however, are unstable and result in spurious grid-to-grid oscillations. As a consequence, they are used in a combination with a filter that removes those high wavenumber oscillations. This strategy generally results in very low amounts of numerical dissipation and is commonly used for computational aeroacoustics, [7, 5]. This scheme has been also adopted here to ensure flow gradients are accurately captured and turbulent structures are well preserved.

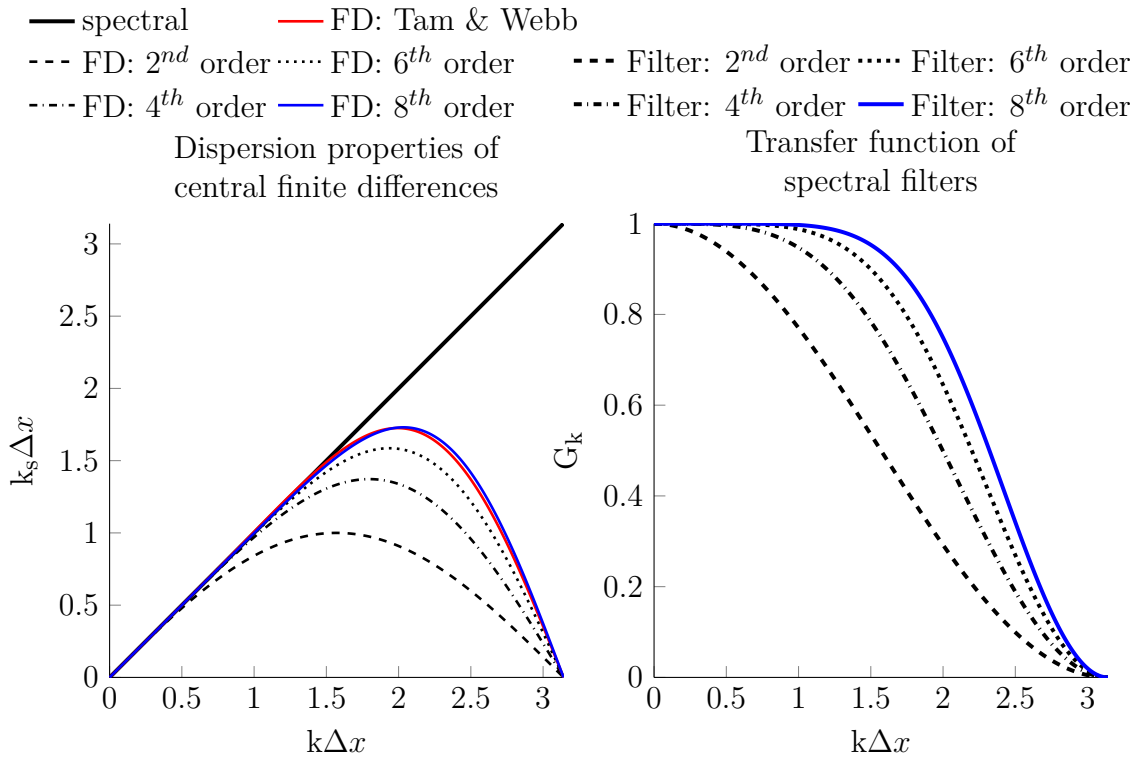

Figure 3.1: Dispersive properties of central finite difference schemes (left) and transfer functions of filtering schemes (right).

3.1.2 Dispersion considerations

In addition to dissipative errors, numerical schemes also results in dispersive errors, i.e. relating to the propagation speed of the waves. This property is crucial for accurate propagation of sound waves, but has been also shown to affect transition prediction as shown by, e.g. Souza et al. [96] for natural transition. Low dispersive errors can be achieved with the use of high-order schemes, i.e. using longer stencils. Further still, finite difference schemes can be optimised against dispersion relations. This is achieved by changing finite difference coefficients so that the finite difference approximation of Navier-Srokes equations in frequency and wave number space matches the space and time Fourier transforms of Navier-Stokes equations. This process changes the truncation error of the scheme and lowers its formal order, but improves dispersion properties. Tam and Webb [99] were first to apply this method to arrive at the Dispersion-Relation-Preserving (DRP) scheme. This scheme offered better dispersive properties than 6^{th} order central scheme while using the stencil of the same length. Dispersion properties of various schemes can be measures by looking at their effective wavenumber plots, Figure 3.1, while their resolution can be compared by calculating the number of points they require to resolve a wavelength, Table 3.1. Figure 3.1 and Table 3.1 show the performance of standard central finite difference schemes of various orders along with the performance of DRP scheme of Tam&Webb.

$$PPW = \frac{2\pi}{G_k} \tag{3.1}$$

Scheme	$4^{th} order$	$6^{th} order$	$8^{th} order$	7-point stencil Tam and Webb
PPW	8.4	7.0	5.7	4.5

Table 3.1: Points-per-wavelength for various FD schemes.

It can be seen from Figure 3.1 that central finite difference schemes are not able to resolve all the wavenumbers. As a result they may produce spurious grid-to-grid oscillations that can lead to numerical instabilities. These instabilities have to be removed without affecting the longer physical waves. This is achieved with a selective filter which is able to cut-off wave-numbers which are too high. Figure 3.1 shows the performance of standard filters of various order. These schemes were tested and benchmarked on a Taylor-Green vortex canonical test-case in Chapter 4 to demonstrate how their formulation affects simulation's ability to capture entropy generation rate.

3.1.3 Aliasing considerations

Another important source of error is aliasing errors. These errors arise during the evaluation of the convective terms and often manifest in the energy spectra. They result in an accelerated decay of energy at low wavenumbers and an unphysical accumulation of energy at high wavenumbers. Selective filters alleviate some of the aliasing problems as they remove high wavenumber oscillations and the aliased energy they carry, however, they do not compensate for the energy lost at low wavenumbers and may result in excessive dissipation.

This problem may be addressed with the use of skew-symmetric formulation of convective derivatives, Kennedy and Grubber [47]. Such formulation ensures that aliasing errors are minimised. For simple quadratic derivative skew-symmetric splitting can be formulated as:

$$\frac{\partial}{\partial x}(ab) = \frac{1}{2}\frac{\partial}{\partial x}(ab) + \frac{1}{2}a\frac{\partial(b)}{\partial x} + \frac{1}{2}b\frac{\partial(a)}{\partial x} \tag{3.2}$$

For incompressible Euler equations this formulation leads to kinetic energy conservation. Similar formulation has been implemented in 3DNS and tested in Chapter 4 on Taylor-Green vortex test case. Figure 3.2 demonstrates the effect of skew-symmetric formulation on Taylor-Green vortex energy spectrum solved with an 8^th order central finite difference scheme with a matched filter.

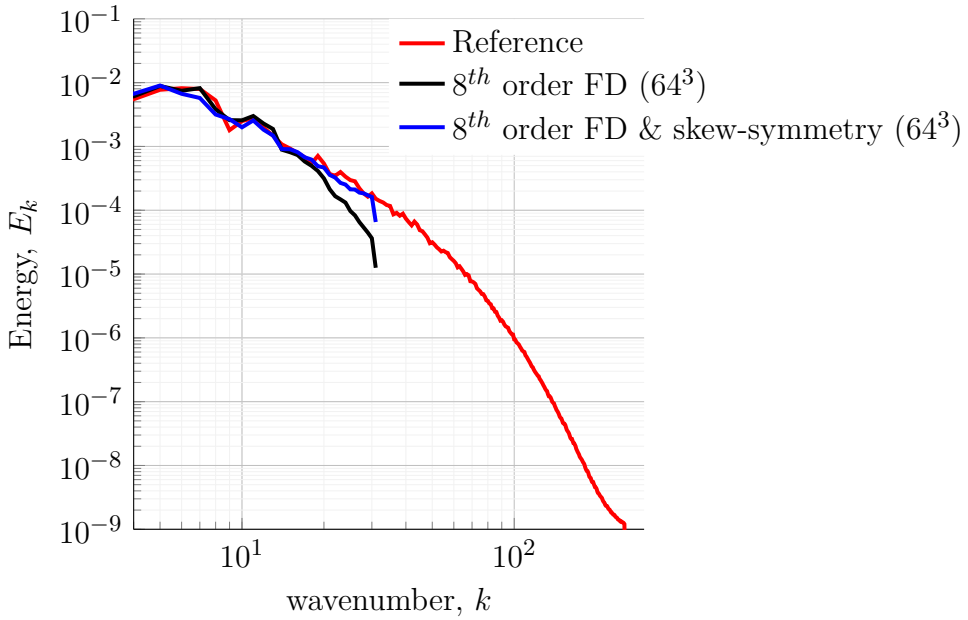

Figure 3.2: The effect of skew-symmtric splitting treatment on Taylor-Green vortex spherical spectrum.

3.1.4 Boundary schemes

High-order finite difference schemes need special care when handling physical and numerical boundaries, otherwise they may suffer from instabilities when solved for long periods of time. Carpenter et al. [11, 12] demonstrated a methodology that allows to construct high-order finite difference schemes for boundary points that ensure time-stability property. Their methodology relies on the approximation to the first derivative that satisfied summation-by-parts (SBP) rule. The authors showed further that while SBP formula alone does not guarantee stability, it is necessary to construct time-stable boundary schemes. This is achieved using simultaneous approximation term (SAT) procedure that solves a linear combination of the boundary conditions and the differential operator near the boundary by posing the boundary conditions in the form of a forcing function. Such SBP-SAT formulation is shown to ensure strict stability, [11], and has been selected for 3DNS solver.

3.1.5 Grid metrics

To solve Navier-Stokes equations on arbitrary body-fitted curvilinear grids, a mapping from physical to computational domain has to be introduced, also shown in Figure 3.3.

$$\begin{aligned} \xi &= \xi(x,y,z) \\ \eta &= \eta(x,y,z) \\ \zeta &= \zeta(x,y,z) \end{aligned} \tag{3.3}$$

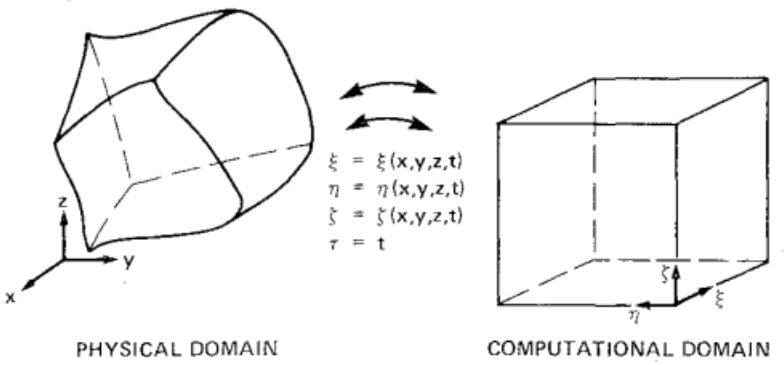

Figure 3.3: Mapping between physical an dcomputational domain, from Pulliam and Steger [84].

Navier-Stokes equations are then transformed from physical domain:

$$\partial_t q + \partial_x(F - F_\nu) + \partial_y(G - G_\nu) + \partial_z(H - H_\nu) = 0 \tag{3.4}$$

to a computational domain using chain rule for partial derivatives. The resulting equations are then of the following form (following the notation by Pulliam and Steger [84]:

$$\partial_t \hat{q} + \partial_\xi(\hat{F} - \hat{F}_\nu) + \partial_\eta(\hat{G} - \hat{G}_\nu) + \partial_\zeta(\hat{H} - \hat{H}_\nu) = 0 \tag{3.5}$$

where $\hat{q}$ are conserved variables:

$$q = J^{-1}(\rho,\, \rho u,\, \rho v,\, \rho w,\, \rho E)^T \tag{3.6}$$

$\hat{F}, \hat{G}, \hat{H}$ are inviscid fluxes and $\hat{F}_\nu, \hat{G}_\nu, \hat{H}_\nu$ are viscous fluxes, e.g.:

$$\begin{aligned} \hat{F} &= J^{-1}(\rho U,\, \rho u U + \xi_x p,\, \rho v U + \xi_y p,\, \rho w U + \xi_z p,\, \rho U(E + p/\rho))^T \\ \hat{G} &= J^{-1}(\rho V,\, \rho u V + \xi_x p,\, \rho v V + \xi_y p,\, \rho w V + \xi_z p,\, \rho V(E + p/\rho))^T \\ &\text{etc.} \end{aligned} \tag{3.7}$$

and

$$\begin{aligned} U &= \xi_x u + \xi_y v + \xi_z w \\ V &= \eta_x u + \eta_y v + \eta_z w \\ W &= \zeta_x u + \zeta_y v + \zeta_z w \end{aligned} \tag{3.8}$$

Finally the metric terms are obtained from chain rule expansions to give:

$$\begin{aligned} \xi_x &= J(y_\eta z_\zeta - y_\zeta z_\eta) \\ \eta_x &= J(z_\xi y_\zeta - y_\xi z_\zeta) \\ \zeta_x &= J(y_\xi z_\eta - z_\xi y_\eta) \\ &\text{etc.} \end{aligned} \tag{3.9}$$

and the grid Jacobian is computed according to:

$$J^{-1} = x_\xi y_\eta z_\zeta + x_\zeta y_\xi z_\eta + x_\eta y_\zeta z_\xi - x_\xi y_\zeta z_\eta - x_\eta y_\xi z_\zeta - x_\zeta y_\eta z_\xi \tag{3.10}$$

The details and derivations of these formulations can be found in Pulliam and Steger [84]. However, these authors also showed that errors can be incurred when calculating the metric coefficients using central difference operators. Thomas and Lombard [100]

remedied this problem by rewriting these metrics in the following conservative form:

$$\begin{aligned} \xi_x &= J[(y_\eta z)_\zeta - (y_\zeta z)_\eta] \\ \eta_x &= J[(z_\xi y)_\zeta - (y_\xi z)_\zeta] \\ \zeta_x &= J[(y_\xi z)_\eta - (z_\xi y)_\eta] \\ &\text{etc.} \end{aligned} \tag{3.11}$$

This final formulation has been used in 3DNS albeit simplified for the uniform spanwise mesh distribution.

3.2 Boundary conditions

Specifying inlet and outlet boundary conditions for unsteady compressible simulations still remains a challenge. Unlike steady simulations, unsteady compressible simulations require careful control of wave reflections from the boundaries. Otherwise, pressure oscillations (many of which occur during the solution initialisation) are reflected from the inlet and outlet boundaries into the domain and preserved for long periods of time leading to non-physical standing pressure waves. This is particularly true when high-order numerical schemes are used and spurious waves cannot be eliminated through, e.g. the numerical dissipation, [82]. One way to address this problem is through the use of characteristic boundary conditions.
In Chapter 5 characteristic boundary conditions coupled with the inlet sponge zone were used to minimise the effect of reflecting pressure waves. The inlet sponge zone extended to around 15 points from the inlet. Within that zone, flow variables were damped towards the prescribed inflow conditions with the strength of damping dependent on the distance from the inflow (the closer to inflow the stronger the damping). Such treatment has been widely adopted due to its robustness in eliminating pressure wave reflections, however, it has a major impact on the inflow turbulence. This can be observed in Chapter 5, Figure 5.2 which shows turbulence intensity evolution at a midpitch of a domain. It is clear that the sponge zone is affecting turbulence evolution near the inlet, but small distance downstream, turbulence appears recovered and no longer affected as its evolution matches the reference relatively well.

For the characteristic boundary conditions, the implementation followed the methodology established by Poinsot and Lele who in their paper applied the characteristic analysis to Navier-Stokes equations and obtained the characteristic waves and associ-

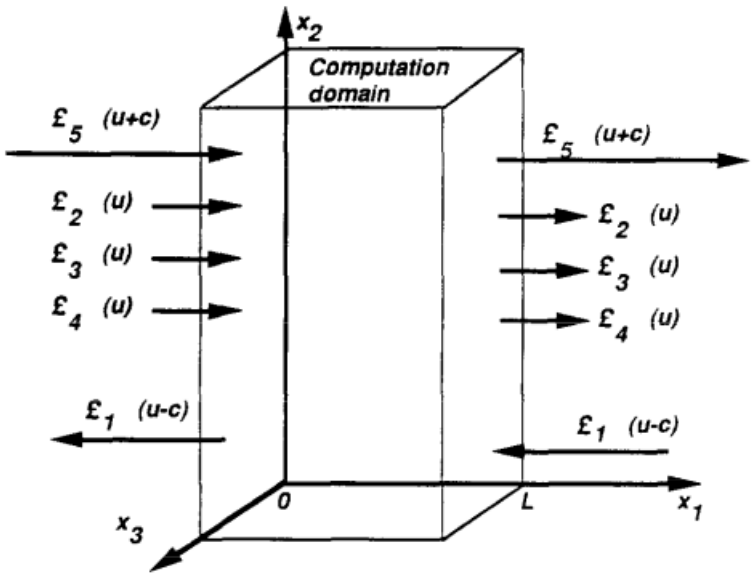

Figure 3.4: Inlet and outlet boundary conditions, and respective characteristic waves, from Poinsot and Lele [82].

ated with then characteristic velocities, Figure 3.4. The amplitudes of characteristic waves were given by:

$$\begin{aligned}
\mathcal{L}_1 &= (u-c)\left(\frac{\partial p}{\partial x} - \rho c \frac{\partial u}{\partial x}\right) \\
\mathcal{L}_2 &= u\left(c^2\frac{\partial \rho}{\partial x} - \frac{\partial p}{\partial x}\right) \\
\mathcal{L}_3 &= u\frac{\partial v}{\partial x} \\
\mathcal{L}_4 &= u\frac{\partial w}{\partial x} \\
\mathcal{L}_5 &= (u+c)\left(\frac{\partial p}{\partial x} + \rho c \frac{\partial u}{\partial x}\right)
\end{aligned} \tag{3.12}$$

Where $\mathcal{L}_1$ and $\mathcal{L}_5$ correspond to the inward and outward travelling sound waves, $\mathcal{L}_2$ corresponds to the entropy wave while $\mathcal{L}_3$ and $\mathcal{L}_3$ represent transervse shear waves. While the outgoing waves ($\mathcal{L}_1$ for the inlet and $\mathcal{L}_{2-5}$) can be easily calculated from the values within the domain, there is no exact method to do the same for the outgoing waves. For that purpose Poinsot and Lele employ Local One-Dimensional Inviscid

(LODI) approach resulting in the following set of relations:

$$\begin{aligned}
\frac{\partial \rho}{\partial t} + \frac{1}{c^2}\left[\mathcal{L}_2 + \frac{1}{2}(\mathcal{L}_5 + \mathcal{L}_1)\right] &= 0 \\
\frac{\partial p}{\partial t} + \frac{1}{2}(\mathcal{L}_5 + \mathcal{L}_1) &= 0 \\
\frac{\partial u}{\partial t} + \frac{1}{2\rho c}(\mathcal{L}_5 - \mathcal{L}_1) &= 0 \\
\frac{\partial v}{\partial t} + \mathcal{L}_3 &= 0 \\
\frac{\partial w}{\partial t} + \mathcal{L}_4 &= 0
\end{aligned} \tag{3.13}$$

For the inflow boundary conditions the velocities u, v, w, density ρ and flow angle *alpha* were selected to be imposed. As a result there were four physical boundary conditions and one numerical boundary condition for pressure p. To fully determine the conditions at the boundary, all characteristic waves $\mathcal{L}_i$ have to be computed. $\mathcal{L}_1$ can be computed from the interior points within the domain. The remaining characteristic waves were calculated using LODI relations. In addition, to prevent a drift in boundary conditions a linear relaxation approach was used, and all temporal derivatives were specified as follows:

$$\frac{\partial X}{\partial t} = -\sigma_x(X_{predicted} - X_{target})/dt \tag{3.14}$$

Where X is a variable of choice and σ_x is a relaxation coefficient (typically chosen to be between 0.05 and 0.5). Predicted and target values correspond to a value predicted by the numerical scheme and a target value imposed at the boundary condition, respectively.

Outflow boundary conditions were set in an analogous manner. In this case characteristic waves $\mathcal{L}_{2-5}$ can be computed from the internal points. The only remaining characteristic that requires a numerical boundary condition is characteristic wave $\mathcal{L}_1$ which again can be computer from the LODI relations. As only one physical condition is required to complete the system, exit static pressure p_{out} was selected to be specified. Figure 3.5 shows how the introduction of the characteristic boundary conditions and sponge zone eliminated the spurious pressure fluctuations.

For Chapter 6 and 7 inlet characteristic boundary conditions were modified to eliminate the need for the inlet sponge zone and ensure correct turbulence evolution. The formulation followed the one outlined by Odier et al. (2019) [74] who re-wrote the characteristic wave equations such that total pressure p_0, total temperature T_0 and flow angle α could be imposed at the inlet (as opposed to the velocities, temperature

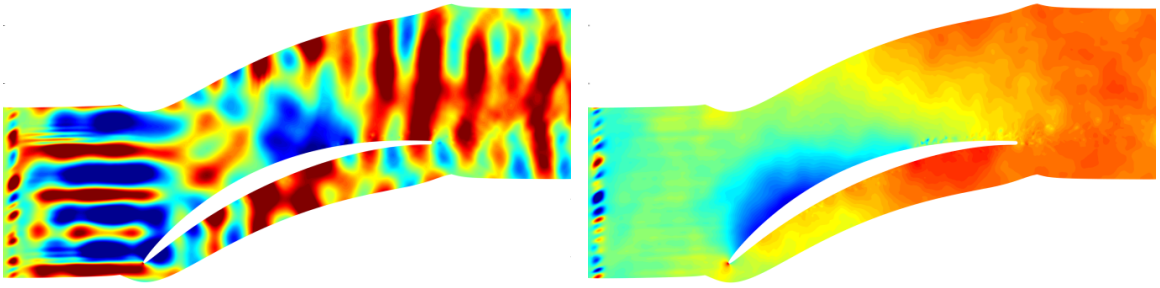

(a) (b)

Figure 3.5: The effect of improved inlet characteristic boundary conditions on static pressure field, Poinsot and Lele [82] formulation.

and flow angle as per original Poinsot and Lele formulation):

$$
\begin{aligned}
\mathcal{L}_1 &= 0 \\
\mathcal{L}_2 &= \left(\frac{\partial T_0}{\partial t} + \frac{F_3}{C_p} - F_5 \mathcal{L}_5 - F_7 \mathcal{L}_1) \right) / F_2 \\
\mathcal{L}_3 &= -\frac{\partial v}{\partial t} \\
\mathcal{L}_4 &= -\frac{\partial w}{\partial t} \\
\mathcal{L}_5 &= \left(F_1 \frac{\partial T_0}{\partial t} + F_2 \frac{\partial p_0}{\partial t} + F_2 F_3 \frac{p_0}{RT_o} + F_1 F_3 \frac{1}{C_p} - \mathcal{L}_1 \left(F_2 F_6 + F_1 F_7 \right) \right) / \left(F_4 F_2 + F_5 F_1 \right)
\end{aligned}
\tag{3.15}
$$

where:

$$
\begin{aligned}
F_1 &= \frac{e_c}{\rho} \frac{p_0}{RT_0} \\
F_2 &= \frac{T_0}{\rho} - \frac{e_c}{\rho C_p} \\
F_3 &= \mathcal{L}_3 v + \mathcal{L}_4 w \\
F_4 &= \left(-\frac{\rho c}{2} \frac{p_0}{p} + \frac{p_0}{RT_0} \left(\frac{\beta e_c}{2c} - \frac{u}{2} \right) \right) \\
F_5 &= \left(-\frac{\beta T_0}{2c} + \frac{1}{C_p} \left(\frac{\beta e_c}{2c} - \frac{u}{2} \right) \right) \\
F_6 &= \left(-\frac{\rho c}{2} \frac{p_0}{p} + \frac{p_0}{RT_0} \left(\frac{\beta e_c}{2c} - \frac{u}{2} \right) \right) \\
F_7 &= \left(-\frac{\beta T_0}{2c} + \frac{1}{C_p} \left(\frac{\beta e_c}{2c} - \frac{u}{2} \right) \right)
\end{aligned}
\tag{3.16}
$$

and

$$\begin{aligned} e_c &= \frac{1}{2}\left(u^2+v^2+w^2\right) \\ \beta &= 1-\gamma \\ c &= \sqrt{\gamma p/\rho} \end{aligned} \tag{3.17}$$

While the need for the inlet sponge was eliminated using the formulation by Odier et al., it was found that their implementation resulted in the incorrect strain friel upsteam of the blade. This was attributed to a close proximity of the inlet of the domain to the leading edge of the blade. This problem was remedied by the addition of the first characteristic (which was set to zero by Odier et al.):

$$\mathcal{L}_1 = (u-c)\left(\frac{\partial p}{\partial x}\frac{1}{\rho c} - \frac{\partial u}{\partial x}\right) \tag{3.18}$$

Further testing have shown that the addition of the first characteristic did not affect non-reflective properties of the inlet boundary conditions. Figure 3.6 demonstrates the improvement in static pressure flowfield with the new boundary conditions and without the inlet sponge zone.

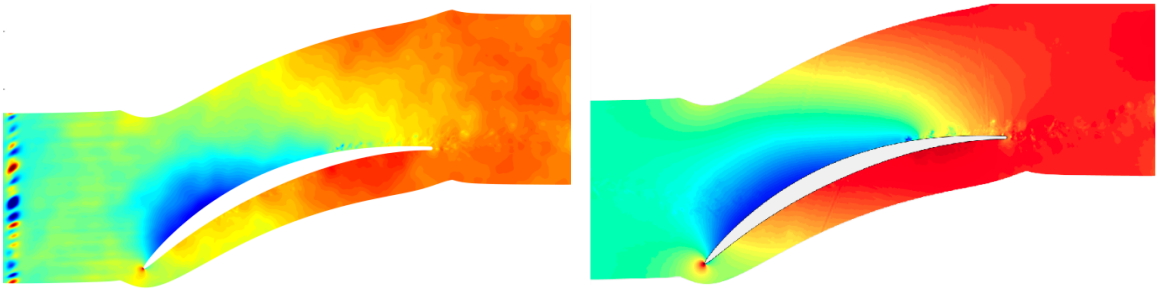

(a) (b)

Figure 3.6: The effect of improved inlet characteristic boundary conditions on static pressure field, Odier et a. [74] formulation.

3.3 Inflow turbulence

The inflow turbulence used here has been produced with a modified TURBID code by Phillips and Fyfe, [76]. The output of the code consists of random, spatially correlated signals. The correlation is achieved via a Gaussian digital filter with manually selected length scales in three dimensions. Signal obtained this way is read into 3DNS every certain number of iterations and added to the inflow through the characteristic boundary conditions. The frequency at which inflow turbulence signal is read depends on the desired streamwise lengthscale.
It is a very efficient method of generating turbulence data and has been validated on a variety of cases. Figure 3.7 shows the example performance of this method for a compressor blade flowfield. For Chapter 5 turbulence lengthscales were selected to correspond to roughly $3\%C_{ax}$. Turbulence intensity was controlled through a parameter that scales the disturbances to the desired intensity level.

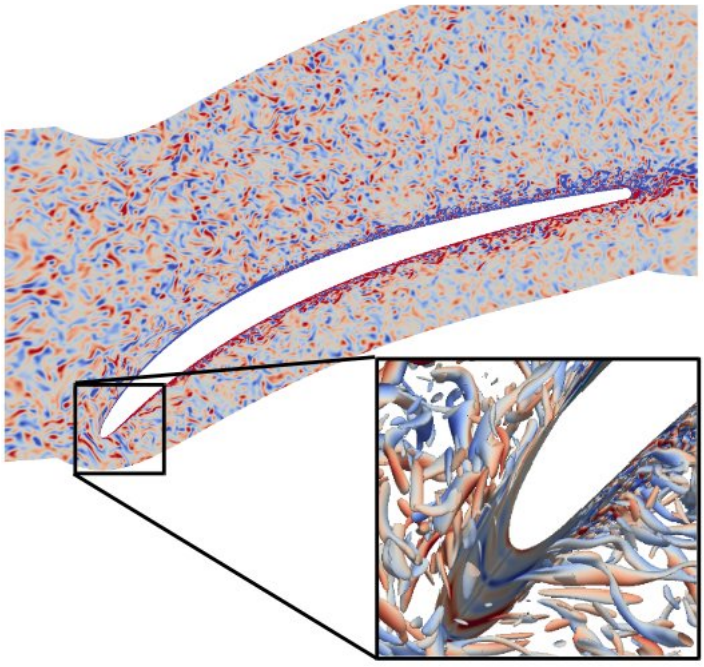

Figure 3.7: Iso-surfaces of Q-criterion of compressor flow with inflow turbulence for representative geometry, from Wheeler et al. [113]

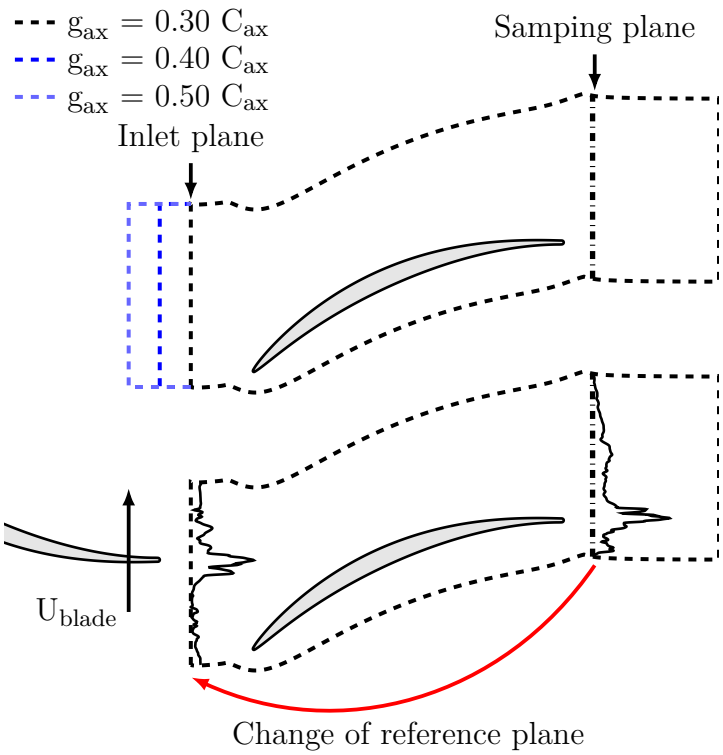

Figure 3.8: Schematic of the computational domain and wake recycling procedure.

3.4 Repeating passage model

The observation of the repeating-stage phenomenon (see Smith [95]) suggests that for a repeating stage, the turbulence is likely to develop an equilibrium state, neither growing in intensity nor decaying through the machine. This insight was used by McKenzie [59] to develop a linear repeating stage axial compressor approach, then implemented computationally by To and Miller [101]. In the original approach the following assumptions were made:

1. Hub-to-tip ratio set to 1 (blade-rows assumed to be linear cascades)
2. Stator exit condition is used as the rotor inlet condition for the next iteration
3. Flow is considered incompressible
4. Stage reaction is chosen to be 50%

This approach removes the need to specify inflow conditions and is key to establishing a repeating-passage simulation presented here. This allows to use scale-resolving simulation for the simulation of the compressor flow in a multi-stage environment,

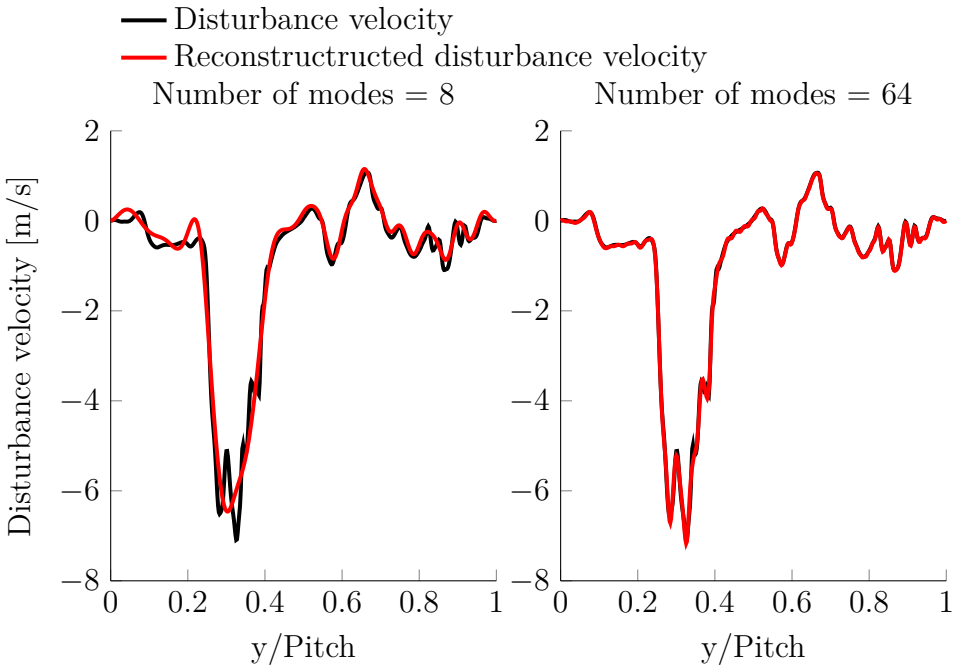

Figure 3.9: Example performance of the wake recycling procedure using different number of Fourier modes.

albeit at the mid-span.
In order to model the mid-span multi-stage environment, a new wake-recycling method was used to recreate a repeating-stage flow field. The method recycles the flow from a single-passage simulation to mimic the multi-stage flowfield which would occur assuming a stage reaction, $\Lambda = 50\%$ (stator and rotor flowfields identical). During the recycling procedure only vortical disturbances are considered and so only velocity fields are sampled and superimposed onto the inlet.

The inflow turbulence is produced by sampling the velocity profile at the sampling plane and recycling it by superimposing the disturbance field onto the inflow boundary conditions at the inlet. When adding disturbances to the inlet conditions it is also necessary to change the sign of the tangential velocity component to reflect the upstream rotor orientation. In addition, the phase of the disturbance field varies linearly with time to replicate the rotor blade speed. A schematic of the sampling method is shown in Figure 3.8. Eventually, after the transient period of the simulation is passed a repeating-stage condition is obtained.

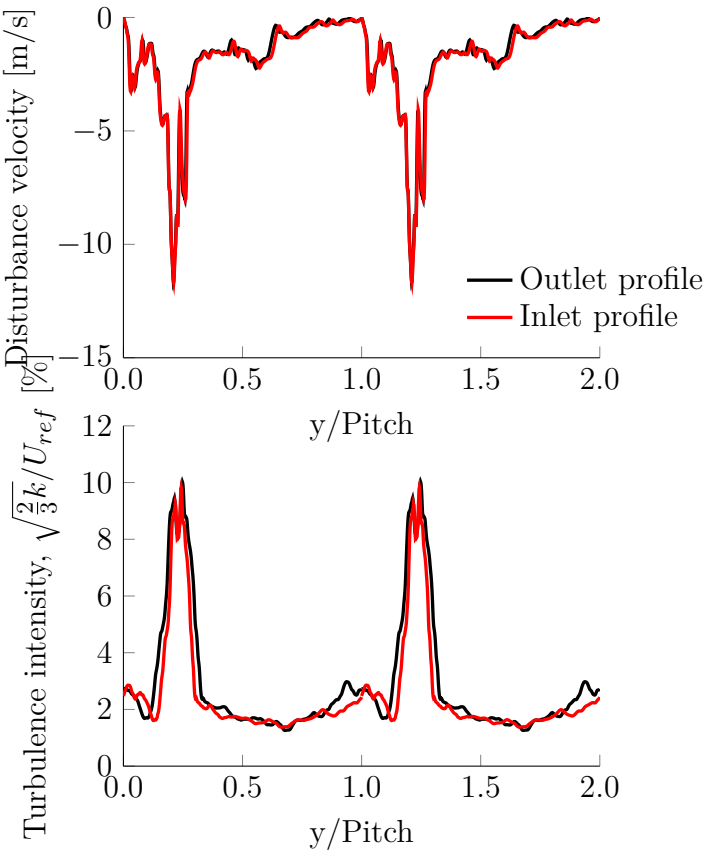

Figure 3.10: Comparison of NACA65 instantaneous disturbance velocity profile (upper) and ensemble average turbulence intensity (lower) at the inlet and at the sampling plance of the domain for the NACA65 testcase with axial gap of $0.40C_{ax}$.

3.4.1 Variation in axial gap

The axial gap is controlled by shortening/extending the inlet domain, while the sampling plane is kept at the fixed position, Figure 3.8. The effective rotor-stator axial gap is equal to the combined distance between the trailing edge and the sampling plane and the distance between the inlet and the leading edge of the blade.

3.4.2 Wake recycling

For the purpose of repeating passage model, a wake recycling procedure has been implemented for the 3DNS code. Sampling of the wake is accomplished using Fourier modes and Figure 3.9 shows the performance of this procedure on an example outlet flow profile for different number of Fourier modes. The velocity disturbance field is reconstructed using a fixed number of modes and added to linear relaxation equations

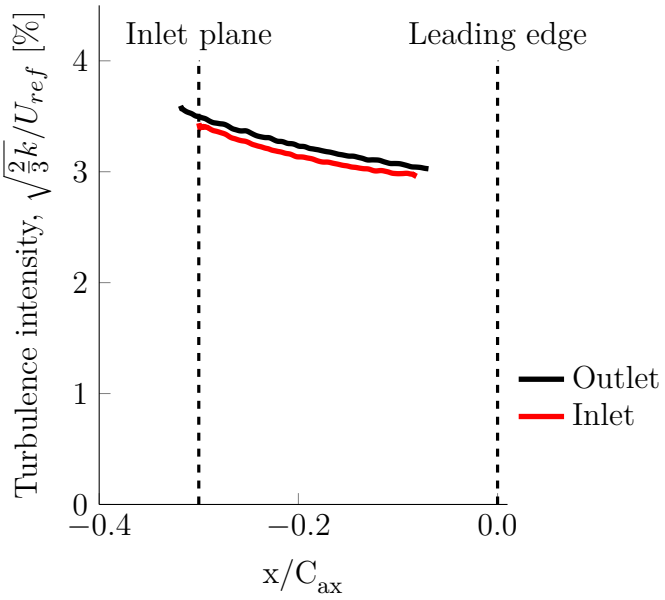

Figure 3.11: Comparison of ensemble averaged turbulence intensity evolution in the axial direction between the outlet and the inlet for the NACA65 testcase with axial gap of $0.40C_{ax}$.

for incoming waves in the inlet characteristic boundary conditions. To avoid dispersion effects related to the sampling method, the number of modes was chosen to be equal to half of the points in the pitchwise direction.

3.4.3 Verification of repeating-stage condition

In order to verify that a repeating condition is achieved, instantaneous velocity profiles and the turbulent kinetic energy at the inlet and exit of the domain were compared. This was done for a NACA65 profile with an axial gap of $g_{ax} = 0.40C_{ax}$. Figure 3.10 shows the outlet and inlet velocity profiles. The figure demonstrates that the wake is well captured by this method. To compare turbulent kinetic energy profiles the velocity is decomposed into periodic and turbulent fluctuations:

$$u(t) = \bar{u} + u^*(t) + u'(t), \tag{3.19}$$

where $\bar{u}$ is the time-averaged velocity, and the periodic and turbulent fluctuations are $u*$ and u' respectively. It is necessary to decompose the velocity before computing the turbulent kinetic energy at the inlet in order to account for the traversing wake profile. This allows for the calculation of phase-averaged (ensemble-averaged) turbulent kinetic

energy:

$$\langle k' \rangle_\phi = \frac{1}{2} \langle u_i' u_i' \rangle_\phi, \tag{3.20}$$

The repeating-passage condition is further validated by demonstrating that the ensemble-averaged turbulent kinetic energy at the sampling plane and at the inlet for each rotor phase is in agreement as shown in Figure 3.10 for one of the rotor phases. In addition, the evolution of time averaged turbulent kinetic energy, $k' = \frac{1}{2}\overline{u_i' u_i'}$ is plotted with the axial distance. Figure 3.11 shows a comparison of k' evolution at the inlet and outlet. The figure confirms that the turbulence statistics are well matched between the inlet and the outlet of the domain.

Consequently, a method enabling the study of the flow as observed by an embedded blade-row of 50% reaction machine is established. This method is used in Chapters 5 and 6 to study the loss generation, the nature of turbulence and turbulence production within a multi-stage machines.

Chapter 4

Accurate Loss Accounting

Accurate prediction of loss using high-fidelity simulations is crucial for unlocking their potential as virtual experiments. The computational requirements for capturing loss are not known leading to inconsistent loss predictions depending on the chosen convergence criteria.

The work presented in this chapter investigates the effect of resolution on loss by simulating a Taylor-Green vortex canonical flow. This test-case is of particular interest as it starts from the well defined flowfield and evolves in a specific manner to a final mixed-out state. As such, its total loss is fixed and path independent. It therefore allows to study the effect of resolution on flow evolution and loss generation rate between two fixed states.

To achieve that, the loss is first related to the entropy generation rate. Later, it is shown how resolution affects simulations ability to capture viscous dissipation and entropy generation rate. Further insight is gained by performing a series of simulations with various numerical schemes and comparing their accuracy. The chapter concludes with a recommendation for grid resolution that ensures correct entropy generation rate prediction.

4.1 Computational setup

Taylor-Green vortex canonical flow is used to study the effect of numerical resolution on capturing entropy generation rate. The initial flowfield is inviscidily unstable and so leads to a spontaneous breakdown to turbulence. This case is conventionally used to test and benchmark the capabilities of high-fidelity codes with regards to capturing transition and turbulence and has been used by many authors, [106, 23, 22, 9]. The problem is solved in a cubic, periodic domain $\Omega = \{0 \leq (x, y, z) \geq 2\pi\}$ at a Reynolds

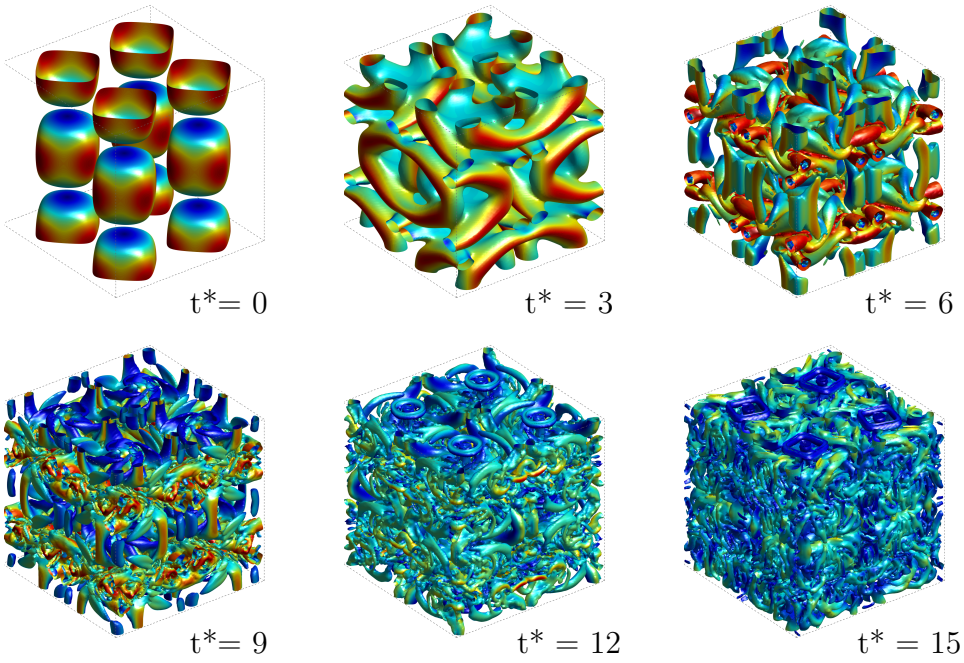

Figure 4.1: Evolution of iso-surfaces of Q-criterion ($Q = 0.1(u_0/L)^2$) colored with the non-dimensional velocity magnitude u/u_{max}. The solution has been computed with the 8^{th} order scheme on the 128^3 grid using 3DNS.

number $Re = \frac{\rho_0 u_0 L}{\mu} = 1600$. The initial distribution of velocity and pressure is specified by:

$$\begin{aligned} u(t_0) &= u_0 \sin\frac{x}{L}\cos\frac{y}{L}\cos\frac{z}{L} \\ v(t_0) &= -u_0 \cos\frac{x}{L}\sin\frac{y}{L}\cos\frac{z}{L} \\ w(t_0) &= 0 \\ p(t_0) &= p_0 + \frac{\rho_0}{16}\left[\cos\frac{2x}{L} + \cos\frac{2y}{L}\right]\left[\cos\frac{2z}{L} + 2\right] \end{aligned} \tag{4.1}$$

The evolution of the flow is showed in Figure 4.1 in which the iso-surfaces of Q-criterion are visualized at three different instances.

The accuracy of the code is verified by comparing results with those of von Rees [106] who performed a spectral simulation of the Taylor-Green vortex. Figure 4.2 shows the integrated enstrophy and energy spectra at $t^* = 9$ comparison. Energy spectra were computed using spherical spectra. For this comparison the standard 8^{th} order central finite difference scheme in combination with a standard 8^{th} order filter is used.

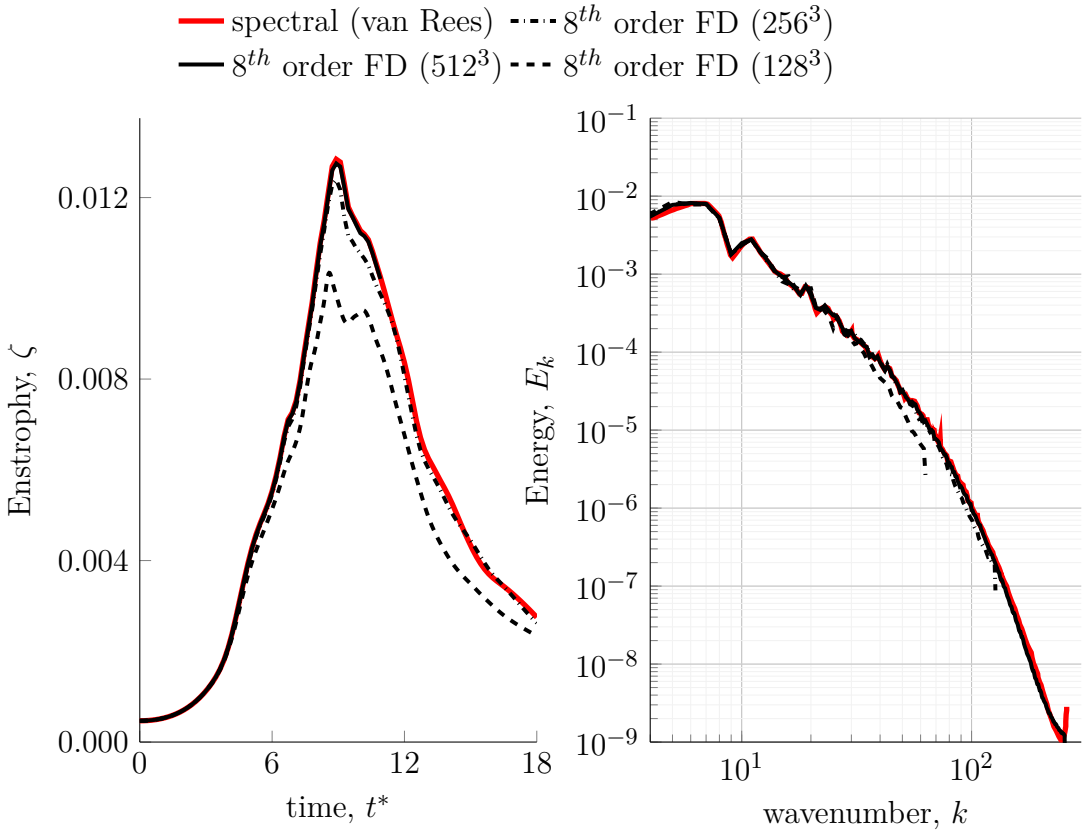

Figure 4.2: Comparison of volume averaged enstrophy (left) and energy spectra at $t = 9$ (right) between 3DNS and spectral solution [106].

It can be seen that as the mesh resolution is increased, convergence onto the spectral solution is achieved.

4.2 Loss accounting using entropy generation rate

Loss can be related to the rate of change of entropy within a control volume, Denton [24]. In this study, the entropy budgets are used as a mean of accurately determining the effect of resolution on loss prediction. Direct numerical simulation and implicit large-eddy simulation (i.e., simulations where no turbulence model is used) are the focus of this study. For these simulations the entropy generation rate, or material derivative of entropy, is given by:

$$\rho \frac{Ds}{Dt} = \frac{\phi}{T} + \kappa \frac{(\nabla T)^2}{T^2} - \nabla \cdot \frac{q}{T} + \epsilon_N \tag{4.2}$$

where the first term on the right-hand-side is the irreversible entropy change due to viscous friction and the second and third terms are the irreversible and reversible changes in entropy due to heat transfer. The fourth term, ϵ_N, comes about due to the combined effects of discretization errors and numerical filtering (artificial dissipation). The total calculated loss will be the integration of Equation 4.2 over the computational domain. For the cases considered in this paper, integrated heat transfer terms are negligible and thus:

$$\int_\Omega \rho \frac{Ds}{Dt} d\Omega = \int_\Omega \left(\frac{\phi}{T} + \epsilon_N \right) d\Omega \tag{4.3}$$

Equation 6.1 suggests that in order to achieve an accurate prediction of loss, there are two choices. Either the effects of artificial dissipation is eliminated by capturing all the dissipative scales in the flow or a model or algorithm which accurately accounts for the effects of unresolved scales is selected. In order to determine how resolution affects the loss prediction and the role numerical dissipation plays in entropy generation rate the net contributions from the resolved and un-resolved dissipation need to be determined. Recalling equation 6.1 three metrics are defined:

$$\begin{aligned} \epsilon_S &= \int_\Omega T \rho \frac{Ds}{Dt} d\Omega \\ \epsilon_\phi &= \int_\Omega \phi d\Omega \\ \epsilon_N &= \epsilon_S - \epsilon_\phi \end{aligned} \tag{4.4}$$

These represent the total entropy generation within the volume ϵ_s and the entropy generation rate due to resolved dissipation ϵ_ϕ. The difference between these two metrics, ϵ_N is the effect of artificial dissipation due to discretization and filtering.
Calculation of the dissipation function can be furthered simplified. Lamb, [51] showed that for the incompressible flow the following formulation is true:

$$\int_\Omega \phi d\Omega = \mu \int_\Omega \omega^2 d\Omega + 2\mu \int_S \left(\mathbf{u} \times \omega - \nabla \frac{u^2}{2} \right) \cdot \mathbf{n} dS \tag{4.5}$$

Using the argument of domain periodicity the second term can be ignored when integrated over the volume, thus relating dissipation function with enstrophy :

$$\begin{aligned} \int_\Omega \Phi d\Omega &= \mu \int_\Omega \omega^2 d\Omega \\ \epsilon_\phi &= \mu \int_\Omega \omega^2 d\Omega \end{aligned} \tag{4.6}$$

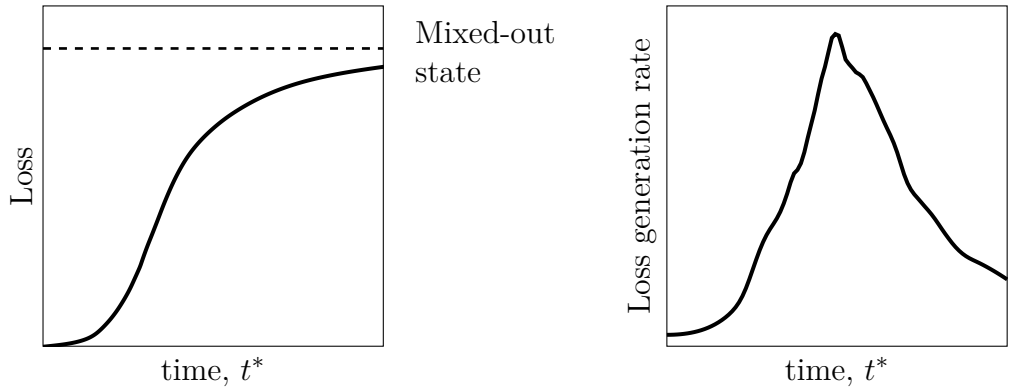

Figure 4.3: Evolution of Taylor-Green vortex from initial flowfield to the mixed-out state and associated loss generation rate.

Taylor-Green vortex test-case is of particular interest as is starts from the well defined flowfield and evolves in a specific manner as it breaks down into turbulence. The initial and final states are therefore fixed with a final loss defined by the mixed-out state. This is depicted in Figure 4.3. Consequently, the loss generation rate along the path between two fixed states can be studied and it is possible to determine resolution requirements for its correct evolution.

For this analysis all the solutions were computed using the standard 8^{th} order central finite difference scheme in combination with a standard 8^{th} order filter unless otherwise specified.
In the next section the effect of resolution on resolved and un-resolved loss generation rate is explored and resolution requirements needed for the accurate prediction of loss are determined.

4.3 The effect of resolution on entropy generation rate

Figure 4.4 shows the effect of resolution on resolved dissipation, ϵ_ϕ (left) and total entropy generation rate, ϵ_s (right). It can be seen that as the mesh size is increased, resolved dissipation, ϵ_ϕ, converges onto the reference solution. The value of dissipation function depends on the resolved velocity field and so reaches the spectral resolution only when all the scales present in the flow are resolved.

Interestingly, the entropy generation rate is not significantly affected by the choice of resolution for meshes of 64^3 and above. The only solution significantly departing from the reference solution is the least resolved 32^3 mesh which fails to predict the

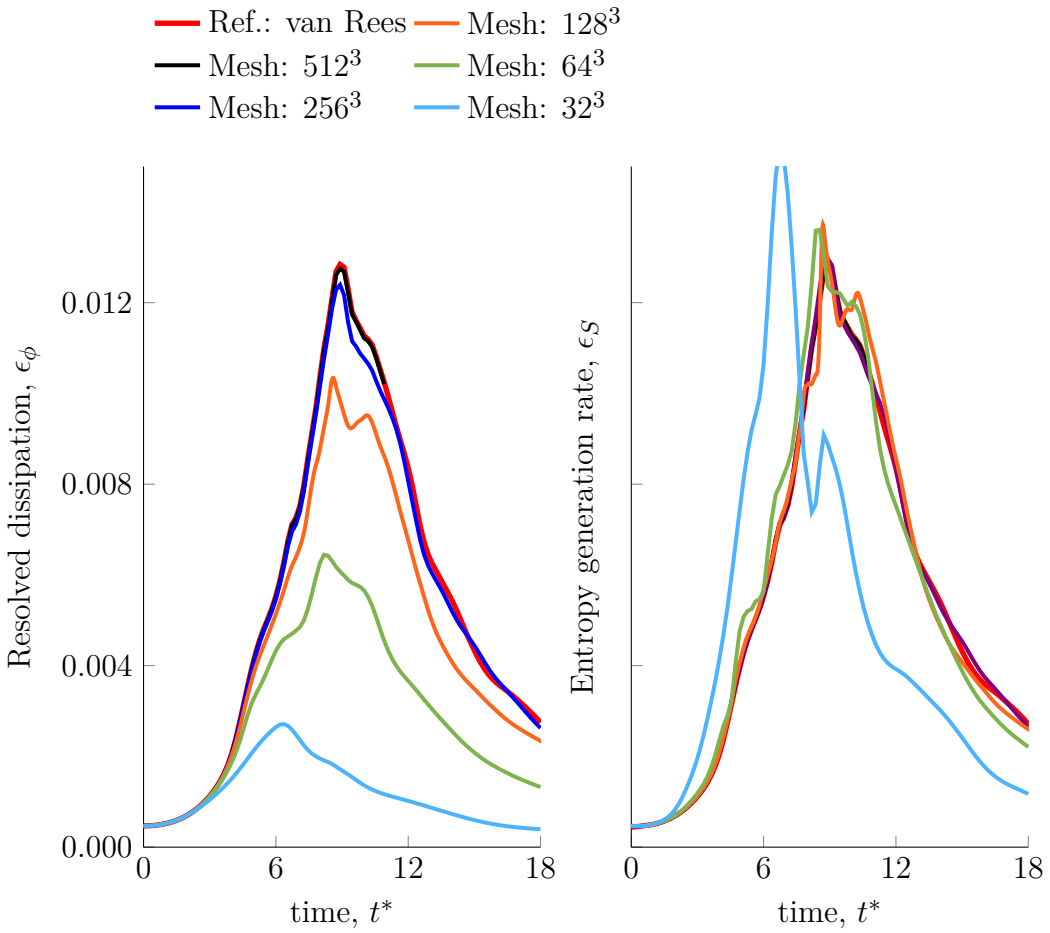

Figure 4.4: The effect of resolution on Taylor-Green vortex dissipation (left) and entropy generation rate (right).

correct breakdown to turbulence, giving rise to a peak ϵ_s and resulting in a premature turbulence breakdown.

The results suggest that capturing the full dissipation spectrum it not a necessary requirement to ensure correct prediction of entropy generation rates. This is happening because the discretization errors and implicit filtering are compensating for the unresolved dissipation and acting as an effective subgrid scale model.

To determine what is the main driver behind the compensation of unresolved dissipation, the order of the discretization and filtering schemes were modified independently. Figure 4.5 shows the effect of filter order on the resolved dissipation ϵ_ϕ. The figure shows that, 6^{th} order discretization with 8^{th} order filtering schemes achieved comparable accuracy to matched 8^{th} order discretization with filtering scheme. This suggests that the filter is compensating for the unresolved dissipation and acting as an effective

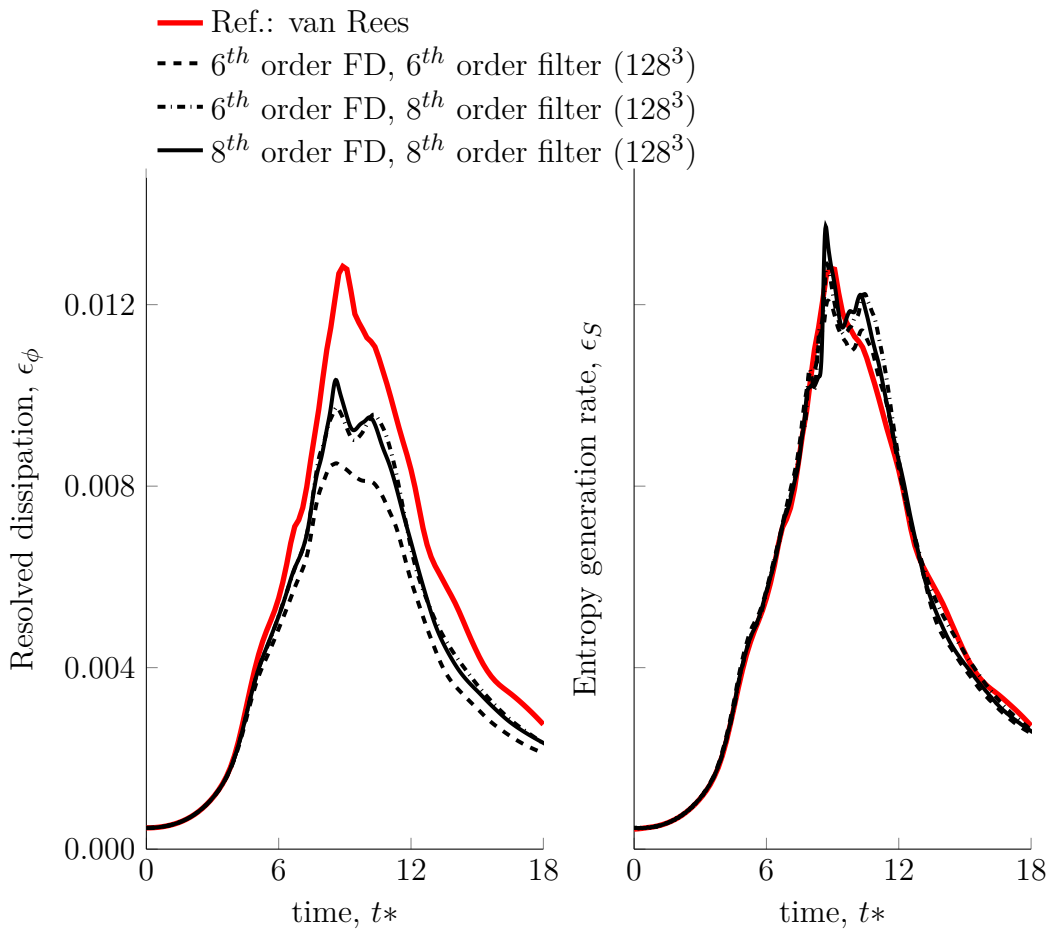

Figure 4.5: The effect of finite difference and filtering order on Taylor-Green vortex dissipation (left) and entropy generation rate (right).

subgrid scale model. However, the difference in the finite difference and filter order is limited by the stability of the scheme, i.e. a 2^{nd} order finite difference and 8^{th} order filtering scheme pairing would result in the scheme that is unstable, but 6^{th} and 8^{th} order pairing would perform well.

4.4 Resolution requirements for accurate entropy generation rate prediction

In this section the resolution requirements that ensure accurate entropy generation rate prediction are established. For this purpose a series of Taylor-Green vortex simulations is performed with mesh sizes ranging between 32^3 and 256^3. For each of these meshes a variety numerical schemes is used ranging from: standard 2^{nd} to 8^{th} order discretization

and filtering schemes, 8^{th} order discretization and filtering scheme with skew-symmetric splitting treatment on convective flux terms [47], 4^{th} order wavenumber optimized Tam&Webb scheme with 8^{th} order filter and, finally, spectral incompressible scheme following Mortensen and Langtangen [70] formulation.
For all these cases two metrics are computed: path error L_1 and normalized cut-off wavenumber $k_{cut-off}$. The first metric called path error, L_1 measures the departure from the reference path of entropy generation rate normalized by the total reference entropy generation rate according to the formula:

$$L_1 = \frac{\int_0^{18} |\epsilon_s - \epsilon_{s_{ref}}| dt^*}{\int_0^{18} |\epsilon_{s_{ref}}| dt^*} \tag{4.7}$$

The second metric, cut-off wavenumber, $k_{cut-off}$ is based on the resolved dissipation spectra $D_k = kkE_k$ shown in Figure 4.6 (right). Dissipation spectra were calculated using the spherical spectra at $t^* = 9$ (peak entropy generation rate). $k_{cut-off}$ is the wavenumber at which the resolved dissipation is 50% of the reference dissipation:

$$k_{cut-off} = D_k \leq 0.5 D_k^{ref} \tag{4.8}$$

This allows to determine the smallest resolved wavenumber relevant for loss prediction for each of the cases. We further normalise cut-off wavenumber by the Kolmogorov scale. Kolmogorov wavenumber, k_{Kol}, is computed by using:

$$\begin{aligned} \eta_{Kol} &= \left(\frac{\nu^3}{\epsilon_s} \right)^{1/4} \\ k_{Kol} &= 2\Pi / \eta_{Kol} \end{aligned} \tag{4.9}$$

Where 2Π is the size of the domain, ϵ_s is peak entropy generation rate, equal to $\epsilon_{s_{ref}} = 0.01276$. This corresponds to the maximum value of average entropy generation rate across the domain at any point in time as the solution evolves towards the mixed-out state. The Kolmogorov wavenumber computed this way was equal to $k_{Kol} \approx 535$.

Figure 4.7 shows how the entropy generation rate (path) error, L_1 changes with the cut-off wavenumber, $k_{cut-off}$ for all tested numerical schemes and meshes. It is interesting to see that all the cases collapse on the inverse wavenumber curve, ck^{-1} (dashed line) surprisingly well (c is a constant that was used to fit the data). This behavior is independent of the numerical schemes considered here.

The figures also shows that for $k_{cut-off}/k_{Kol}$ over 0.1 the path error, L_1 becomes relatively independent of mesh and order. Consequently, it is determined that for the

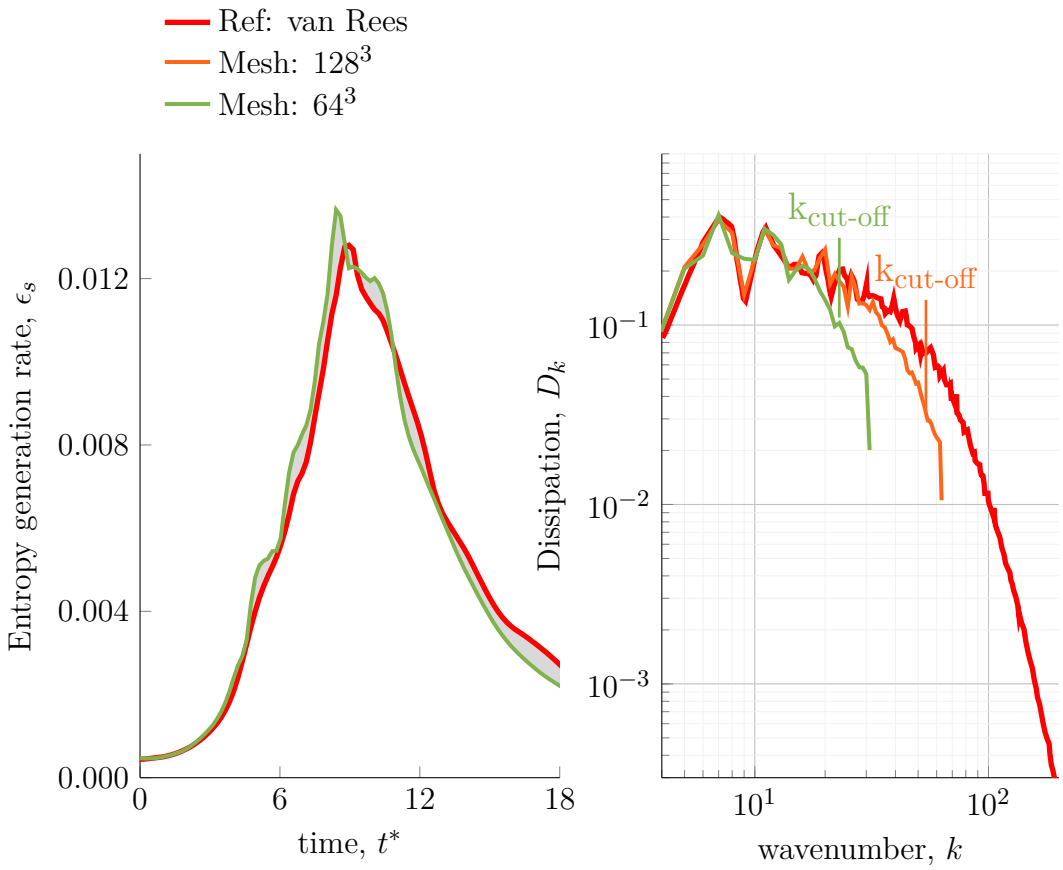

Figure 4.6: Defintion of path error, L_1, i.e. deviation of entropy generation rate from the reference solution (left) and cut-off wavenumber, $k_{cut-off}$ based on dissipation spectra at $t^* = 9$ (peak entropy generation rate) defined as the smallest wavenumber for which dissipation is lower than 50% of the reference dissipation (right).

accurate entropy generation rate prediction one needs to resolve all the scales down to around $10\eta_{Kol}$.

This result can be used to determine the cell size that ensures correct loss prediction for the numerical schemes considered. To do this a mesh resolution that reaches mesh and order independence ($\sim 0.1k_{cut-off}/k_{Kol}$) for a particular scheme is chosen. From Figure 4.7 it can be observed that for the 8^{th} order, Tam&Webb and spectral schemes such mesh resolution is 128^3. The required cell size for this scheme is therefore $\Delta = \approx 4\eta_{Kol}$.

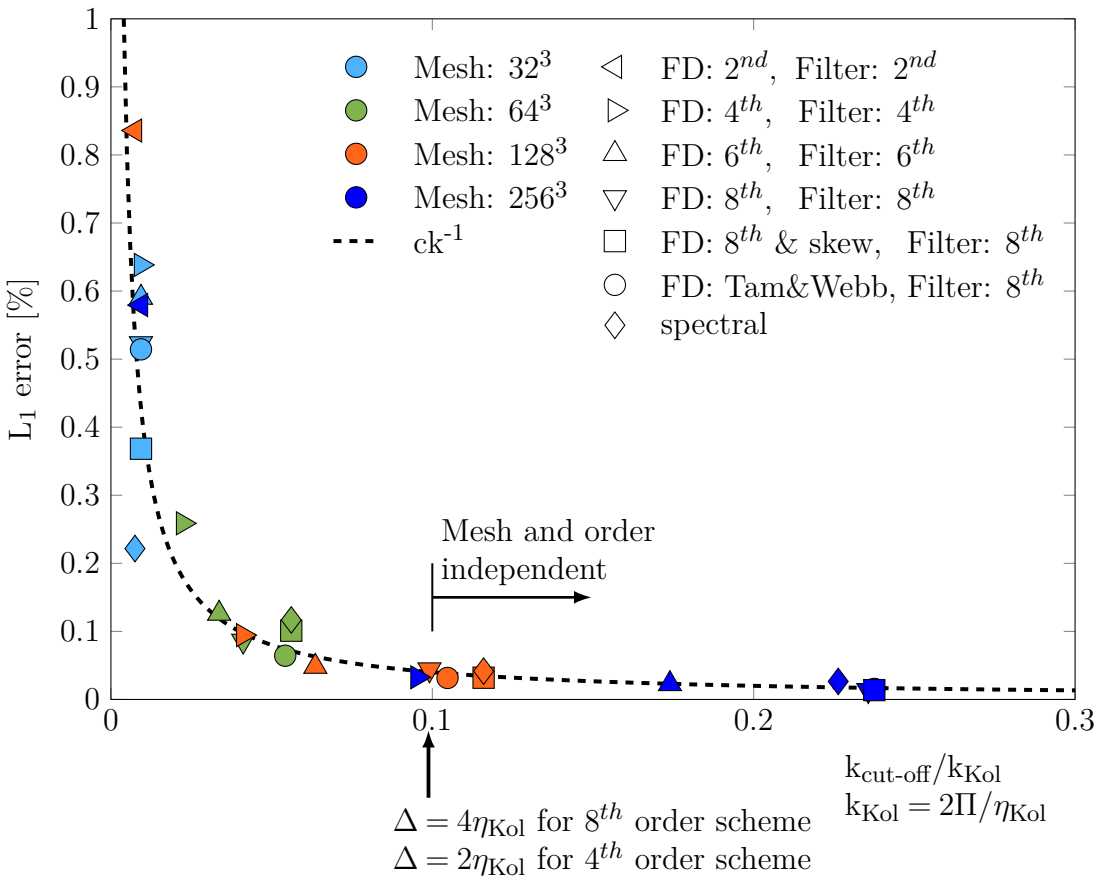

Figure 4.7: Path error, L_1, vs. cut-off wavelength, $k_{cut-off}$ for a range of numerical schemes and mesh resolutions for Taylor-Green vortex case.

4.5 Conclusions

The problem of accurate prediction of loss was addressed in this chapter. The loss was defined as the change of entropy following Denton, [24] and the accuracy was assessed using entropy transport equation budgets. For the purpose of this study a canonical Taylor-Green vortex text case was used. The initial flowfield is analytically prescribed and inviscidly unstable leading to a well defined breakdown to turbulence. The final flowfield is set by a mixed-out state. Consequently, the effect of resolution on entropy generation rate evolution is studied.

The results show that entropy generation rate is far less sensitive to the effects of resolution that resolved viscous dissipation. It is shown that given the correct initial breakdown, even under-resolved solution follow trajectory which is close to the fully resolved (spectral) solution. It is then demonstrated that solver's ability to account for unresolved scales can be credited to the effect of filtering.

Later in the chapter a series of simulations was performed with a variety of numerical schemes ranging from low to high order. It is shown that the combination of a high-order discretization and a high-order filter can achieve accurate predictions of entropy generation rate without the need for resolving the entire dissipation spectrum. Empirical resolution criterion that ensures accurate loss prediction is also demonstrated $\Delta \leq 10\eta_{Kol}$. This was found to correspond to $\Delta \leq 4\eta_{Kol}$ for a standard 8^{th} order scheme, or the 4^{th} order Tam&Webb scheme with 8^{th} order filter.

Chapter 5

Compressor Cascade Loss Prediction

In the previous chapter the effect of resolution on entropy generation rate was shown. This chapter builds upon these findings and investigates what other physical mechanisms are important to consider when making accurate loss predictions in compressor cascade flows using high fidelity simulations.
For the purpose of this analysis a NACA65 compressor cascade subjected to freestream turbulence is used. The cascade is studied at two freestream turbulence intensity levels and at the range of mesh resolutions. The chapter starts with a description of the computational setup and the case validation. Chosen mesh resolutions are then characterized according to entropy generation criterion shown in Chapter 4 and the loss audit is performed. Finally, the effect of resolution on flow physics and how it affects loss is demonstrated.

5.1 Computational setup

In this chapter a well-established NACA65 compressor blade geometry is employed. This test case was extensively studied by Zaki et al. [125–127]. The running conditions considered here are: Reynolds number of $Re_{C_{ax}} = 138,500$ and turbulence intensity at the inlet plane equal to $Tu = 6.5\%$ and $Tu = 8.0\%$ (equivalently $Tu = 4.0\%$ and $Tu = 6.0\%$ at the leading edge).
A typical mesh with multi-block structure that was used for this study is presented in the Figure 5.1. For clarity, the mesh that is shown is plotting every 8^{th} grid line. Following the method of Wheeler et al. [113], the initial mesh and block structure with block boundaries were created using the Turbogrid software. That mesh was then

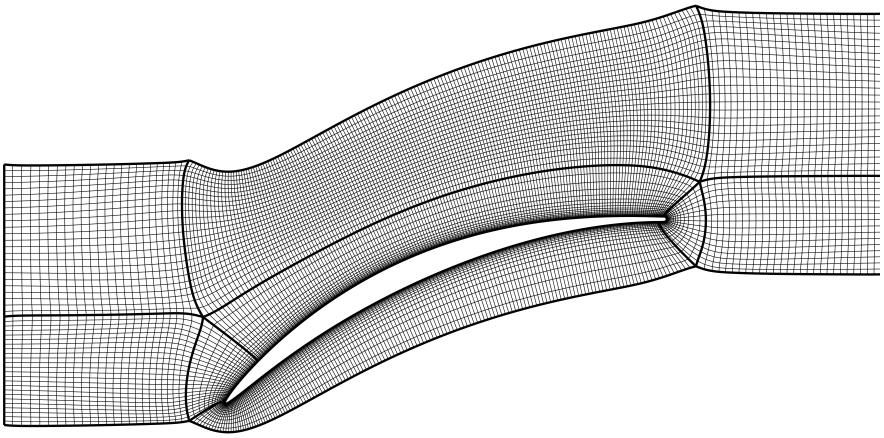

Figure 5.1: Block structure and example mesh showing every 8^{th} grid line (for 73M mesh).

Table 5.1: Test cases

Mesh size	$Re_{C_{ax}}$	Tu_{LE}	Δ_n^+	Δ_t^+	Δ_z^+
14M	138.5k	4&6%	1.2	13	20
28M	138.5k	4&6%	1.2	13	10
73M	138.5k	4&6%	1.2	8	7
102M	138.5k	4%	1.2	8	7

refined using a suite of Matlab scripts and repeated in z-direction to obtain the final 3D mesh.

Table 5.1 gives a summary of maximum viscous wall units for NACA65 compressor meshes. The $14M$ mesh comprised of roughly $444k$ nodes in the blade-to-blade plane and 32 nodes in the spanwise direction. The $32M$ mesh was constructed by doubling the spanwise mesh count (to 64). The $73M$ mesh was refined in all three dimensions resulting in around $760k$ nodes in the blade-to-blade plane and 96 nodes in the spanwise direction. Finally, the $102M$ mesh was obtained by refining the O-mesh in the wall normal direction and around trailing edge resulting in around $1,063k$ nodes in the blade-blade plane and 96 nodes in the spanwise direction. A spanwise domain extent of 10% of the axial chord was used throughout the study and periodic boundary conditions were enforced in both spanwise and pitchwise directions.

The data presented in this chapter was obtained by performing time averaging (Reynolds average) over at least 5 convective time units based on the freestream velocity

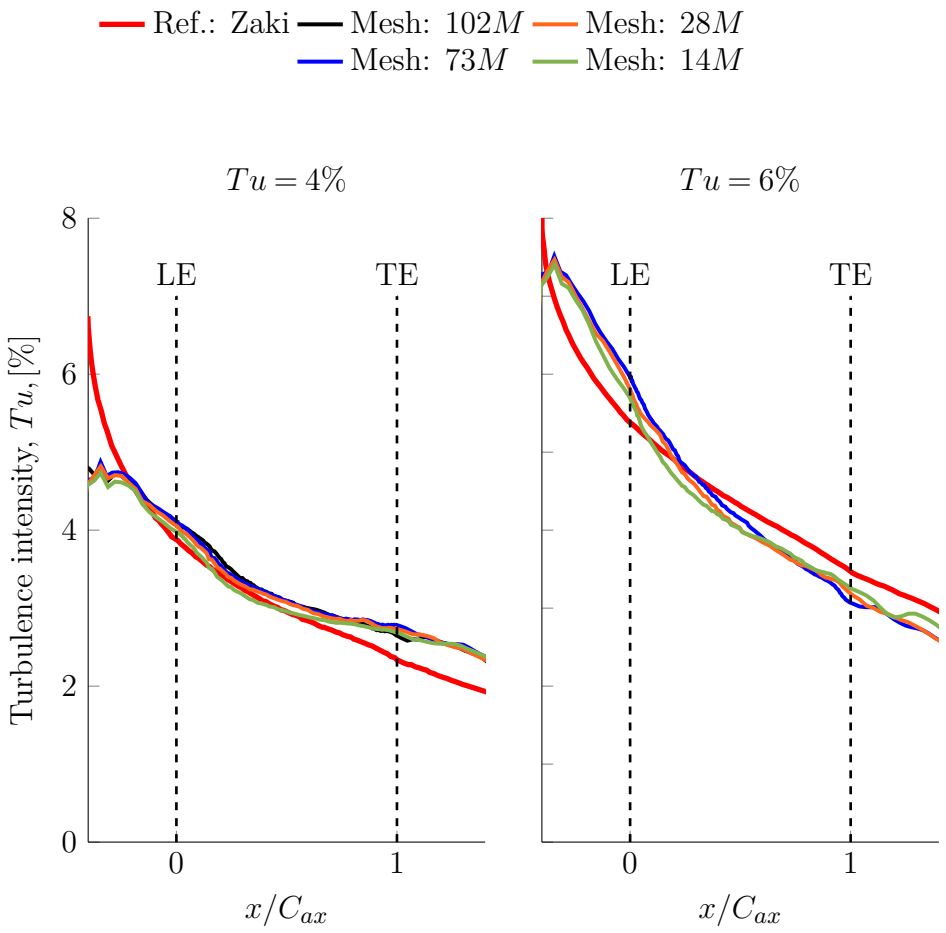

Figure 5.2: Comparison of turbulence intensity at the midpitch between 3DNS and reference solution, [127].

and the axial chord.

The freestream turbulence level was determined by matching to the reference case of Zaki et al. [127]. The turbulence intensity along a mid-passage line is shown in Figure 5.2 along with the data of Zaki et al. [127]. Close to the inlet, the turbulence intensity does not follow the rapid decay as shown by the reference curves. This is due to our application of synthetic freestream turbulence which enters through the sponge zone.

Nonetheless, within the passage there is a close match between the current simulations and the reference cases for all mesh sizes. In addition, Figure 5.3 shows pressure loading coefficient C_p comparison. There is a good match for all the cases, but there is some sensitivity on the suction side around the point of separation and re-attachment. This sensitivity is explored later in the chapter.

In all the simulations performed here the 4^{th} order DRP scheme by Tam&Webb in combination with a standard 8^{th} order filter was used. In Chapter 4 it was established

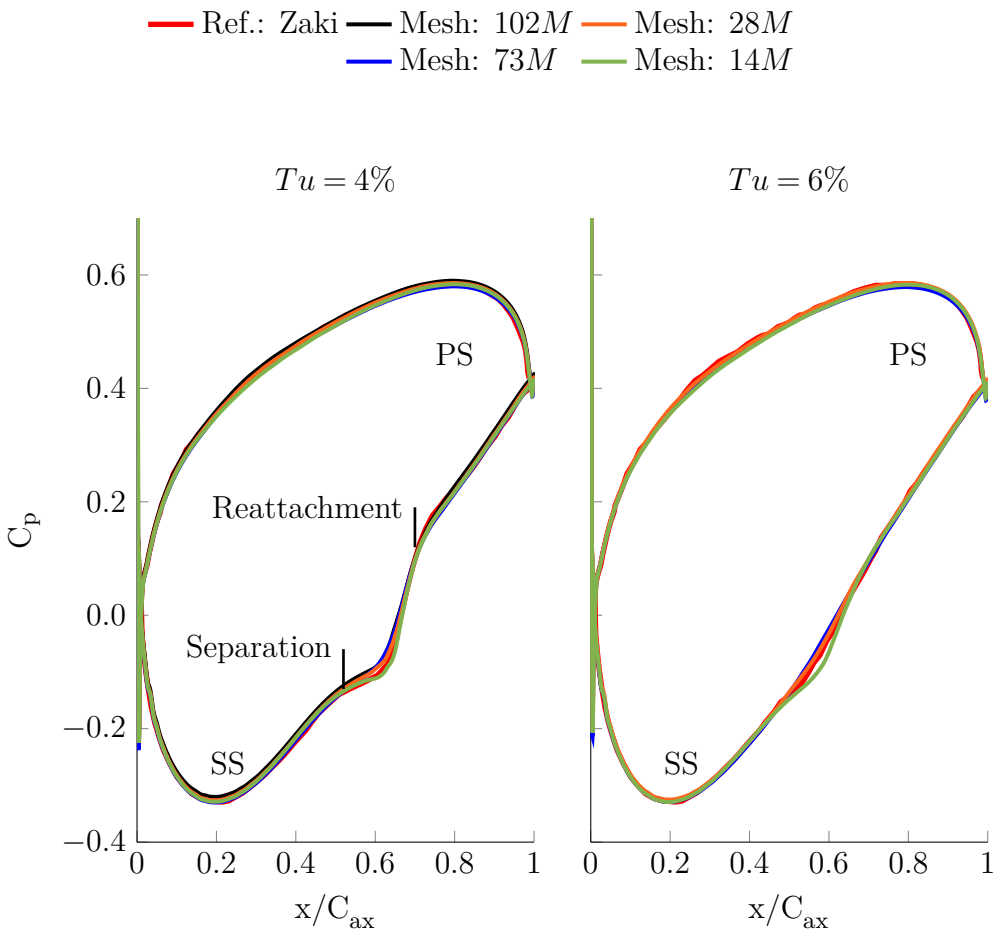

Figure 5.3: Comparison of predicted pressure loading coefficient for three mesh sizes and and reference solution, [127]: top $Tu = 4\%$; bottom $Tu = 6\%$

that cell sizes of at most $\Delta = 4\eta_{Kol}$ are needed to ensure correct entropy generation rate prediction for this scheme.

In order to characterize the mesh sizes used in this case-study, the Kolmogorov length-scale was computed from the local time-averaged entropy generation rate. An example of this is presented in Figure 5.4 which shows a region of high turbulence dissipation in the suction side boundary layer.

Table 5.2 gives a summary of the maximum cell sizes, in terms of the local Kolmogorov length-scale, for the meshes used in this study. The table shows that the criterion $\Delta \leq 4\eta_{Kol}$, is reached for mesh sizes of $73M$ and $102M$ points.

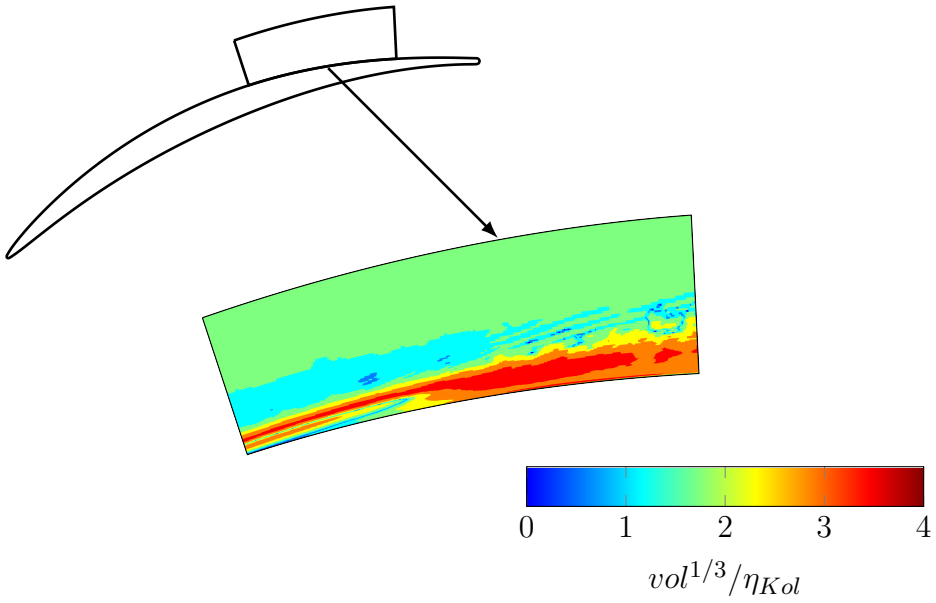

Figure 5.4: Comparison of cell size with Kolmogorov lengthscale at peak entropy generation rate region for $102M$ mesh.

5.2 Loss audit

The sensitivity of loss with mesh size is shown in Figure 5.5. For $Tu = 4\%$, the loss reaches mesh convergence for mesh sizes of $73M$ and above; the difference in loss between the $73M$ and $102M$ meshes is within 0.5%. For $Tu = 6\%$, the computed loss is more sensitive to mesh resolution, but the loss starts to level off as the mesh size reaches $73M$.

In order to determine the mechanisms driving mesh sensitivity a breakdown of loss for various parts of the flow was performed, Figure 5.6. The loss contributions were computed by integrating the entropy generation rate within the suction and pressure side boundary layers, and the freestream region (see Equation). The freestream region was defined as the region of the flow outside of the blade boundary layers and therefore included the wake.

Figure 5.6 shows that an increase in turbulence level from 4% to 6% causes a doubling in the contribution of freestream loss from around 15% to 30% of the total loss. At the same time contribution from the wake region remained at a similar level of $12-14\%$ of the total loss for both turbulence levels.

As expected, the suction side is the main contributor to the total predicted loss. Interestingly, for $Tu = 4\%$ this contribution to loss does not appear to be greatly

Table 5.2: Maximum cell size to Kolmogorov length-scale ratio Δ/η_{Kol} for suction and pressure side

Mesh points	Tu= 4%		Tu= 6%	
	$\left(\frac{\Delta}{\eta_{Kol}}\right)_{ss}$	$\left(\frac{\Delta}{\eta_{Kol}}\right)_{ps}$	$\left(\frac{\Delta}{\eta_{Kol}}\right)_{ss}$	$\left(\frac{\Delta}{\eta_{Kol}}\right)_{ps}$
14M	6.3	6.0	5.8	6.0
28M	5.0	4.8	4.5	4.7
73M	3.5	3.4	3.3	3.4
102M	3.0	3.2	-	-

affected by mesh resolution; the suction-surface loss increases by less than 3% as the mesh size is increased from $14M$ to $102M$ points. For $Tu = 6\%$ the suction surface loss is more sensitive, changing by around 7% as the mesh size is increased from $14M$ to $73M$ points.
On the other hand, the pressure side shows quite a significant sensitivity to the mesh resolution for both Tu levels; the pressure-surface loss increases by around 20% between $14M$ and $73M$ meshes. While the pressure surface represents a quarter of the total predicted loss, it is the biggest driver behind the sensitivity in loss with mesh resolution.

For this case-study, We find that mesh resolution affects loss mechanisms in three inter-linked ways, namely: transition; dissipation coefficient; and flow structure. These are discussed in turn next.

5.3 The effect of mesh resolution on transition

To understand what drives suction and pressure surface loss sensitivities the effect of mesh resolution on transition is first investigated.
Figure 5.7 shows skin friction coefficient for all considered cases. For $Tu = 4\%$, the figure shows that the suction surface undergoes a separated-flow transition. The separation bubble on the suction side shortens as mesh resolution increases; increasing the mesh size from $14M$ to $73M$ points, leads to a reduction in bubble length of about 20%.

For $Tu = 6\%$ case a significant change is observed on the suction side. Increasing the mesh size from $14M$ to $73M$ points leads to a switch between separated flow transition to attached flow transition. This leads to the elimination of the separation bubble as the mesh resolution is increased above $14M$ points. This switch is responsible for an increased sensitivity of suction side loss. The flow on the pressure surface shows similar

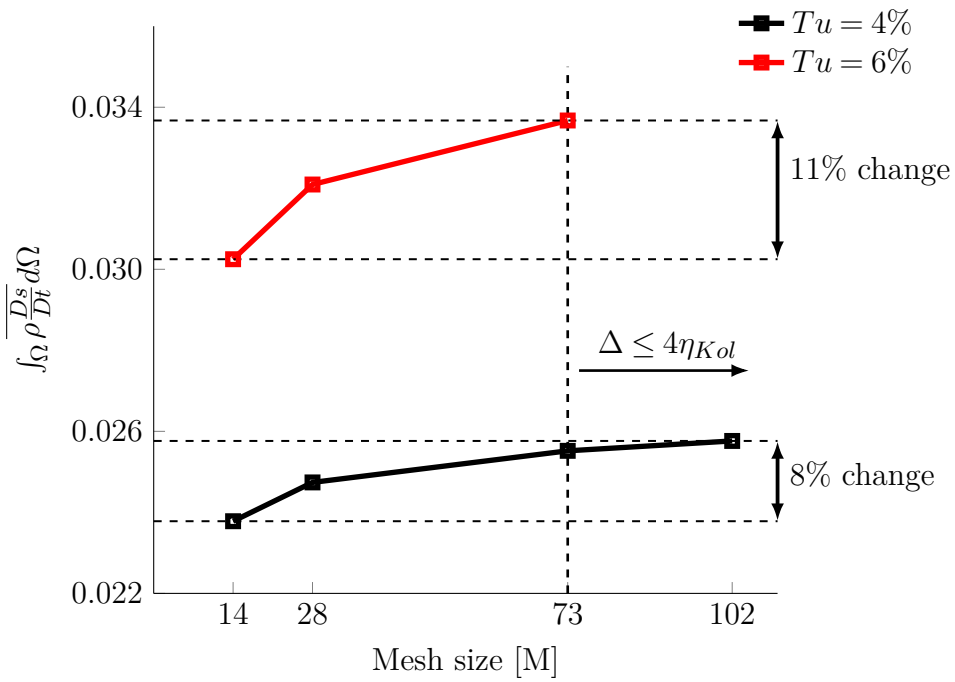

Figure 5.5: The effect of resolution on loss prediction.

behavior as in $Tu = 4\%$ case and, again, large changes over the entire pressure surface are observed.

The pressure surface skin friction shows significant sensitivity to mesh resolution for both $Tu = 4\%$ and $Tu = 6\%$. Increasing mesh size from $14M$ to $73M$ points, leads to an increase in skin friction over the entire pressure surface of around 30%, and a shift in transition upstream by around $10\%C_{ax}$.

Despite the dramatic change in the suction side transition behavior for $Tu = 6\%$ the sensitivity of loss to mesh resolution is much lower than for the pressure side as noted previously. In the next section it is explored why mesh resolution affects the pressure side more than the suction side with regard to the loss generation.

5.4 The effect of mesh resolution on dissipation coefficient

In order to quantify how the resolution changes loss within boundary layers a dissipation coefficient is computed for both the suction and pressure surfaces. A dissipation

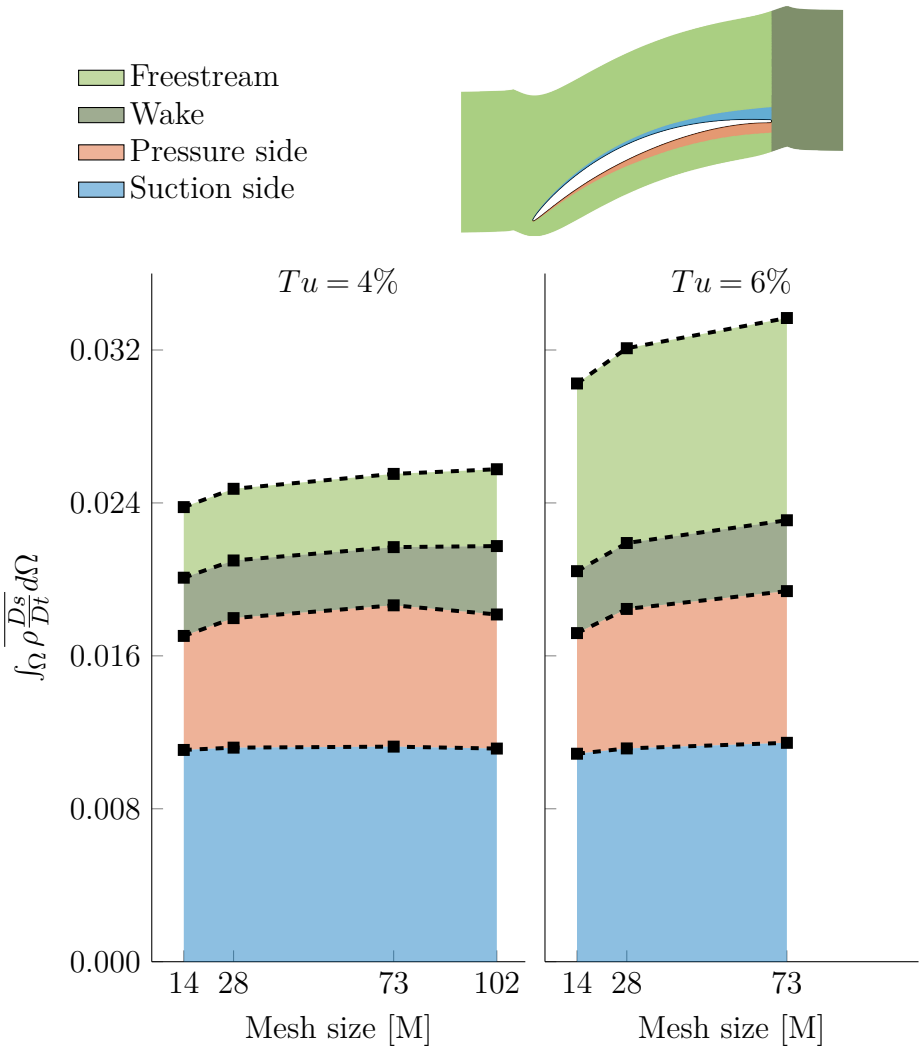

Figure 5.6: Breakdown of loss with regards to different regions of the flow.

coefficient can be defined as:

$$c_d = Pr + \frac{1}{U_e^3} \int_0^\delta \nu \left(\frac{\partial U_i}{\partial x_j} \right)^2 dy \tag{5.1}$$

The first term on the right-hand-side is the turbulence production integrated across the boundary-layer and is equal to the turbulent shear work within the boundary layer:

$$Pr = -\frac{1}{U_e^3} \int_0^\delta \overline{u_i u_j} \frac{\partial U_i}{\partial x_j} dy. \tag{5.2}$$

The second term is the dissipation due to the time-mean strain field.

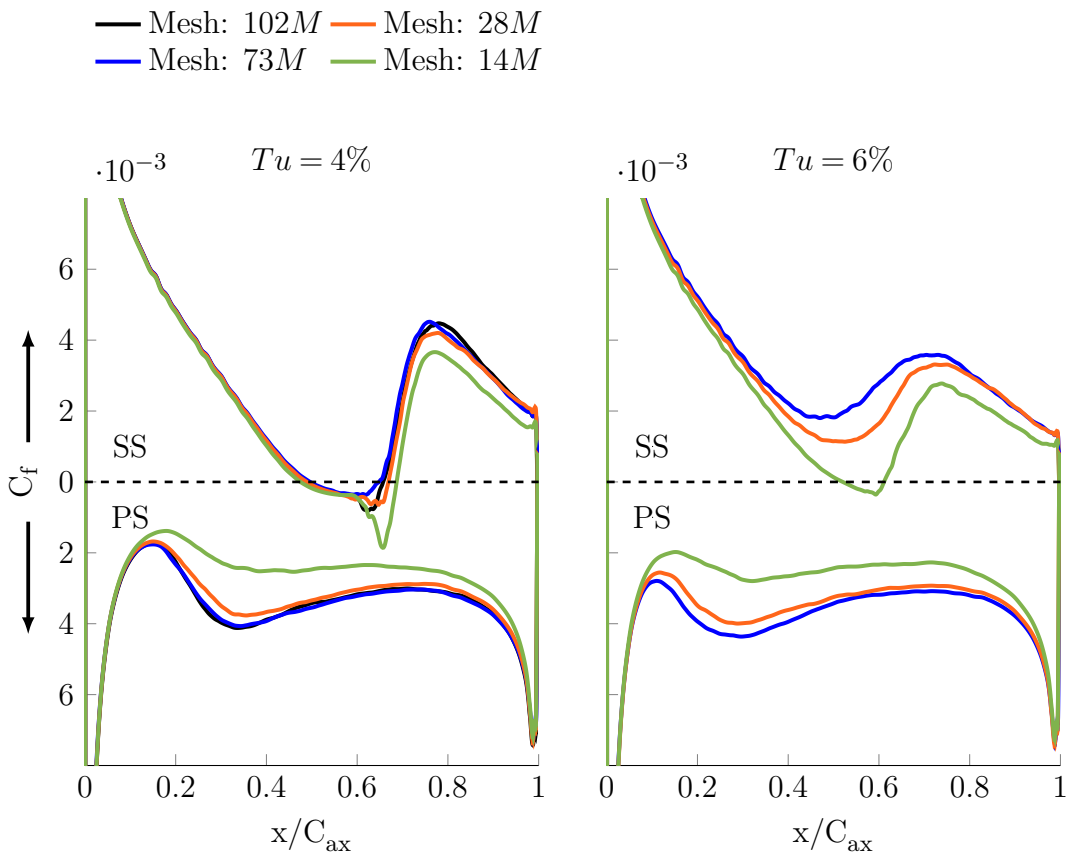

Figure 5.7: The effect of resolution on skin friction for $Tu_{in} = 4\%$ (left) and $Tu_{in} = 6\%$ (right).

Figure 5.8 shows the variation of c_d and Pr over the suction surface. The figure shows that the predicted c_d in both the laminar and turbulent regions of the flow is sensitive to mesh resolution; upstream of transition the values of c_d are around 10% higher for the $73M$ mesh as compared to the $14M$ mesh.

The difference seen in c_d can be largely explained by the changes in turbulence production. The lack of resolution leads to a delay in turbulence production, and a subsequent increase in peak production. These effects are related to the process of transition and non-equilibrium turbulence downstream of transition.

Figure 5.9 shows the variation of c_d and Pr on the pressure surface. In this case the $14M$ mesh under-predicts c_d by around $20-30\%$ over the majority of the pressure surface. Again, this difference in c_d is largely explained by differences in turbulence production. For the $14M$ mesh turbulence production is consistently lower over the entire pressure side.

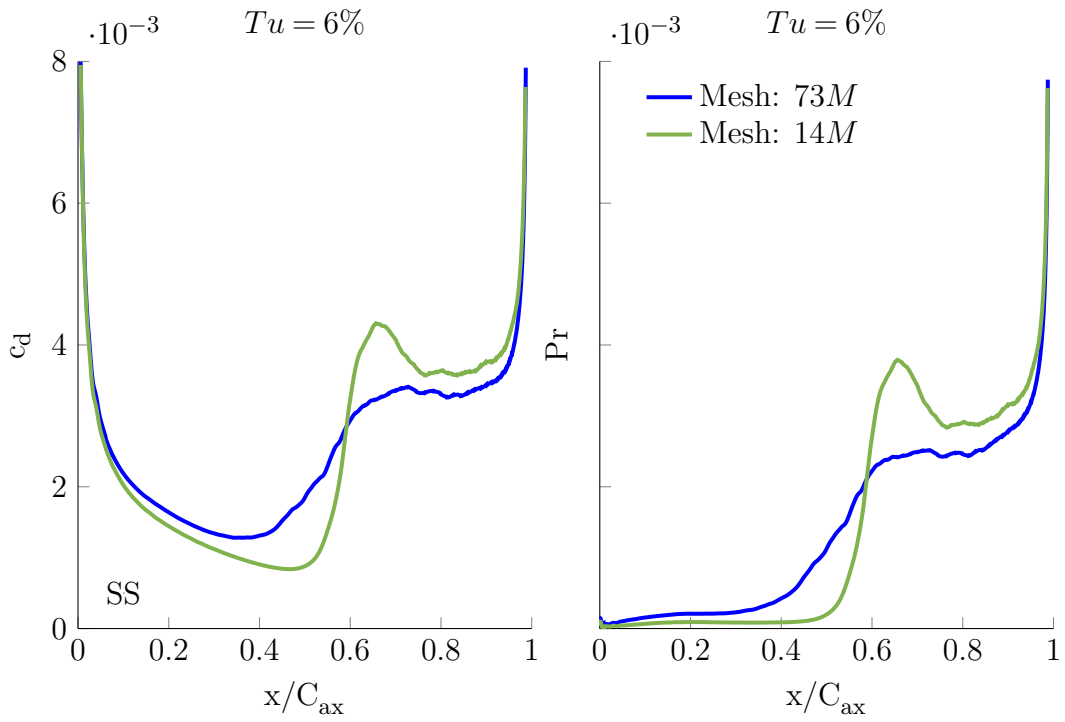

Figure 5.8: The effect of resolution on dissipation coefficient (left) and turbulence production (right) in the boundary layer on the suction side for $Tu = 6\%$.

The results show that the sensitivity of the flow to mesh resolution is strongly related to capturing the correct turbulence production. It is interesting to note that the effect of resolution on the suction side tends to be self-correcting i.e. a delay in production tends to lead to a subsequent increase later due to a more pronounced peak in turbulence production.

This behavior does not occur on the pressure side. This is because transition occurs much closer to the leading-edge and does not feature a distinct turbulence production peak as seen on the suction side. As a consequence, the failure to capture the initial boundary development at the leading-edge of pressure side affects the accuracy over the entire boundary layer. This is the cause for the high sensitivity of the pressure side loss to mesh resolution.
The results show that accurate loss prediction requires accurate turbulence production prediction. However, accurate turbulence production prediction is dependent on the process of transition and initial boundary layer development. Underlying this is the impact of mesh resolution on flow structure. In the next section the effect of mesh resolution on flow structure on both suction and pressure side is investigated.

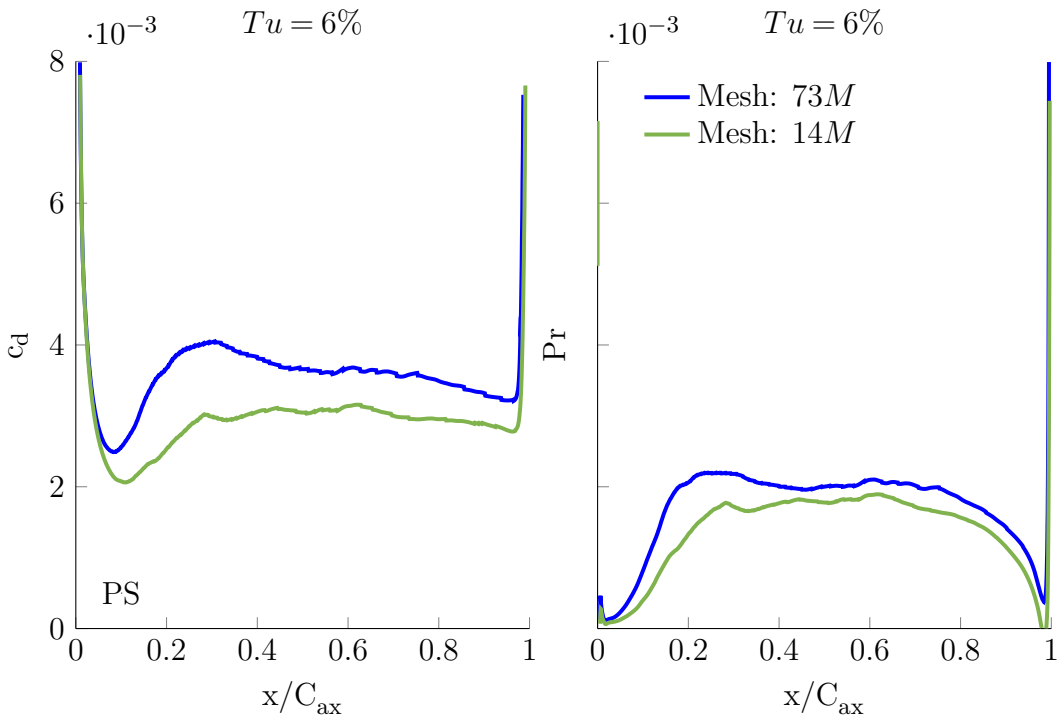

Figure 5.9: The effect of resolution on dissipation coefficient (left) and production (right) in the boundary layer on the turbulence pressure side for $Tu = 6\%$.

5.5 The effect of mesh resolution on flow structure

This section addresses the effect of mesh resolution on flow structure. In order to illustrate the structures leading to transition, Figure 5.10 shows iso-surfaces of instantaneous turbulence production on the suction side, computed using the instantaneous velocity fluctuations and mean strain rate:

$$\Pi(t) = -u_i' u_j' \frac{\partial U_j}{\partial x_i}. \tag{5.3}$$

These structures signify the extraction of energy from the base flow and are colored by the streamwise velocity fluctuation, u'. Also shown in this figure are iso-surfaces of Q-criterion to identify vortical structures within the flow and the wall shear stress. The figure shows that very little fine-scale structure is present upstream of transition for the $14M$ mesh. Instead, flow separation leads to the development of two-dimensional instabilities proceeded by a breakdown to turbulence. As mesh resolution is increased up to $73M$ points, we begin to see the emergence of streaky structures ahead of transition (labelled 'A') and the formation of turbulent spots (labelled 'B') occurring further downstream.

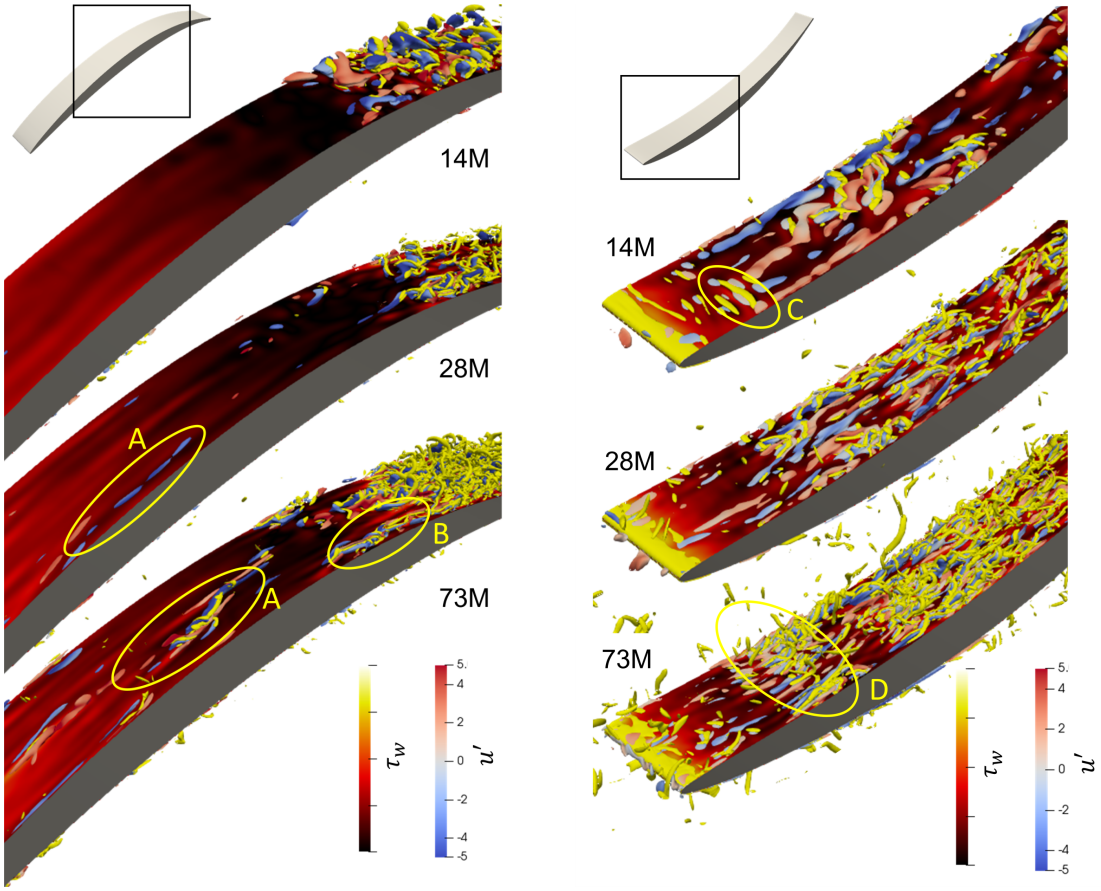

Figure 5.10: Suction surface (left) and pressre surface (right) flow structures indicated by yellow-colored iso-surfaces of Q-criterion $= 1 \times 10^8 s^{-2}$, iso-surface of instantaneous turbulence production $\Pi(t) = 5 \times 10^4$ colored by streamwise velocity fluctuation u' and surface shear stress for the $Tu = 6\%$ case.

The results suggest that these streaky structures are responsible for the growth of instabilities leading to turbulent transition. Capturing the development of streaky structures within the boundary layer ahead of transition is likely to be crucial to accurately predict the correct breakdown to turbulence and subsequent turbulence production.

These streaky structures originate near the leading edge. Figure 5.11 shows how the mesh resolution affects the size and frequency of streaky structures near the leading edge of the suction side. We notice that streaks reduce in frequency and length, but their spanwise size increases as mesh resolution is reduced. When under-resolved, as in the $14M$ point mesh, these structures tend to dissipate before they form turbulent spots. This explains the switch in transition mechanism from separated flow, to attached-flow transition seen for the $Tu = 6\%$ case, when the mesh size is increased from $14M$ to

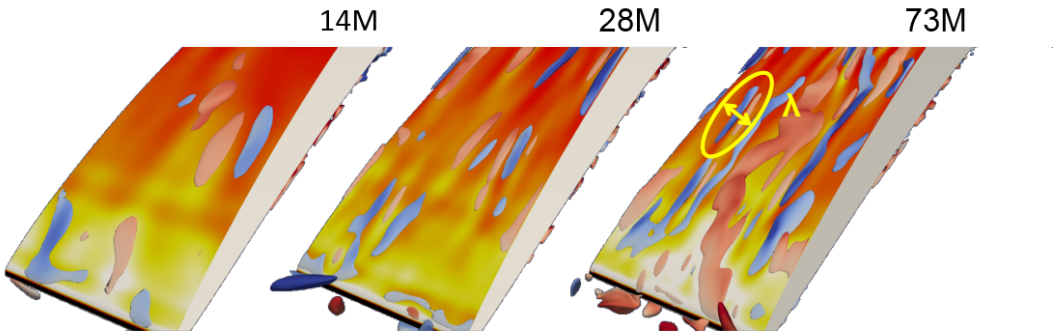

Figure 5.11: The effect of resolution on leading edge streaks.

$73M$ points.
The streak spanwise wavelength in the resolved case ($74M$ point mesh) is found to be equal to $\lambda \approx 0.015 C_{ax}$, which is around six times the local displacement thickness of the boundary layer, $\lambda \approx 6\delta^*$. This is in agreement with experiments by Matsubara and Alfredsson [57] and reinforces findings by Zaki et al. [127] that these structures are Klebanoff streaks associated with bypass transition. Leading edge streaks with similar spanwise wavelengths are also observed on the pressure surface (see Figure 5.10).

The emergence of the streaky structures near the leading edge requires capturing of the initial disturbance and its growth. Andersson et al. [3] give the spanwise wavelength of an optimal disturbance for triggering bypass transition as:

$$\lambda_{opt} = \frac{\nu}{0.45 U_{ref}} \sqrt{Re} \tag{5.4}$$

Using this expression, we find that the optimum disturbance spanwise wavelength is equal to $\lambda \approx 0.006 C_{ax}$. To correctly resolve the growth of the disturbance leading to a streaky structure, we need enough resolution to capture dispersive properties of the optimal disturbance wavelength.
The dispersion properties of the Tam & Webb scheme used in this study require at least 4.5 points per wavelength, [99]. Therefore, in order to correctly capture the leading-edge instability mechanism, in this case, we require $\Delta_z \leq 0.0013 C_{ax}$. As Table 1 indicates this is achieved for the $73M$ mesh which has 96 spanwise points for a spanwise extent of $0.1 C_{ax}$ ($\Delta_z = 0.001 C_{ax}$).
Figure 5.12 shows the summary of instability mechanisms on a compressor blade. Both, vortical and turbulence producing structures are shown. On the suction side turbulence producing structures related to the streaky structures originate from the leading edge and seem to emerge from the interaction of the leading-edge and freestream

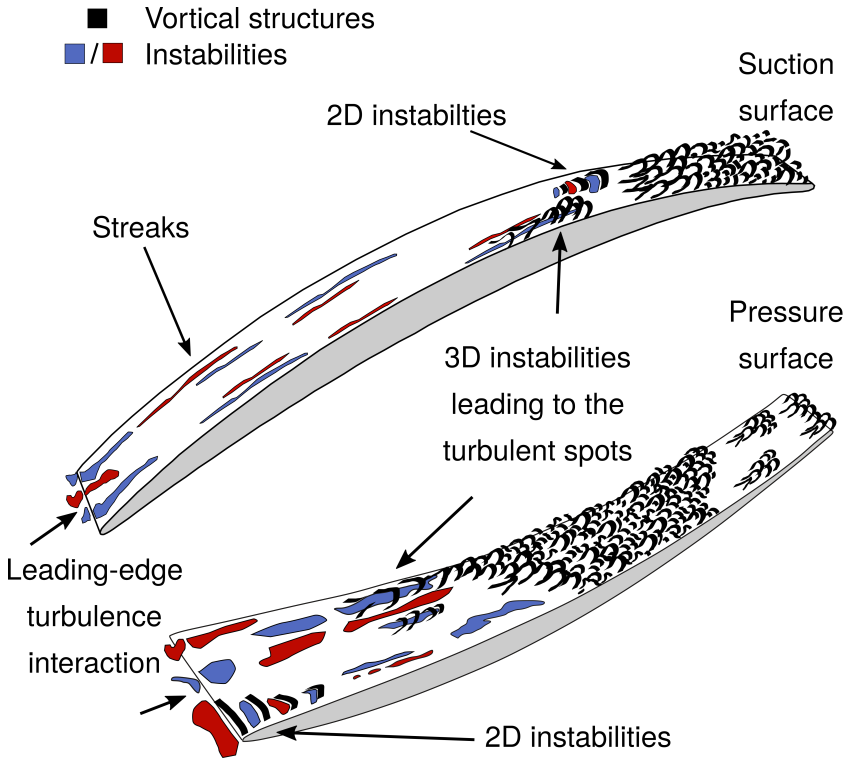

Figure 5.12: The importance of the leading edge and laminar region on accurate prediction of loss mechanisms.

turbulence. Higher freestream turbulence intensity leads to stronger streaky structures. When strong enough, these structures lead to three-dimensional instabilities that create turbulent spots. Turbulent spots prevent a separation bubble and suppress the development of two-dimensional instabilities that would otherwise emerge. On the pressure side turbulence producing structures are more abundant, but, similarly, seem to emerge from the leading-edge. Both two- and three-dimensional instabilities are present, but latter become more frequent and dominant as freestream turbulence intensity increases. Despite the differences in transition mechanisms, turbulence producing structures are always present and often act as a precursor to turbulence breakdown.

5.6 Conclusions

In this chapter the effect of resolution on flow physics was explored. This was done by employing a well established NACA65 compressor cascade. This cascade was simulated at two different freestream turbulence levels and at varying degree of resolution.

The results showed that loss, defined as entropy generation, depends predominantly on the instability mechanisms and the subsequent turbulence production. On both suction and pressure surfaces the instabilities had a streaky structure resemblance and were observed upstream of transition, Figure 5.12. Their origin was tracked to the interaction between turbulence and the leading edge of the blade which resulted in the injection of instabilities into the boundary layer.
Reducing mesh resolution was found to significantly reduce the presence of the streaky structures and instead transition tended to occur through the generation of two-dimensional instabilities which then broke down to turbulence. As a consequence of this change, turbulence production was modified both upstream and downstream of transition. On suction side this effect had a large impact on turbulence production in aft part of the blade. On pressure side, this effect spanned the entire boundary layer. To ensure correct bypass transition mechanism prediction, spanwise optimum disturbance wavelength estimate was given 5.4 and resolution recommendations based on dispersive properties of the Tam&Webb were obtained.
Throughout the study it was found that the pressure surface exhibited far greater sensitivity to mesh resolution for both low and high turbulence levels, even despite its much smaller share of loss generation. This was because transition occurred close to the leading edge and inaccuracies in the prediction of transition affected the boundary layer development over the whole pressure surface. This meant that as the mesh resolution was increased from $14M$ to $102M$ points the pressure surface loss changed by around 15%.

Chapter 6

Unsteady Energy Transfers in Compressors

Much is unknown about the multi-stage environment within the compressor. Such flows are difficult to study experimentally and are prohibitively expensive to simulate with scale resolving methods. To overcome this problem a wake recycling method is used in which wake unsteadiness from a single blade passage is recycled back into the inlet of the computational domain. This method was shown to successfully replicate a repeating-passage flow field, albeit for the mid-span section of a compressor stator (Chapter 3). The advantage of this method is that it does not rely on a-priori knowledge of the turbulence. As a result a type of repeating-passage simulation is obtained such as observed by an embedded blade-row.
Such repeating-passage simulation is employed in this chapter to explore unsteady energy transfers within the compressor passage. With the use of triply decomposed kinetic energy budgets, it is determined how energy is transferred between mean, periodic and turbulent flowfields. For the purpose of this analysis NACA65 compressor cascade is used with the running conditions (Re and Ma) identical to the ones used in the previous Chapter.

6.1 Computational setup

For the purpose of this Chapter, the repeating passage model introduced in Chapter 3 is used with NACA65 blade profile. A typical mesh and multi-block structure that was used for this study are presented in the Figure 7.2. For clarity, the mesh is shown here using every 8^{th} grid line. The mesh was generated in the identical manner as described in the Chapter 5. The NACA65 mesh had $130M$ points with $1,143k$ nodes

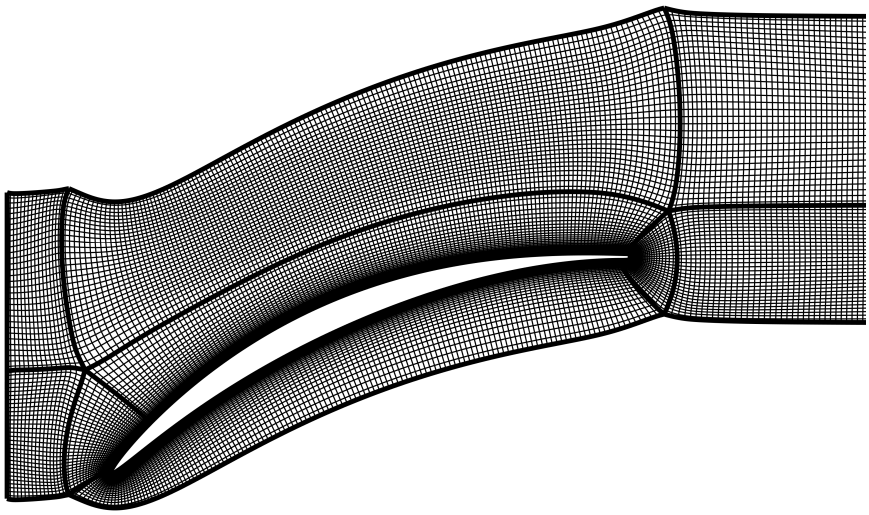

Figure 6.1: Mesh used for this study showing every 8^{th} grid line.

Table 6.1: Maximum near-wall viscous units

Mesh size	$Re_{C_{ax}}$	Δ_n^+	Δ_t^+	Δ_z^+
130M	138.5k	0.6	4.8	6.0

in the blade-to-blade plane and 112 nodes in the spanwise direction and the spanwise extent was 10% of the axial chord. There were three axial gaps that were studied: $0.30C_{ax}$, $0.40C_{ax}$ and $0.50C_{ax}$. In all simulations periodic boundary conditions were enforced in both spanwise and pitchwise directions.

Maximum viscous wall units are shown in Table 6.1. The NACA65 simulation resolution compares favorably with previously established benchmark DNS of Zaki et al. [127] as over twice as many mesh points per spanwise extent are used here to ensure good freestream turbulence resolution.

An example of an instantaneous flowfield for NACA65 profile at $0.40C_{ax}$ gap obtained using the wake recycling routine can be seen in Figure 6.2 for which the spanwise vorticity contours were plotted. Upstream rotor wakes are easily identifiable and remain distinct for the whole passage. Between upstream rotor segments there are disturbances in the freestream due to the accumulation of turbulence from the upstream passages.

The results used in this chapter comprise of time- and phase-averaged data spanning

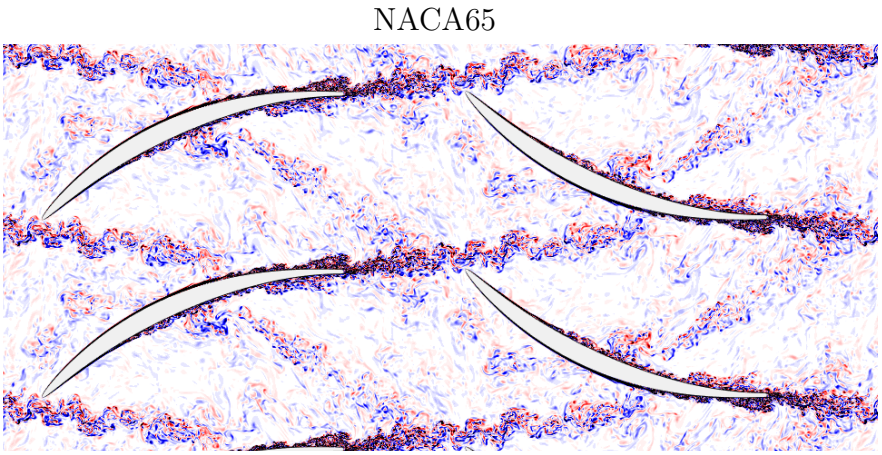

Figure 6.2: Instantaneous spanwise vorticity flowfield of a stator row of a repeating-passage simulation for the NACA65 blade profile.

at least 15 wake periods. The averaging procedure also assumed that the flow can be spanwise-averaged. For the purpose of phase-averaging, the wake period was split into 20 phases.

6.2 Loss summary

To estimate loss as well as its resolved and unresolved components, similar to previous analyses, entropy budgets are used. For the cases considered here, integrated heat transfer terms are negligible and thus:

$$\int_\Omega \rho T \frac{Ds}{Dt} d\Omega = \int_\Omega (\phi + \epsilon_N)\, d\Omega \tag{6.1}$$

As before, three metrics are defined, these represent the total entropy generation within the volume ϵ_S, the entropy generation rate due to resolved dissipation, ϵ_ϕ and the effect of artificial dissipation due to filtering, ϵ_N:

$$\begin{aligned} \epsilon_S &= \int_\Omega T\rho \frac{Ds}{Dt} d\Omega \\ \epsilon_\phi &= \int_\Omega \phi d\Omega = \int_\Omega \tau_{ij} \frac{\partial u_i}{\partial x_j} d\Omega \\ \epsilon_N &= \epsilon_S - \epsilon_\phi \end{aligned} \tag{6.2}$$

Table 6.2: Comparison between resolved and unresolved dissipation

	$g_{ax} = 0.30C_{ax}$	$g_{ax} = 0.40C_{ax}$	$g_{ax} = 0.50C_{ax}$
ϵ_S	7.002	6.694	6.764
ϵ_ϕ	6.327	6.080	6.103
ϵ_N	0.675	0.610	0.661

Table 6.2 gives a summary of those metrics. It can be noticed that the amount of unresolved dissipation is of similar magnitude for all three cases and accounts for around 10% of the overall entropy generation. The table also shows that as gap is reduced, loss rises. This is driven by a change in turbulence production as shown later.

6.3 Triple decomposition of kinetic energy

Considerable insight can be drawn from the analysis of kinetic energy budgets. This is commonly done by decomposing the flow into mean and fluctuating components using classic Reynolds decomposition (done for reference in Appendix A). However, the flow considered here is subject to periodic wakes and Reynolds decomposition treats periodic oscillations and turbulent fluctuations together. To distinguish turbulence fluctuations from organized (oscillating) motion of the wake, Hussain and Reynolds proposed a triple decomposition which splits the total instantaneous velocity field into mean, periodic (oscillating) and turbulent (fluctuating) components:

$$f = \bar{f} + f^* + f' \tag{6.3}$$

Compared to original equations by Hussain and Reynolds, decomposition here uses Favre averaged quantities:

$$\bar{f} \equiv \frac{\overline{\rho f}}{\bar{\rho}} \tag{6.4}$$

The flow here is also considered compressible, however, as the Mach number for the NACA65 testcase is low, density fluctuations were assumed to be negligible, i.e. $\rho' \approx 0$. In addition, $\langle f \rangle$ will represent the phase-averaged quantity of f.

Triple decomposition of kinetic energy equations allows for a more detailed study of energy transfers compared to double decomposition. As a consequence, the role of periodic wakes can be isolated and its effect on turbulent field quantified. The resulting set of kinetic energy equations for mean (m), oscillating periodic (o) and fluctuating

turbulent (f) fields is as follows:

$$\underbrace{\frac{\bar{D}}{Dt}\left(\bar{\rho}\frac{1}{2}\bar{u_i}\bar{u_i}\right)}_{c_m} = \underbrace{-\left(-\overline{\rho u_i' u_j'}\frac{\partial \bar{u_i}}{\partial x_j}\right) - \left(-\overline{\rho u_i^* u_j^*}\frac{\partial \bar{u_i}}{\partial x_j}\right)}_{t_{mf}+t_{mo}} \underbrace{- \frac{\partial}{\partial x_j}\left[\bar{u_i}\left(\overline{\rho u_i' u_j'}\right)\right] - \frac{\partial}{\partial x_j}\left[\bar{u_i}\left(\overline{\rho u_i^* u_j^*}\right)\right]}_{d_{1,m}+d_{2,m}}$$
$$+ \underbrace{\frac{\partial \bar{\tau_{ij}}\bar{u_i}}{\partial x_j}}_{v.d._m} \underbrace{- \bar{\tau_{ij}}\frac{\partial \bar{u_i}}{\partial x_j}}_{\phi_m} \underbrace{- \bar{u_i}\frac{\partial \bar{p}}{\partial x_i}}_{p.w._m} \tag{6.5a}$$

$$\underbrace{\frac{\bar{D}}{Dt}\left(\bar{\rho}\frac{1}{2}\overline{u_i^* u_i^*}\right)}_{c_o} = \underbrace{+\left(-\overline{\rho u_i^* u_j^*}\frac{\partial \bar{u_i}}{\partial x_j}\right) - \left(-\overline{\left\langle \rho u_i' u_j' \right\rangle \frac{\partial u_i^*}{\partial x_j}}\right)}_{t_{mo}+t_{of}} \underbrace{- \overline{\frac{\partial}{\partial x_j}\left[\rho u_j^*\left(\frac{1}{2}u_i^* u_i^*\right)\right]} - \frac{\partial}{\partial x_j}\left[\overline{\rho u_i^* \left\langle u_i' u_j' \right\rangle}\right]}_{d_{1,o}+d_{2,o}}$$
$$+ \underbrace{\frac{\partial \overline{\tau_{ij}^* u_i^*}}{\partial x_j}}_{v.d._o} \underbrace{- \overline{\tau_{ij}^* \frac{\partial u_i^*}{\partial x_j}}}_{\phi_o} \underbrace{- \bar{u_i^*}\frac{\partial \bar{p}}{\partial x_i}}_{p.w._o} \underbrace{- \frac{\partial \overline{p^* u_i^*}}{\partial x_i}}_{p.d._o} \underbrace{+ \overline{p^* \frac{\partial u_i^*}{\partial x_i}}}_{p.l._o} \tag{6.5b}$$

$$\underbrace{\frac{\bar{D}}{Dt}\left(\bar{\rho}\frac{1}{2}\overline{u_i' u_i'}\right)}_{c_f} = \underbrace{+\left(-\overline{\rho u_i' u_j'}\frac{\partial \bar{u_i}}{\partial x_j}\right) + \left(-\overline{\left\langle \rho u_i' u_j' \right\rangle \frac{\partial u_i^*}{\partial x_j}}\right)}_{t_{mf}+t_{of}} \underbrace{- \frac{\partial}{\partial x_j}\left[\overline{\rho u_j'\left(\frac{1}{2}u_i' u_i'\right)}\right] - \overline{\rho u_j^* \frac{\partial}{\partial x_j}\left\langle \frac{1}{2}u_i' u_i' \right\rangle}}_{d_{1,f}+d2,f}$$
$$+ \underbrace{\frac{\partial \overline{\tau_{ij}' u_i'}}{\partial x_j}}_{v.d._f} \underbrace{- \overline{\tau_{ij}' \frac{\partial u_i'}{\partial x_j}}}_{\phi_f} \underbrace{- \bar{u_i'}\frac{\partial \bar{p}}{\partial x_i}}_{p.w._f} \underbrace{- \frac{\partial \overline{p' u_i'}}{\partial x_i}}_{p.d._f} \underbrace{+ \overline{p' \frac{\partial u_i'}{\partial x_i}}}_{p.l._f} \tag{6.5c}$$

where

$$\frac{\bar{D}}{Dt} \equiv \frac{\partial}{\partial t} + \bar{u_j}\frac{\partial}{\partial x_j} \tag{6.6}$$

and

c - convection of kinetic energy

t - energy transfer between mean, oscillating and fluctuating flowfield

d - diffusion due to unsteadiness

$v.d.$ - viscous diffusion

ϕ - viscous dissipation

$p.w.$ - pressure work

$p.d.$ - pressure diffusion

p.l. - pressure dilation

Hussain-Reynolds decomposition is similar to Reynolds decomposition, except the unsteady field is split into oscillating (periodic) and fluctuating (turbulent) components. As a result, the equations now feature additional terms that govern energy transfers, t, between mean and oscillating as well as oscillating and fluctuating flowfields. There are also additional diffusion terms related to the turbulent transport, d. Reynolds decomposition can be fully recovered by summing up equations 6.5b and 6.5c.
The energy transfer terms, t, play a crucial role as they link kinetic energy equations together, each term showing twice with an opposite sign and acting as an energy source/sink for the given equation. These terms govern:
Mean to turbulent (fluctuating) energy transfer:

$$t_{mf} = -\overline{\rho u_i' u_j'} \frac{\partial \bar{u}_i}{\partial x_j} \tag{6.7}$$

Mean to periodic (oscillatory) energy transfer:

$$t_{mo} = -\overline{\rho u_i^* u_j^*} \frac{\partial \bar{u}_i}{\partial x_j} \tag{6.8}$$

Periodic (oscillating) to turbulent (fluctuating) energy transfer:

$$t_{of} = -\overline{\left\langle \rho u_i' u_j' \right\rangle \frac{\partial u_i^*}{\partial x_j}} \tag{6.9}$$

Each of these transfer terms is a product of a gradient of mean or oscillatory motion and a stress term of periodic (oscillating) and turbulent (fluctuating) motion. The sum of t_{mf} and t_{of} terms is the turbulence production discussed in more detail in Chapter 7.
To study these transfers all the quantities were integrated in the volume, Ω, from the inlet of the domain to the sampling plane (see 3.4 for reference) to compute a total energy budget for the flowfield. Turbulent pressure dilation term as well as periodic and turbulent pressure work terms were ignored due to their negligible impact. The integrated quantities are capitalized, for instance the integrated dissipation is:

$$\Phi = \int_{\Omega} \phi d\Omega \tag{6.10}$$

Tables 6.4, 6.5, 6.6 show that the kinetic energy budget is satisfied for all three equations for the repeating passage simulations. For the turbulent kinetic energy budget,

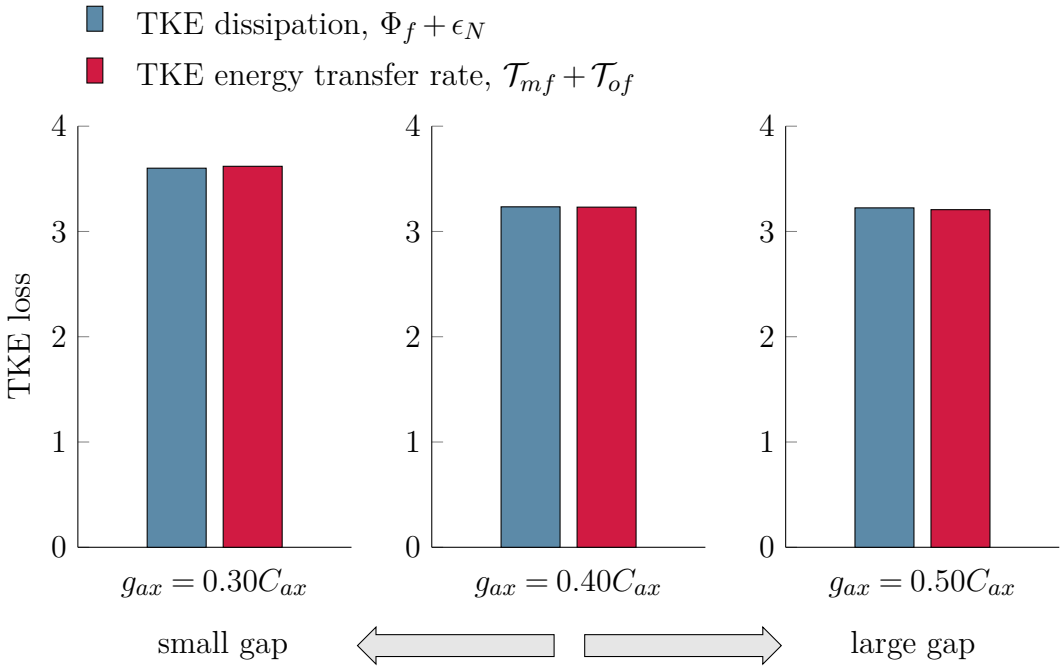

Figure 6.3: The comparison of integrated turbulent dissipation ($\Phi_f + \epsilon_N$) and energy transfer terms ($\mathcal{T}_{mf} + \mathcal{T}_{of}$) for three considered gaps.

artificial dissipation due to filtering, ϵ_N was added to the turbulent resolved dissipation, Φ_f to balance budget.

Now that the turbulence was decomposed into periodic and turbulent components, it is possible to isolate the energy transfer to the turbulent (fluctuating) component only. It is that component of the flow that is expected to extract useful energy from the total flowfield and dissipate it, thus generating loss. Figure 6.3 demonstrates that turbulent dissipation (both resolved and unresolved) is balanced out by a combined action of energy transfer terms. The dissipation of energy of small-scale motion is therefore equal to the total turbulence production.

Standard Reynolds decomposition is unable to separate the action of periodic wakes from turbulent motion and so transfer rate obtained this way cannot balance turbulent dissipation. This is demonstrated in Appendix A.

6.4 Loss accounting

Recalling the Equation 6.1, the loss can be now re-written to substitute resolved and unresolved turbulent dissipation with energy transfer terms t_{mf} and t_{of}, Equation 6.11. These terms signify the amount of energy extracted and transferred to sustain the turbulent motion, i.e. the total turbulence production.

$$\begin{aligned}\int_\Omega \rho T \frac{Ds}{Dt} d\Omega &= \int_\Omega \left(\phi + \epsilon_N\right) d\Omega \\ &= \int_\Omega \left(\phi_m + \phi_o + \phi_f + \epsilon_N\right) d\Omega \\ &\approx \int_\Omega \left(\phi_m + \phi_o + t_{mf} + t_{of}\right) d\Omega\end{aligned} \tag{6.11}$$

From Table 6.2 it can be seen that as gap reduces, loss is increased. In Chapter 7 it will be shown that this rise in loss is due to the energy transfer terms above, i.e. the total turbulence production.

6.5 Energy transfer rate terms

To understand how and where energy is transferred between mean, periodic and turbulent flowfields, contributions to those terms from various flow regions were computed. The domain was split into different regions corresponding to boundary layers, freestream and wake segments. Boundary layers were identified using vorticity criterion $\omega_z < 300$, while upstream rotor wakes were separated from the background turbulence using a detector function. This detector was based on axial velocity deficit, turbulence intensity level and turbulence dissipation. The detector was set equal to 1 in regions where at least two out of three conditions were true: i.e. $u^* < 0$ and/or $\langle u_i' u_i' \rangle > \overline{u_i' u_i'}$ and/or $\langle \phi_f \rangle > \overline{\phi_f}$. An example of the performance of this splitting method is shown in Figure 6.4, which demonstrates that the method is able to correctly identify wake segments from the upstream rotor within the passage.

Table 6.3 show the breakdown of integrated transfer rates for a $g_a x = 0.40 C_{ax}$ gap case. In addition, significant positive and negative contributions were highlighted in the table. The results show that transfer rate from mean to turbulent flowfield, t_{mf} is overwhelmingly positive with majority of it happening in the boundary layers. The transfer rate between mean and periodic flowfield, t_{of}, is found to be negative. This means that the energy carried by the wakes is transferred into the mean flowfield. Around 70% of this negative transfer was confined within wake segments with an

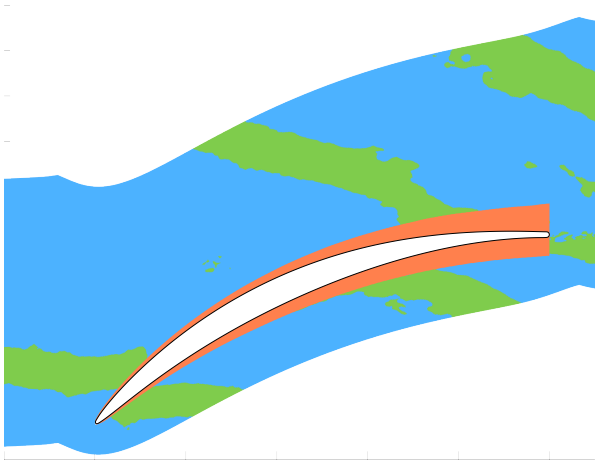

Figure 6.4: Domain split for NACA65 testcase.

additional small contribution from the freestream. The transfer rate from periodic to turbulent flowfield, t_{of}, was positive with almost the entirety of it happening, unsurprisingly, within the wake segment. These rates are further explored below where their time- and phase-averaged contributions are plotted.

Table 6.3: Breakdown of integrated transfer rates for a $g_a x = 0.40 C_{ax}$ gap case

	$t_{mf} = -\overline{\rho u_i' u_j'} \frac{\partial \bar{u}_i}{\partial x_j}$	$t_{mo} = -\overline{\rho u_i^* u_j^*} \frac{\partial \bar{u}_i}{\partial x_j}$	$t_{of} = -\overline{\left\langle \rho u_i' u_j' \right\rangle} \frac{\partial u_i^*}{\partial x_j}$
Total	**2.789**	**-0.312**	**0.442**
Suction side	1.546	0.041	-0.001
Pressure side	0.781	-0.008	-0.003
Freestream	0.278	-0.134	0.060
Wake segments	0.148	-0.211	0.387

6.5.1 Mean to turbulent energy transfer

As noted before, mean to turbulent energy transfer rate (t_{mo}) is positive and happens predominantly within the boundary layers. Figure 6.5 further confirms these findings. Time-averaged energy transfer rate revealed local negative contributions around the leading edge of the blade, but this does not affect the overall balance significantly. The phase-averaged energy transfer rate picture at one of the rotor wake phases shows that energy transfer rate happens also in the freestream where both positive and negative contributions are found. These however seem to balance resulting in an overall small

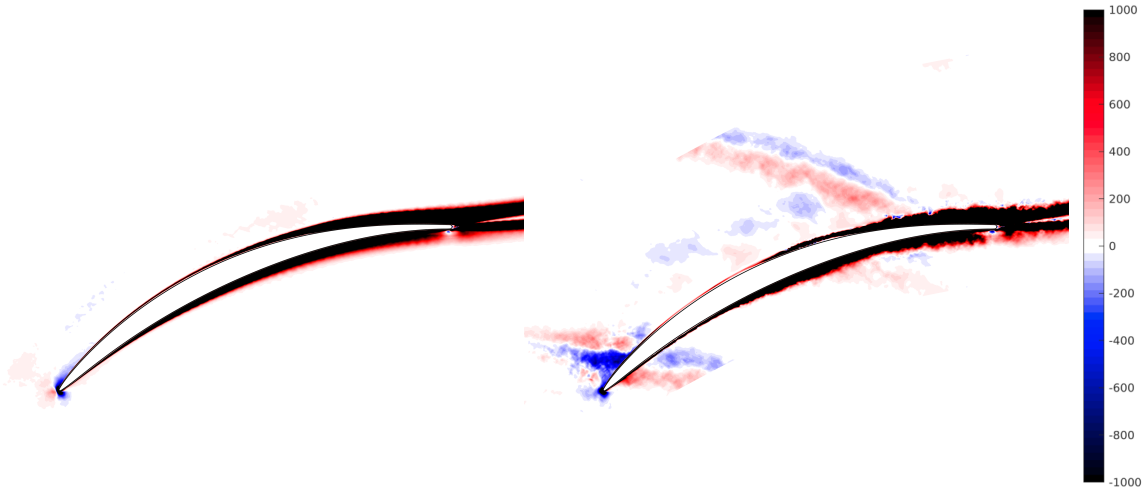

(a) Time-averaged (b) Phase-averaged

Figure 6.5: Time- and phase-averaged energy transfer rate between the mean and turbulent flowfield: $t_{mf} = -\overline{\rho u_i' u_j'} \frac{\partial \bar{u}_i}{\partial x_j}$

positive contribution from both freestream and wake segments. Local negative mean to fluctuating energy transfer values have been also reported elsewhere, e.g. in the shear layer of separating and reattaching flows [16].
This energy transfer rate is by far dominant and is responsible for the majority of energy extracted from the flowfield. It also highlights a dominant role of suction side in loss generation as it is responsible for over 50% of it.

6.5.2 Mean to periodic energy transfer

Figure 6.6 shows a complex behavior of energy transfer rate between mean and periodic flowfields (t_{mo}). In a time-averaged sense the majority of mean to periodic energy transfer is negative and happens in the freestream at the fore of the passage. This means the energy is extracted from the wakes and transferred into the mean flowfield where it could potentially contribute to useful mechanical work. Some positive energy transfer contributions are found near the leading edge and around the transition region of the suction side boundary layer.
Interestingly, phase-averaged energy transfer rate shows that wake segment starts off with a positive transfer rate. As the wake convects through the passage, this contribution changes from positive to negative. This effect seem to be related to the wake reorientation and stretching as it convects through the passage and therefore may be related to the wake recovery effect which tends to reduce mixing loss, [95, 26, 107].

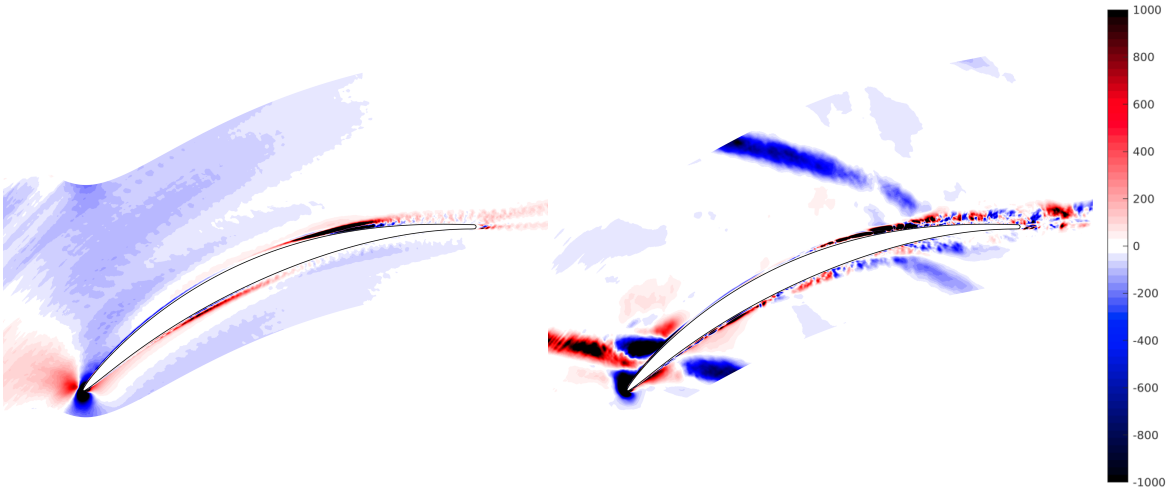

(a) Time-averaged (b) Phase-averaged

Figure 6.6: Time- and phase-averaged energy transfer rate between the mean and periodic flowfield: $t_{mo} = -\overline{\rho u_i^* u_j^*} \frac{\partial \bar{u_i}}{\partial x_j}$

However, the contribution to the overall loss generation is unknown and generally seem to be outweighed by energy transfer rate from periodic to turbulent flowfield, t_{of}. The net wake recovery effect will be evaluated in Chapter 7.

6.5.3 Periodic to turbulent energy transfer

Figure 6.7 shows time- and phase-averaged energy transfer rate between the periodic and turbulent flowfields (t_{of}). As demonstrated previously in Table 6.3 the majority of this term comes from the wake segments. The terms signifies the extraction of energy from the wakes and and is the product of a gradient of oscillatory motion and turbulent stresses. This turbulence production mechanism is further explored in Chapter 7.

6.6 Conclusions

In this chapter a new repeating passage model is used to study the multi-stage compressor flowfield. The analysis of triply decomposed kinetic energy budgets allowed for a detailed study of energy transfers within the compressor. This investigation revealed an important role total turbulence production plays in determining the loss within the compressor.

The study also showed that energy transfer between the mean and periodic flowfield is

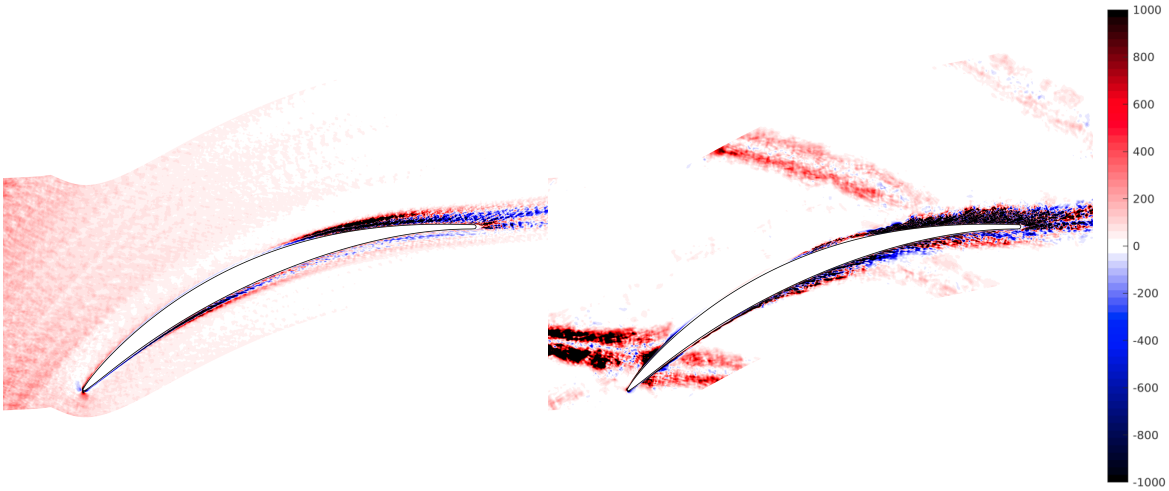

(a) Time-averaged (b) Phase-averaged

Figure 6.7: Time- and phase-averaged energy transfer rate between the periodic and turbulent flowfield: $t_{of} = -\overline{\left\langle \rho u_i' u_j' \right\rangle} \frac{\partial u_i^*}{\partial x_j}$

often negative and has potentially positive impact on compressor performance. Since this effect is related to wake re-orientation and stretching, it is likely to be linked to wake recovery effects. However, its overall role in loss reduction/generation is unclear.

The next Chapter will make use of these findings and explore the mechanisms responsible for the production of turbulence in a multi-stage compressors, how they vary with the axial gap and compare with wake recovery effects.

Table 6.4: Triple decomposition - mean kinetic energy budget

Eq. 6.5a	$C_m = -\mathcal{T}_{mf} - \mathcal{T}_{of} - D_{1,m} - D_{2,m} + V.D._{\cdot m} - \Phi_m - P.W._{\cdot m}$		
	$g_{ax} = 0.30 C_{ax}$	$g_{ax} = 0.40 C_{ax}$	$g_{ax} = 0.50 C_{ax}$
C_m	-107.716	-109.583	-109.977
$\mathcal{T}_{mf}$	2.976	2.789	2.759
$\mathcal{T}_{of}$	-0.640	-0.312	-0.180
$D_{1,m}$	-0.014	-0.081	0.001
$D_{2,m}$	-3.967	-2.468	-2.076
$V.D._{\cdot m}$	0.012	0.013	0.014
Φ_m	3.419	3.472	3.554
$P.W._{\cdot m}$	105.906	106.287	105.678
NET	0.048	-0.091	0.253

Table 6.5: Triple decomposition - oscillating kinetic energy budget

Eq. 6.5b	$C_o = +\mathcal{T}_{mo} - \mathcal{T}_{of} - D_{1,o} - D_{2,o} + V.D._{\cdot o} - \Phi_o - P.W._{\cdot o} - P.D._{\cdot o} + P.L._{\cdot o}$		
	$g_{ax} = 0.30 C_{ax}$	$g_{ax} = 0.40 C_{ax}$	$g_{ax} = 0.50 C_{ax}$
C_o	-2.088	-1.420	-1.189
$\mathcal{T}_{mo}$	-0.640	-0.312	-0.180
$\mathcal{T}_{of}$	0.643	0.442	0.448
$D_{1,o}$	0.422	0.411	0.326
$D_{2,o}$	0.134	0.104	0.080
$V.D._{\cdot o}$	0.002	0.001	0.001
Φ_o	0.084	0.073	0.057
$P.W._{\cdot o}$	-0.001	-0.002	0.000
$P.D._{\cdot o}$	0.022	-0.004	-0.022
$P.L._{\cdot o}$	0.002	0.001	0.001
NET	0.147	0.089	0.122

Table 6.6: Triple decomposition - fluctuating kinetic energy budget

Eq. 6.5c	$C_f = +\mathcal{T}_{mf} + \mathcal{T}_{of} - D_{1,f} - D_{2,f} + V.D._f - \Phi_f - P.W._f - P.D._f + P.L._f$		
	$g_{ax} = 0.30C_{ax}$	$g_{ax} = 0.40C_{ax}$	$g_{ax} = 0.50C_{ax}$
C_f	-0.018	-0.106	-0.059
$\mathcal{T}_{mf}$	2.976	2.789	2.759
$\mathcal{T}_{of}$	0.643	0.442	0.448
$D_{1,f}$	0.000	0.000	-0.001
$D_{2,f}$	0.160	0.136	0.113
$V.D._f$	0.000	0.000	0.000
$\Phi_f + \epsilon_N$	2.842 + 0.675	2.552 + 0.610	2.507 + 0.661
$P.W._f$	–	–	–
$P.D._f$	-0.056	-0.056	-0.041
$P.L._f$	–	–	–
NET	-0.096	-0.020	-0.054

Chapter 7

Multi-Stage Compressor Loss Mechanisms - The Effect of Gapping

In the previous Chapter a series of steps were made towards simulating the flow within the multi-stage compressor and understanding energy transfers within it. In this chapter, previously developed repeating passage model is used to study both the nature of turbulence and the loss generation within a multi-stage machine.
For the purpose of this analysis NACA65 blade geometry as well as custom CDA geometry are used at three different axial gaps each. The turbulence generated in the setups considered here is free of any a-priori knowledge about the inlet turbulence and originates only as a consequence of the accumulation of recycled unsteadiness. It is therefore possible to study the effect of axial gap on the freestream turbulence within multi-stage compressors. The aspect of loss generation is addressed by making use of Chapter 6 outcomes, demonstrating turbulence production mechanisms and how they change as the gap is varied.

7.1 Computational setup

For this study the midspan section of two geometries are used: the well-established NACA65 compressor blade geometry that was used in previous studies by Zaki et al. [126], Legget et al. [54] and Przytarski and Wheeler [83]; the second geometry is a controlled-diffusion profile (CDA) representative of a modern high pressure ratio compressor. This geometry was designed according to current design principles following

Table 7.1: Test-case details

Case	Re	Ma	ϕ_{flow}	ψ_{work}	F_{red}	α_{in}	F_{rotor}
NACA65	140k	0.065	1	0.79	1.71	42°	$273.3Hz$
CDA	250k	0.20	0.568	0.45	2.49	51.78°	$100.0Hz$

the method outlined in the work of To and Miller [101]. Compared to NACA65 geometry, CDA design has blade loading shifted forward with the peak suction surface Mach number located at about 20% of the chord. This helps prevent premature laminar boundary layer separation at the suction surface and allows for a continuous flow deceleration towards the trailing edge while maintaining an attached turbulent boundary layer with a low level of skin friction. CDA design also maintains almost a constant pressure side loading when compared to the NACA65 design. Details of the two geometries are shown in Table 7.1. For both geometries the flow coefficient, and thus blade speed, is set by the stage reaction ($\Lambda = 50\%$) and the inlet and exit flow angles. Figure 7.1 shows the blade profiles and loading distributions for these two geometries.

Mesh details

A typical mesh and multi-block structure that was used for this study are presented in the Figure 7.2. For clarity, the mesh is shown here using every 8^{th} grid line. The mesh was generated in the identical manner as described in the Chapter 5. The NACA65 testcase mesh was identical to the ones used in Chapter 6 and had $130M$ points with $1,143k$ nodes in the blade-to-blade plane and 112 nodes in the spanwise direction and the spanwise extent was 10% of the axial chord. The CDA testcase mesh had $170M$ points with $1,087k$ nodes in the blade-to-blade plane and 160 nodes in the spanwise direction. The spanwise extent for CDA testcase was 15% of the axial chord. In all simulation setups periodic boundary conditions were enforced in both spanwise and pitchwise directions.

Maximum viscous wall units are shown in Table 7.2. The resolution of NACA65 and CDA testcases puts the simulation in the range of wall-resolved LES. Freestream spectrum from the NACA65 testcase, shown later, indicates that the range of eddies beyond inertial subrange is captured.

An example of an instantaneous flowfield for both NACA65 and CDA profiles at $0.40C_{ax}$ gap obtained using the wake recycling routine can be seen in Figure 7.3

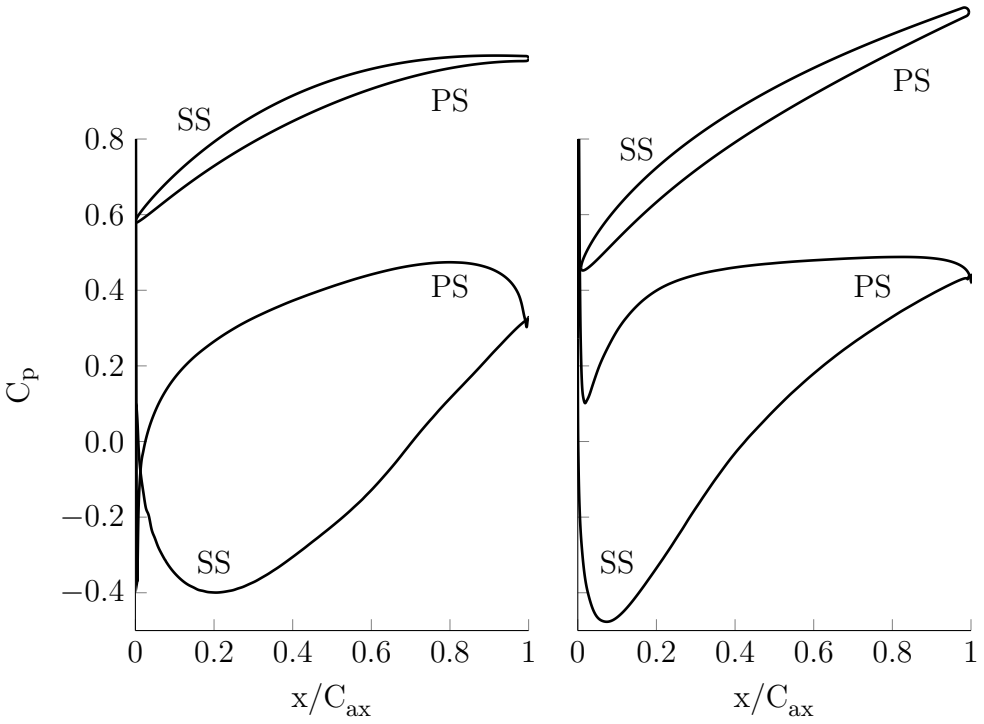

Figure 7.1: Loading distributions for the NACA65 (left) and the CDA profiles (right)

Table 7.2: Maximum near-wall viscous units

Case	$Mesh$	Δ_n^+	Δ_t^+	Δ_z^+
NACA65	130M	0.6	4.8	6.0
CDA	170M	0.9	15.5	10.0

for which the spanwise vorticity contours were plotted. Upstream rotor wakes are easily identifiable and remain distinct for the whole passage. Between upstream rotor segments there are disturbances in the freestream due to the accumulation of turbulence from the upstream passages. Despite differences in terms of geometry and running conditions, both testcases show strong similarity. It can be seen that the wake segments propagate in similar way and are distorted in similar way.

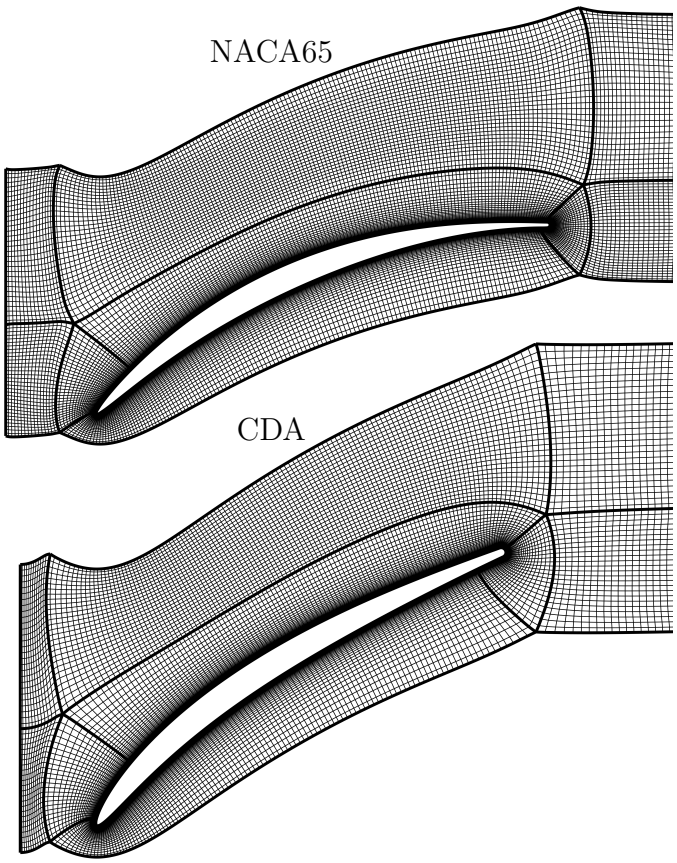

Figure 7.2: Mesh used for this study showing every 8^{th} grid line.

7.2 The effect of axial gap on unsteadiness

To characterize the nature of the turbulence in the multi-stage environment a freestream inlet probe is employed. The velocity trace recorded for NACA65 testcase at two gap extents of 0.30 and $0.40C_{ax}$ using this probe can be seen in Figure 7.4 where a clear repeating pattern of wake passings can be seen. The turbulence spectrum, Figure 7.4, shows the presence of peaks at the wake passing frequency of $273.13Hz$ and its harmonics.

The wake recycling routine does not carry any assumptions about the freestream turbulence intensity levels or length scales. This eliminates one of the most significant unknowns when performing high-fidelity simulations, i.e. the choice of freestream turbulence at the inflow. As a result, the energy cascade, shown in Figure 7.4, evolved naturally and shows large inertial range that compares favorably with Kolmogorov's $-5/3$ law.

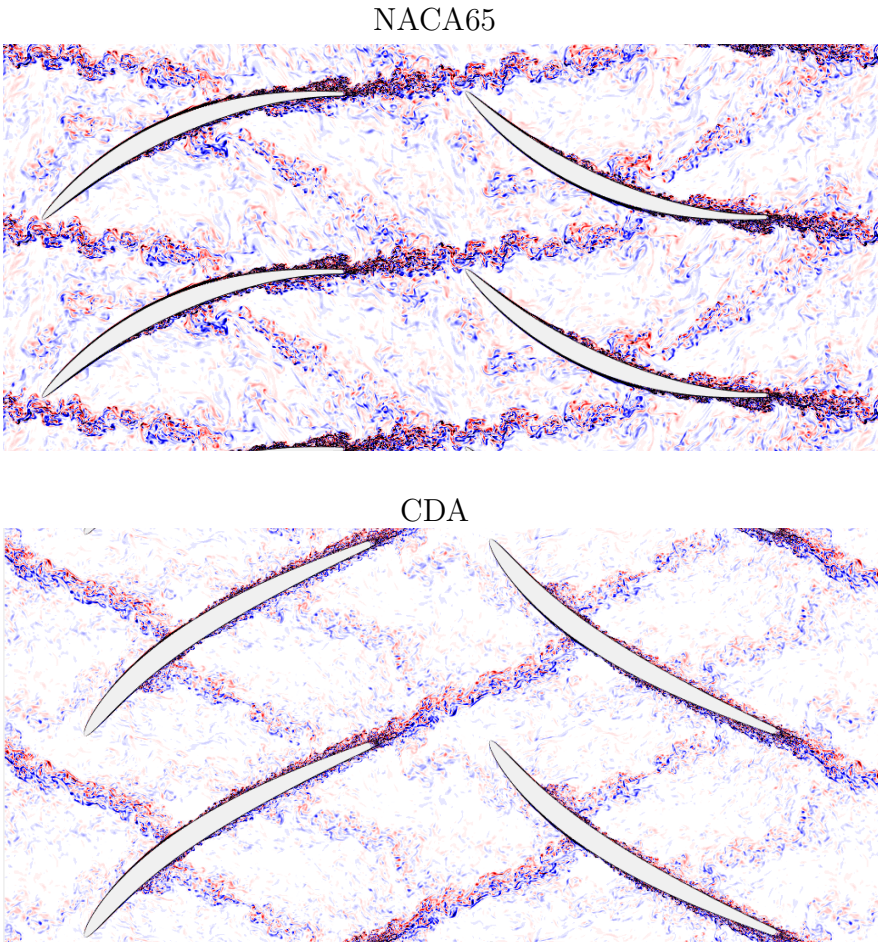

Figure 7.3: Instantaneous spanwise vorticity flowfield of a stator row of a repeating-passage simulation for the NACA65 and CDA blade profiles.

It is also clear that as the gap is reduced from 0.40 to $0.30C_{ax}$ both periodic and turbulent unsteadiness rises. The periodic unsteadiness can be best seen on the velocity trace where much higher variability of velocity can be seen. The turbulent unsteadiness is best displayed by the raised level of energy on the turbulence spectrum across all the scales.

The increase in unsteadiness can be further quantified by looking at the average periodic and turbulent unsteadiness. For this purpose we take phase-averaged flow solutions and split the effect of periodic and turbulent fluctuations by defining turbulent and periodic intensities:

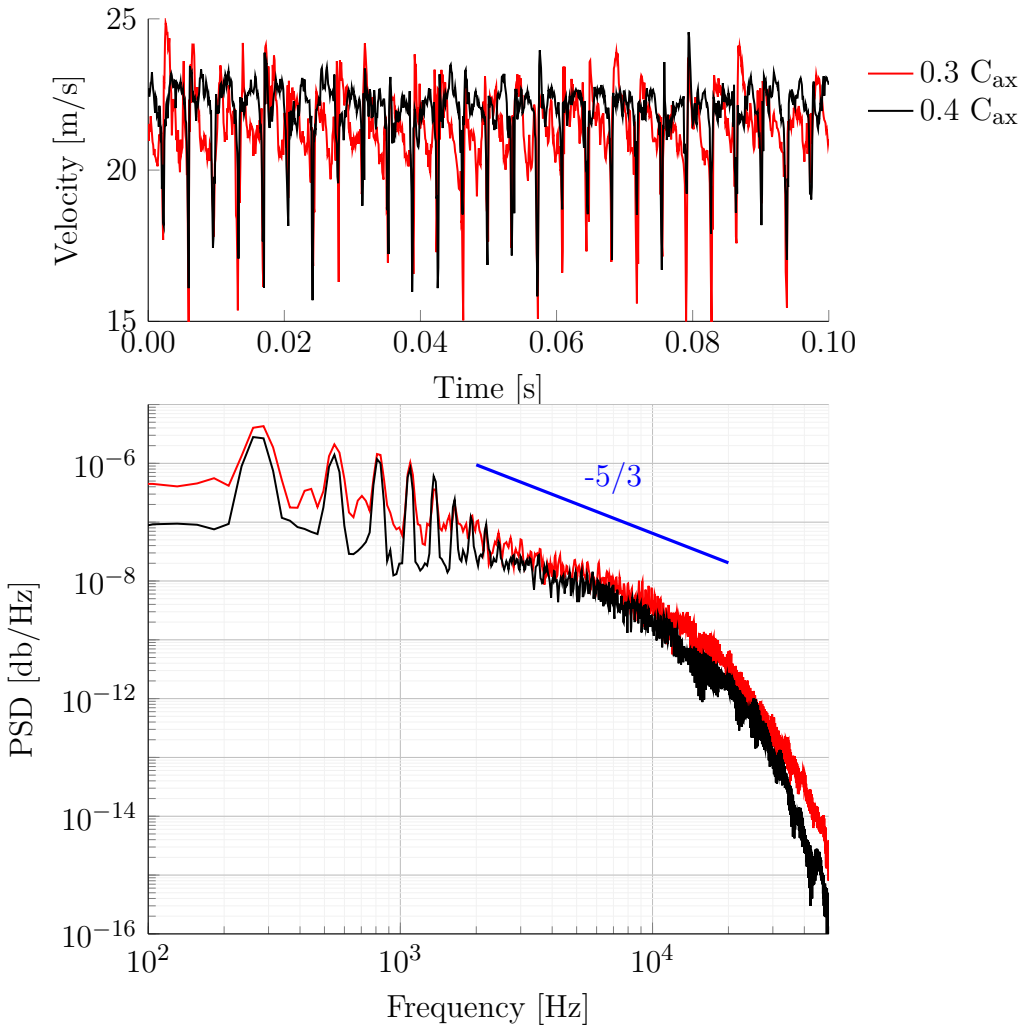

Figure 7.4: Velocity trace (upper) from the inlet freestream probe of NACA65 blade at two different gaps (0.3 and $0.4C_{ax}$) and associated Fourier spectrum of the signal (lower).

$$
\begin{aligned}
Tu &= \frac{1}{N_{phases}} \sum_{N_{phases}} \sqrt{\frac{1}{3}\overline{u_i' u_i'}}/U_{ref} \\
Pu &= \frac{1}{N_{phases}} \sum_{N_{phases}} \sqrt{\frac{1}{3}\overline{u_i^* u_i^*}}/U_{ref}
\end{aligned}
\tag{7.1}
$$

These quantities are averaged at the plane at $0.15C_{ax}$ upstream from the leading edge of the blade to characterize the inlet unsteadiness. Figure 7.5 shows the effect of axial gap on periodic and turbulent unsteadiness at the inlet of the passage. When the gap is reduced the periodic unsteadiness (Pu) rises sharply for both cases from

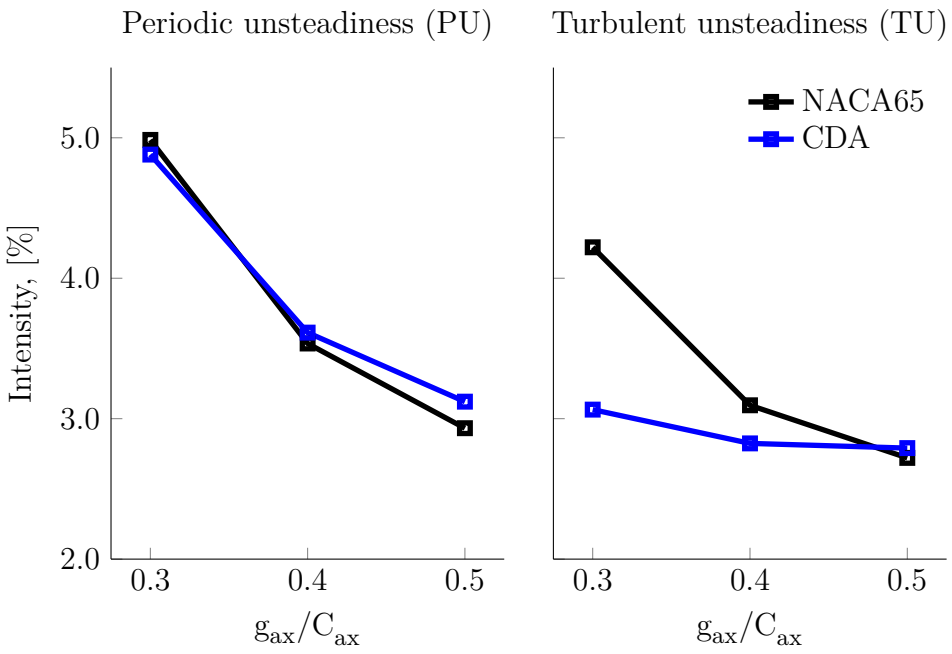

Figure 7.5: Comparison of decomposed periodic and turbulent unsteadiness for both NACA65 and CDA testcases showing increase in both as the gap is reduced.

approximately 3% to 5%. The turbulence intensity (Tu) also rises, but that rise is not as dramatic for the CDA testcase as for the NACA65.

7.3 The effect of axial gap on loss

Figure 7.6 shows that loss for both cases exhibits similar behavior, i.e. stays relatively constant as the gap is initially reduced from 0.50 to $0.40C_{ax}$ and then rises sharply as the gap is further reduced from 0.40 to $0.30C_{ax}$. This sharp rise translates into an increase of 5.5% and 9.5% in loss for NACA65 and CDA testcases, respectively. The rest of the study will focus on explaining the arising trends as the gap is varied from large to small. To do that one has to find out what drives the change in loss.

7.4 The role of turbulence production on loss

To understand the mechanism driving loss it is important to understand turbulence production, because it is the production of turbulence which extracts useful mechanical energy from the mean flow. Our analysis exploits the fact that in our repeating passage calculation turbulence properties at the inlet and outlet are the same. This means

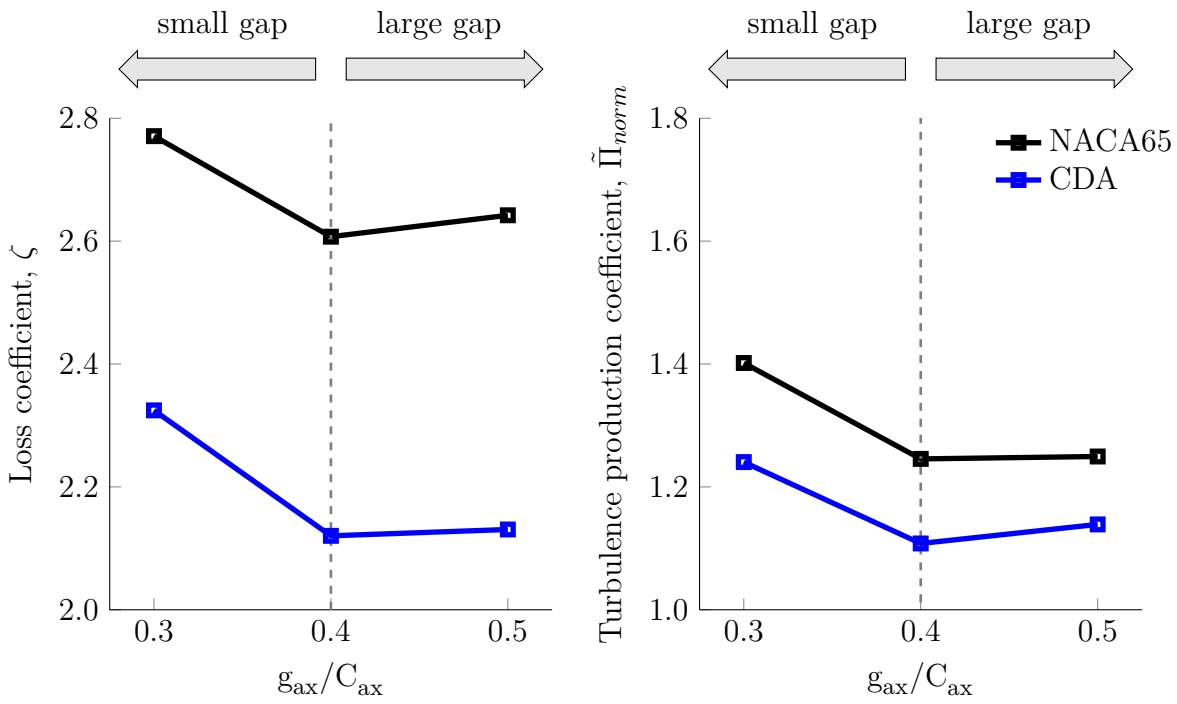

Figure 7.6: Variation of loss coefficient (left) and turbulence production coefficient (right) with axial gap.

that the overall production of turbulence will be at an exact balance with turbulence dissipation and therefore loss generated by the turbulence. To do that we will integrate turbulence production as defined in Chapter 6 across the domain and normalize it in such a way to evaluate its direct contribution to loss coefficient:

$$\widetilde{\Pi}_{norm} = \frac{\rho_{in}}{\dot{m}} \int_{\Omega} \overline{\langle u_i' u_j' \rangle \frac{\partial \left(\bar{u}_i + u_i^*\right)}{\partial x_j}} d\Omega / 0.5 U_{ref}^2 \tag{7.2}$$

As can be seen in Figure 7.6 not only the trends of loss and turbulence production are the same, but also the magnitudes of change are similar. As a consequence to understand changes in loss the study will focus on mechanisms of turbulence production. In addition, because the same trends are observed for both testcases for the sake of simplicity NACA65 testcase will be used to determine the causes for this rise in turbulence production and to explain how axial gap affects the flow within the machine. Later it will be shown that the same behavior is true for the the CDA testcase.
Firstly, the turbulence production coefficient for NACA65 testcase was split it into contributions from the boundary layers and freestream. The boundary layer areas were defined according to a boundary layer edge detection method based on vorticity criterion and the resulting split can be seen in Figure 7.7. The gap of $0.40C_{ax}$ will be

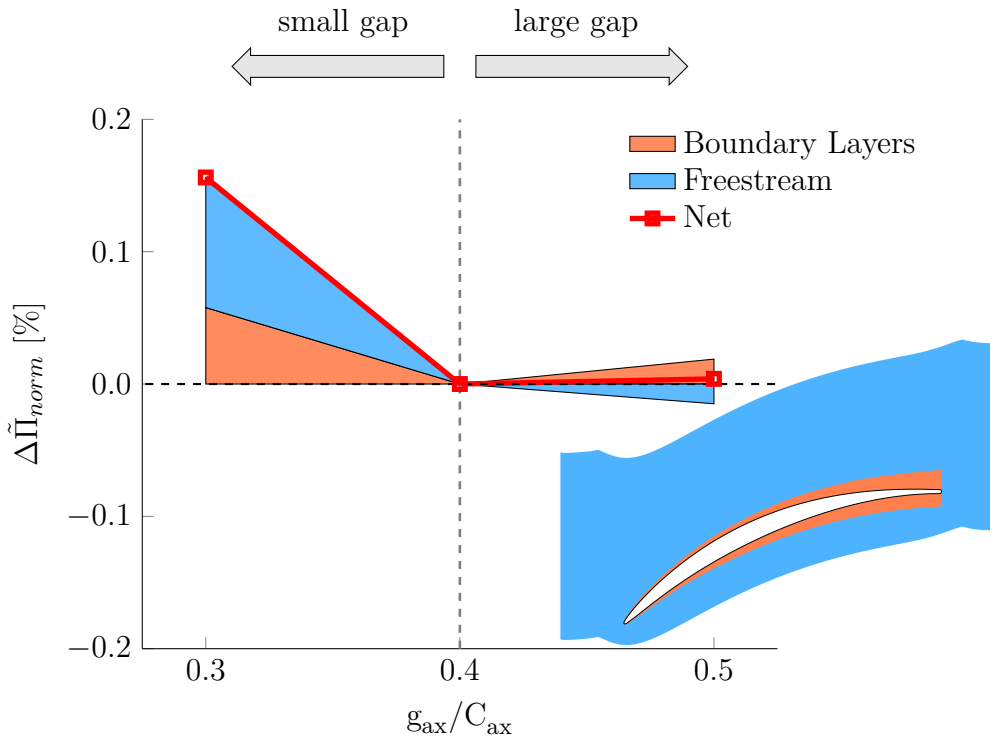

Figure 7.7: Contribution to turbulence production coefficient from the boundary layers and freestream for NACA65 testcase.

taken as the nominal gap size here and it will be shown how turbulence production coefficient changes as the gap increased or decreases in size.

Figure 7.7 shows relative changes in turbulence production coefficient as the gap is varied. In addition, it quantifies contributions from boundary layers and freestream to the overall production. It can be observed that as gap is reduced, turbulence production due to both boundary layers and freestream rises giving a net increase of 0.15% points in loss coefficient. On the other hand, as the gap is increased the overall turbulence production stays relatively constant. This is because contributions from boundary layers and freestream production are of similar proportion and opposite direction - freestrom production slightly decreases and boundary layer production slightly increases. The following two sections will discuss, firstly, boundary layer behavior and, secondly, freestream behavior as the gap is varied.

Figure 7.8 shows the space-time diagram of shear stress displaying the unsteady transition behavior on the suction-surface as the gap is varied. Separation line representing a zero velocity contour is plotted in green. Structures moving over the surface appear as wedges in the space-time diagrams that propagate across the surface. It is clear that the boundary layer transition is changing with gap. For larger gap ($0.50C_{ax}$)

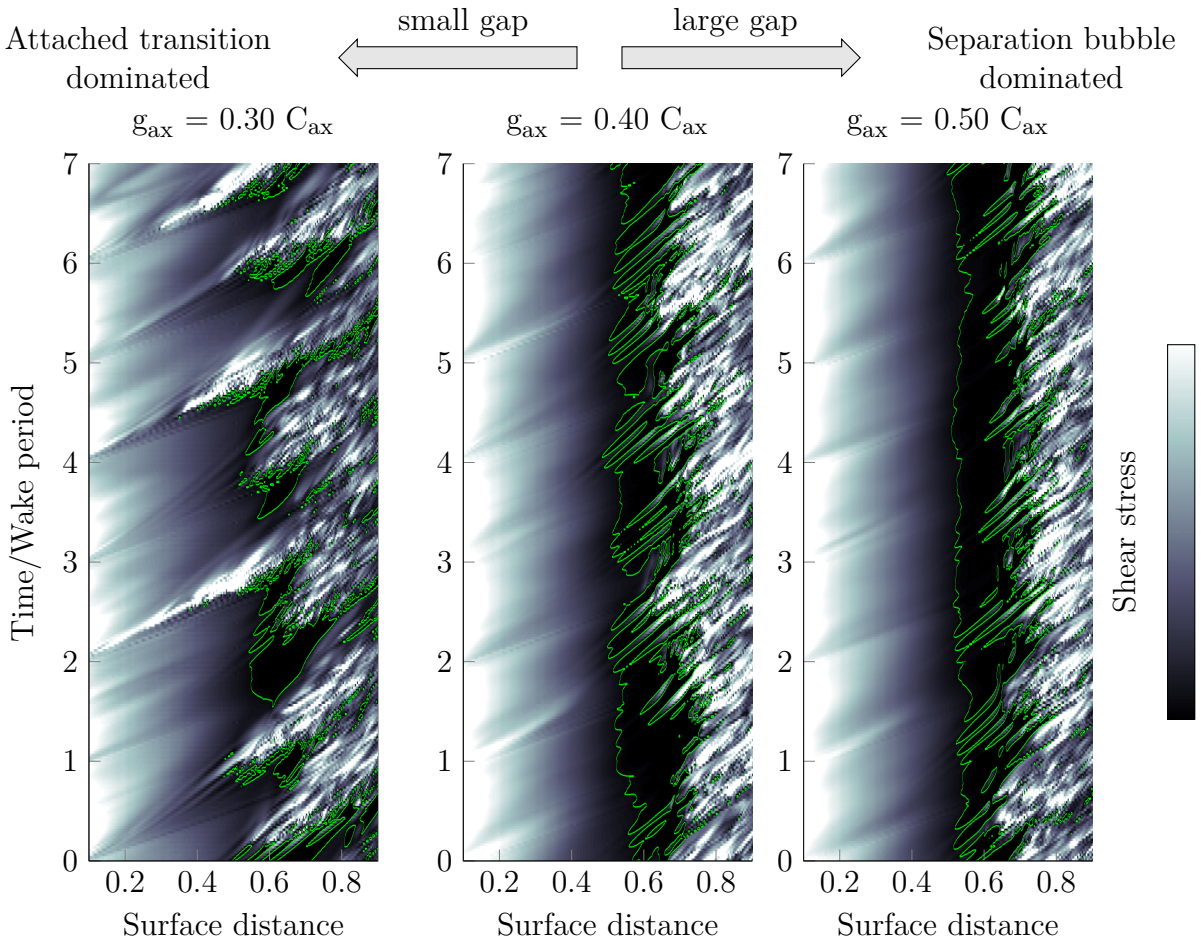

Figure 7.8: Spacetime diagram of shear stress of suction surface for all the axial gaps. Region of separated flow is outlined with a zero velocity contour (green).

the flow tends to be more separated. For smaller gap ($0.30C_{ax}$) wake induced transition in the form of turbulent wedges suppresses separation. The effect of transition behavior on turbulence production will be explored next.

The effect of separation bubble on turbulence production. To understand the effect of separation on turbulence production let us define the integrated turbulence production across the boundary layer according to Equation 7.3:

$$\widetilde{\Pi}_{BL} = \frac{1}{U_e^3} \int_{\delta} \overline{\langle u_i' u_j' \rangle \frac{\partial (\bar{u}_i + u_i^*)}{\partial x_j}} dy \tag{7.3}$$

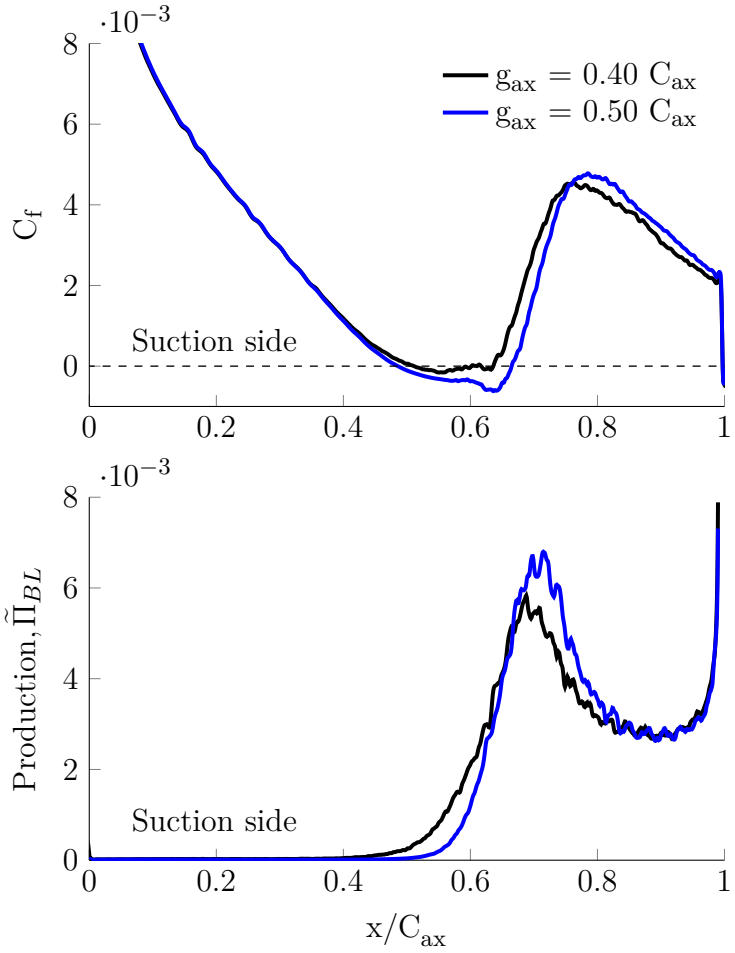

Figure 7.9: The effect of separation bubble on turbulence production.

Figure 7.9 shows skin friction and integrated turbulence production across suction side boundary layer of the NACA65 testcase for the nominal gap of $0.40C_{ax}$ and large gap of $0.50C_{ax}$. It can be seen that for the large gap separation bubble is larger than for the nominal gap as seen on the time averaged skin friction plot. Large separation bubbles lead to higher turbulence production in the reattachment region. Axial gap affects the size of the separation bubble and as the gap is initially reduced from large to nominal, the reattachment region moves upstream, peak integrated turbulence production decreases and overall boundary layer contribution decreases. Next paragraph explains what happens as the gap is furthered reduced.

The effect of attached transition on turbulence production. From space-time diagrams shown in Figure 7.8 it can be seen that as the gap is reduced the interaction between incoming wakes and boundary layer is much stronger. To understand why

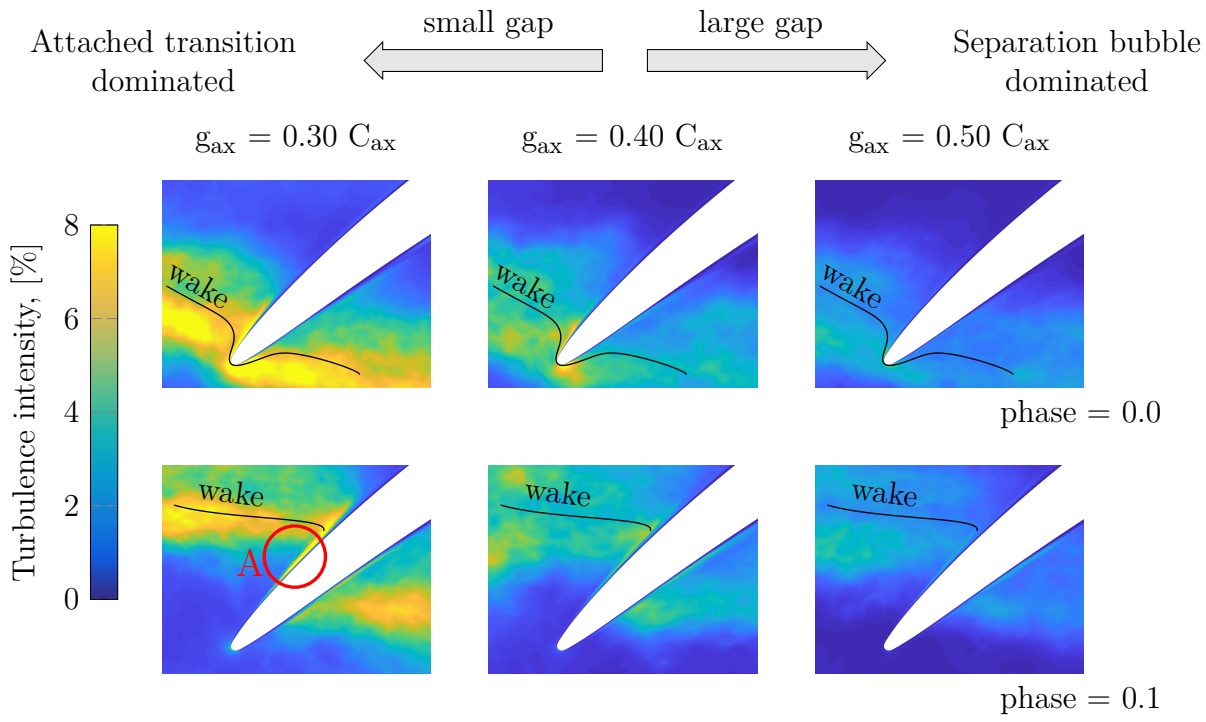

Figure 7.10: Wake boundary layer interaction increases as the gap is reduced resulting in creation of turbulent spots.

closing the gap leads to stronger interaction ensemble averaged turbulent kinetic energy contour plots are used as shown in Figure 7.10. There is a large difference in turbulent kinetic energy level in the wake for different gaps. Turbulence intensity in the center of the wake ranges between 8% for $0.30C_{ax}$ and 4% for $0.50C_{ax}$. This results in much stronger interaction between wake and the boundary layer that leads to wake induced transition. The signature of this interaction is elevated turbulent kinetic energy within the boundary layer as observed for gap $0.30C_{ax}$, label A on the same figure. This earlier transition results in higher turbulent wetted area and higher turbulence production. Consequently an increase in boundary layer turbulence production is observed as the axial gap is both - increases and decreased. Increasing the gap reduces wake boundary layer interaction and increases separation bubble and therefore turbulence production. Decreasing the gap leads to stronger wake boundary layer interaction and thus higher turbulent wetted area and higher turbulence production.

In the next section the effect of gap on freestream turbulence production is discussed and the mechanism behind it is investigated.

The effect of axial gap on freestream turbulence production. Turbulence production can be computed at each rotor phase using the decomposition described in Equation 3.19:

$$\langle \Pi \rangle = -\langle u_i' u_j' \rangle \frac{\partial \langle \bar{u}_i + u_i^* \rangle}{\partial x_j} \tag{7.4}$$

The effect of rotor wakes on turbulence production has been previously studied in the context of low-pressure turbines (LPT) by Stieger and Hodson [97] and Michelassi et al. [63]. In LPT passages, the high loading leads to significant wake straining within the stator passage and this leads to additional turbulence production.
In order to determine whether a similar phenomenon affects the freestream turbulence production in compressors, we follow the method of Stieger and Hodson [97] and decompose the strain and stress tensors into their principal components. for that purpose turbulent stress, R_{ij}, and strain-rate, S_{ij}, tensors are defined:

$$\begin{aligned} \langle R_{ij} \rangle &= \langle u_i' u_j' \rangle \\ \langle S_{ij} \rangle &= \frac{1}{2} \left(\frac{\partial \langle U_i + \tilde{u_i} \rangle}{\partial x_j} + \frac{\partial \langle U_j + \tilde{u_i} \rangle}{\partial x_i} \right) \end{aligned} \tag{7.5}$$

From these principal stress ψ and strain θ angles along which the shear stress and shear strain components are equal to zero can be calculated:

$$\begin{aligned} \langle \psi \rangle &= \frac{1}{2} \tan^{-1} \left(\frac{2\langle R_{xy} \rangle}{\langle R_{xx} \rangle - \langle R_{yy} \rangle} \right) \\ \langle \theta \rangle &= \frac{1}{2} \tan^{-1} \left(\frac{2\langle S_{xy} \rangle}{\langle S_{xx} \rangle - \langle S_{yy} \rangle} \right) \end{aligned} \tag{7.6}$$

From these principal stresses can be obtained:

$$\begin{aligned} \langle R_{xx,\psi} \rangle &= \langle R_{xx} \rangle \cos^2\langle \psi \rangle + \langle R_{yy} \rangle \sin^2\langle \psi \rangle + \langle R_{xy} \rangle \sin\langle \psi \rangle \cos\langle \psi \rangle \\ \langle R_{yy,\psi} \rangle &= \langle R_{xx} \rangle \cos^2\langle \psi \rangle + \langle R_{yy} \rangle \sin^2\langle \psi \rangle - \langle R_{xy} \rangle \sin\langle \psi \rangle \cos\langle \psi \rangle \end{aligned} \tag{7.7}$$

And the principle strains can be calculated in a similar manner:

$$\begin{aligned} \langle S_{xx,\theta} \rangle &= \langle S_{xx} \rangle \cos^2\langle \theta \rangle + \langle S_{yy} \rangle \sin^2\langle \theta \rangle + \langle S_{xy} \rangle \sin\langle \theta \rangle \cos\langle \theta \rangle \\ \langle S_{yy,\theta} \rangle &= \langle S_{xx} \rangle \cos^2\langle \theta \rangle + \langle S_{yy} \rangle \sin^2\langle \theta \rangle - \langle S_{xy} \rangle \sin\langle \theta \rangle \cos\langle \theta \rangle \end{aligned} \tag{7.8}$$

Figure 7.11 shows the principal stress and strain components alongside turbulent production contours for one of the rotor phases. It is clear from the figure that the regions of increased turbulence production correspond to the regions where principle

stress and strain vectors are aligned and at opposite direction (Equation 7.4). As the wake convects across the passage its strain field interacts with the Reynolds stresses leading to the extraction of work from the mean flow and elevated turbulence production. It can be observed that as the gap is reduced the interaction between strain field and Reynolds stresses becomes stronger, especially within the wake segments. As a consequence freestream turbulence production rises increasing freestream loss.

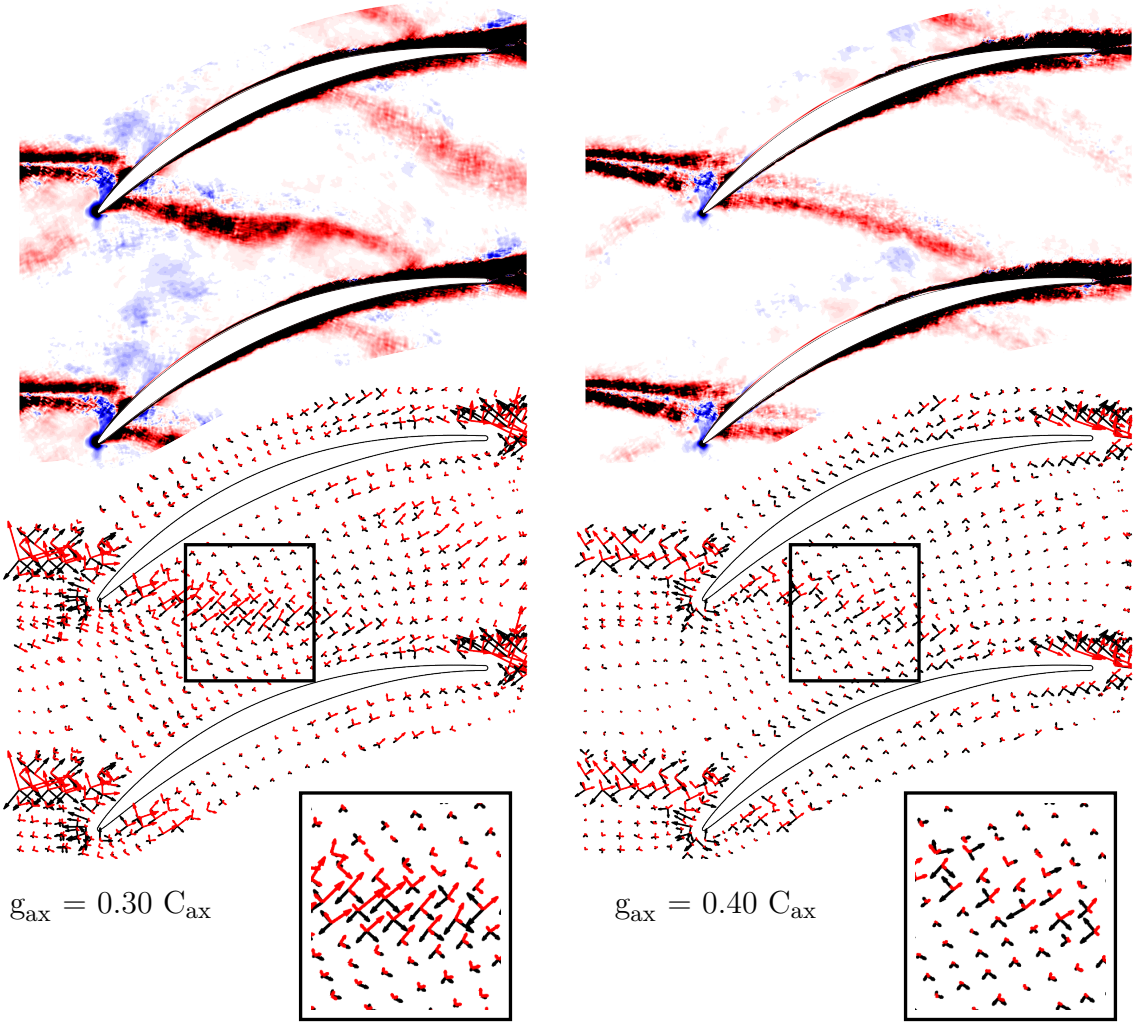

Figure 7.11: Turbulence production contours (upper) and vectors of principle strain (black) and principle stress (red) components (lower) at one of the rotor phases for $g_{ax} = 0.30C_{ax}$ (left) and $g_{ax} = 0.40C_{ax}$ gaps.

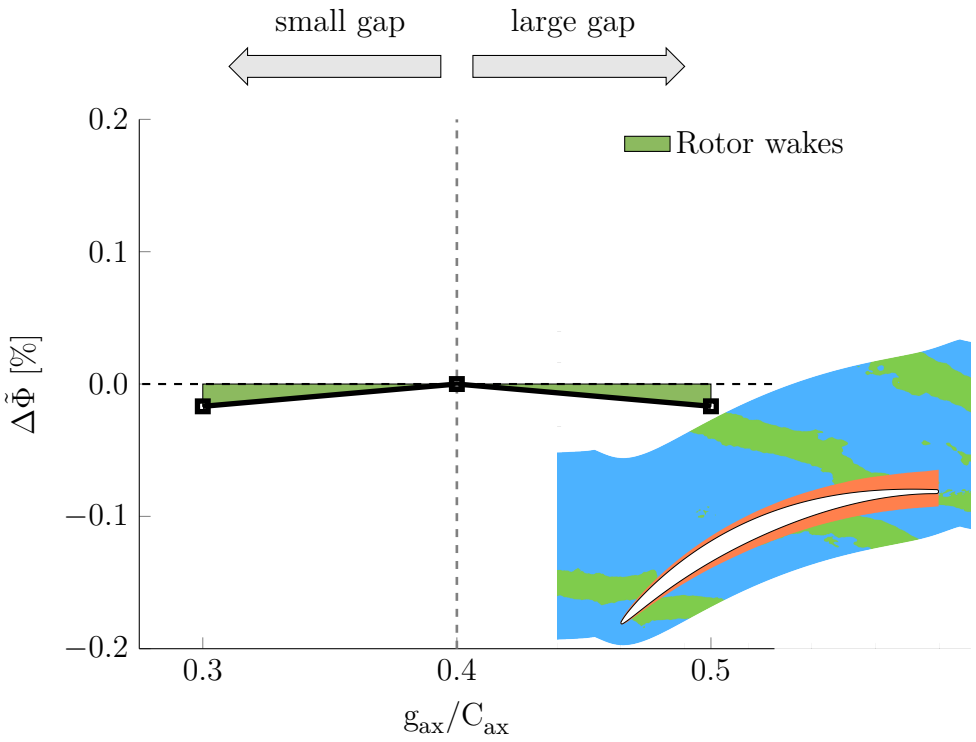

Figure 7.12: Variation of wake dissipation coefficient for NACA65 testcase.

7.5 The effect of axial gap on wake recovery

It is useful to compare the importance of turbulence production to wake recovery effect. Wake recovery effect will tend to reduce mixing loss as axial gap is reduced [95, 26, 107]. However, in the cases considered here the loss due to freestream turbulence production was observed to increase as the gap was reduced. The following analysis aims to determine the magnitude of wake recovery effect.
In order to quantify wake recovery effect we integrate viscous dissipation through the rotor wake segments. To separate upstream rotor wakes from the background turbulence, a detector function shown in the previous Chapter was used. As before, the detector was set equal to 1 in regions where at least two out of three conditions were true: i.e. $u^* < 0$ and/or $\langle u_i' u_i' \rangle > \overline{u_i' u_i'}$ and/or $\langle \Phi_f \rangle > \overline{\Phi_f}$.

The viscous dissipation is integrated through the rotor wake segments and normalized in such a way that it gives a direct contribution to loss coefficient, Equation 7.9.

$$\widetilde{\Phi} = \frac{\rho_{in}}{\dot{m}} \int_{\Omega} \tau_{ij} \frac{\partial u_i}{\partial x_j} d\Omega / 0.5 U_{ref}^2 \tag{7.9}$$

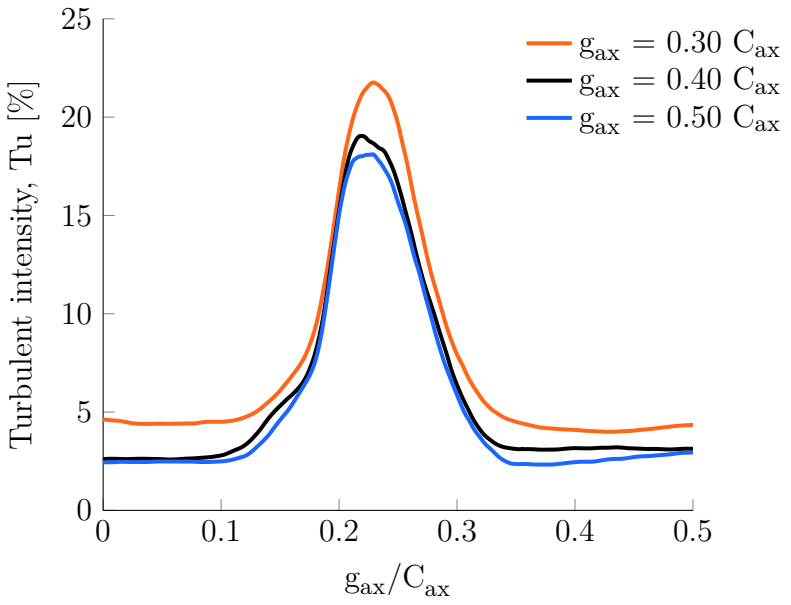

Figure 7.13: The profile of wake turbulence intensity on the plane located $0.15C_{ax}$ downstream of the trailing edge for NACA65 testcase for all three gaps.

The process is repeated for all the phases in the phase averaged solutions to compute the overall time averaged loss due to viscous dissipation in rotor wake segments. A relative change in loss is then computed as compared to the nominal gap of $0.40C_{ax}$. Figure 7.12 shows that the change in loss due to rotor wakes as the gap is varied is small. In fact, as the gap is reduced from $0.40C_{ax}$ to $0.30C_{ax}$ the loss due to rotor wakes decreases by 0.02% points while loss due to turbulence production increases by 0.15% points. In addition, it can be observed that there is no strong trend as the gap is varied - loss due to rotor wakes reduces as gap is both reduced and increased. The results therefore suggest that wake recovery effects are small compared to turbulence production mechanisms.

It is important to note that the current analysis does not consider the impact of unsteady potential effects on wake development and loss generation. As described in more detail in Chapter 3, the repeating-passage model was set up and implemented to only sample and recycle vortical disturbances (and exclude pressure and density disturbances). This decision was guided by the literature review which identified the interaction of deterministic and stochastic unsteadiness as one of the biggest unknowns that scale resolving simulation may help better understand. As a result, the focus of these simulations has been put on these interactions.

At engine conditions unsteady potential effects will increase in strength, especially as axial gaps are reduced and Mach numbers are increased. As a result, current findings

cannot be easily extrapolated to configurations operating at significantly higher Mach numbers or configurations which are more compact. This could be addressed by either developing the repeating-passage model further to include density and pressure interactions or by using current results to develop a low-order model that could be fed into a multi-stage (U)RANS simulation to improve the prediction of turbulent unsteadiness and its impact on performance.

7.6 Multi-stage feedback effect on turbulence production

In order to understand why wake recovery effect is not consistently reducing loss as gap is reduced we compare the wakes downstream of the trailing edge of the stator. Figure 7.13 shows the profiles of turbulence intensity across the wakes. It can be seen that as the gap is varied the wake intensity also changes. In fact, as the gap is reduced from 0.40 to $0.30C_{ax}$ there is a higher peak and a broader profile of turbulence intensity. More turbulent kinetic energy in the wake results in higher wake mixing and thus increased viscous dissipation and loss. As a consequence, the benefit of wake recovery due to reduced time for the upstream wake to mix out is offset by a higher content of turbulent kinetic energy within the wake.

For simplicity the analysis focused on NACA65 case, but both mechanisms are also present for CDA case where similar trends are present. The key difference between CDA profile and the NACA65 is the loading distribution (see Figure 7.1). The adverse pressure gradient on the suction surface of CDA geometry is initially comparatively steep and then decreases in strength towards the trailing-edge.
Figure 7.14 shows how loss due to wake recovery and turbulence production mechanisms changes as the gap is decreased from the $0.40C_{ax}$ to $0.30C_{ax}$. It is clear that the reduction in loss due to wake recovery is small, i.e. within 1% for both testcases. On the other hand, turbulence production mechanisms increase the loss by over 6% for both cases and dominate the overall performance. Therefore, despite different geometries and running conditions, a similar effect of axial gap on performance is observed in both cases.

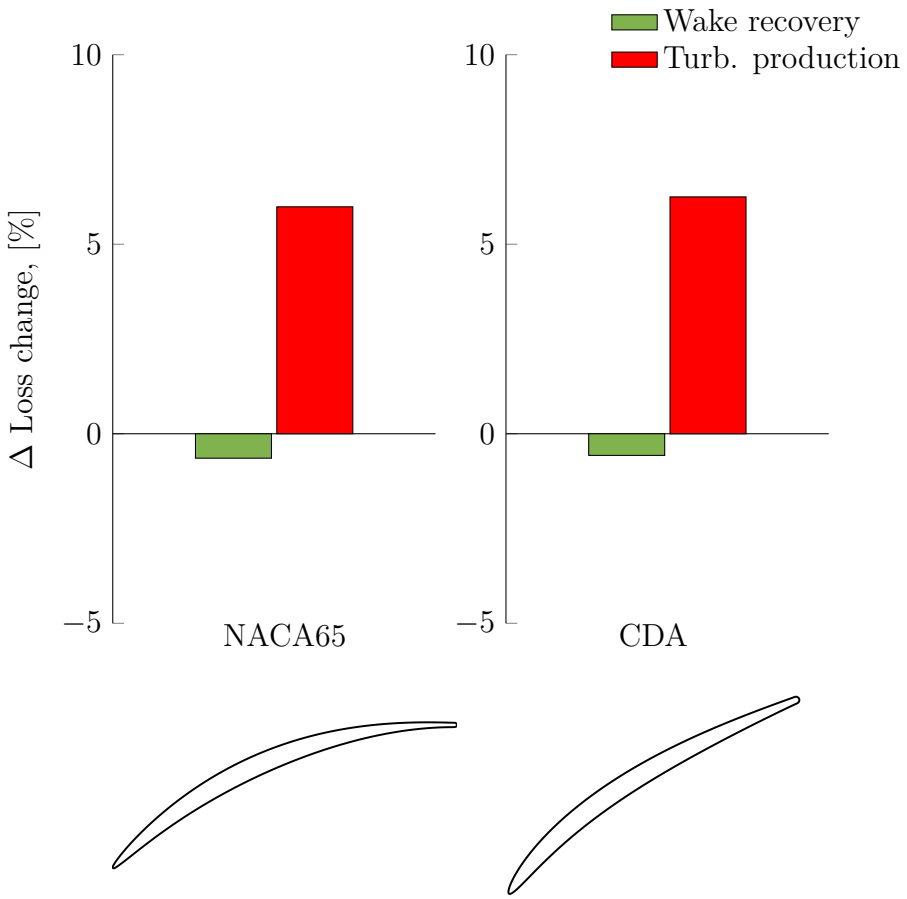

Figure 7.14: The comparison of loss change for NACA65 and CDA testcases due to wake recovery (green) and turbulence production (red) as the gap is reduced from 0.40 to0.30C_{ax}.

7.7 Conclusions

In this chapter the repeating-passage model was used to study the origin and nature of turbulence within the multi-stage machine as well as the effect of rotor-stator gap has on the freestream turbulence and loss generation.

The simulations, which do not rely on any assumptions with regards to the incoming unsteadiness, showed that turbulence in multi-stage environment has a broad spectrum in good agreement with Kolmogorov's $-5/3$ law. The unsteadiness levels varied between 3 and 5% for periodic unsteadiness and between 3 and 4% for turbulent unsteadiness intensity for considered cases.

The results show that rotor-stator gap plays critical role in turbulence production and determines the unsteadiness in multi-stage environment. Consequently, the gap

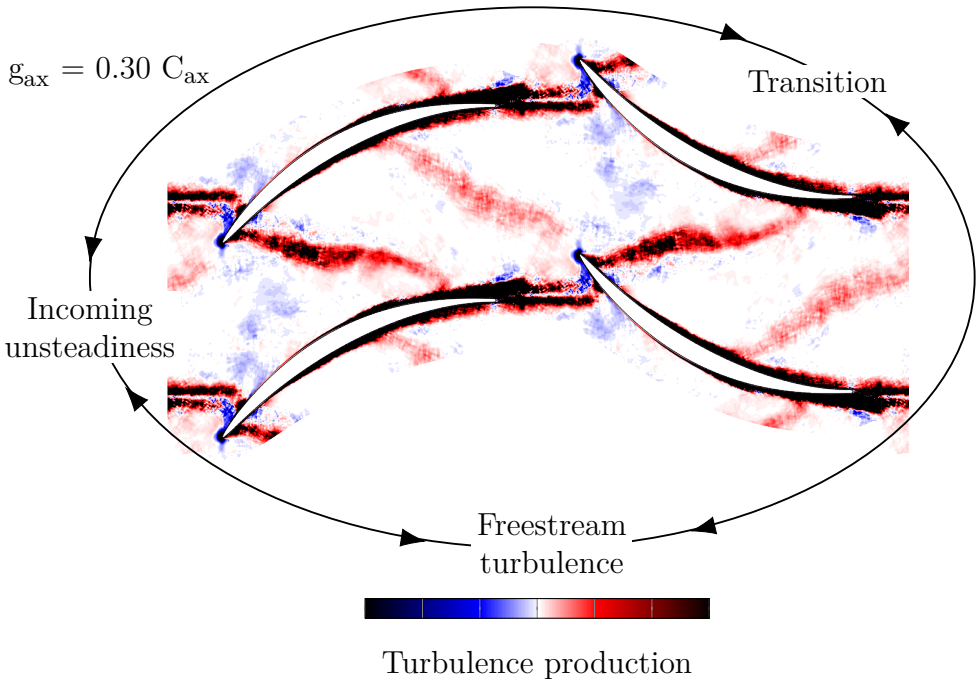

Figure 7.15: Multi-stage feedback mechanism resulting in higher turbulence production as the gap is reduced.

has significant effect on the overall loss. This sensitivity of loss with axial gap is due to a feedback mechanism: as the gap is reduced, the strength of the wake boundary layer interaction within the stator increases, driving increases in turbulence production within the freestream and boundary layers. This turbulence, whether it is generated in the boundary layers or the freestream is then convected into the freestream, and itself raises freestream turbulence intensity, driving further turbulence production. Eventually, the turbulence is dissipated, thus increasing overall loss. This mechanism appears to outweigh any beneficial effects due to wake recovery.

This phenomenon was observed for two compressor geometries: a traditional NACA65 profile and a modern CDA profile and led to an increase in loss of $5.5 - 9.5\%$ for the tested conditions. In a real machine there will be additional effects due to three dimensional flows and end-wall boundary layers. These effects will also impact the turbulence and loss generation within the machine and it remains to be understood what the impact is.

Including effects of unsteadiness can have significant implications on predictive capabilities of models especially as gas turbines are moving towards more compact designs and the aim of this work is to better inform future designs with respect to loss generation.

Chapter 8

Conclusions and Recommendations for Future Work

8.1 Conclusions

The aim of this thesis was to investigate loss mechanisms in compressor flows at industrially relevant conditions using high-fidelity simulations. Literature review revealed that one of the major sources of uncertainty with regards to compressor flows was the unsteadiness. The work performed in this thesis was therefore focused on the impact of the unsteadiness on compressor loss, specifically at the mid-span section of a compressor.

8.1.1 Accurate prediction of loss using high fidelity methods

In the first part of the thesis, the problem of accurate loss prediction was addresses. Lack of formal resolution guidelines and high sensitivity of scale-resolving simulations to mesh refinement meant that loss predictions depended on the chosen convergence criteria. Chapter 4 and Chapter 5 examined computational requirements for capturing loss. The results showed that accurate loss predictions for turbomachinery flows require:

- capturing local entropy generation rate;
- capturing the inception and growth of instabilities leading to transition;

It was demonstrated in Chapter 4 that capturing local entropy generation rate can be achieved without the need for resolving the full dissipation spectrum. It was shown that accurate prediction was warranted as long as resolution was sufficient to resolve all the scales down to around 10 Kolmogorov lengthscales ($10\eta_{Kol}$). It was further

determined that for the 8^{th} order scheme this requirement translated to the effective resolution of cell size, $\Delta \leq 4\eta_{Kol}$.

In Chapter 5, NACA65 compressor cascade subject to freestream turbulence was employed to show that the accuracy of loss prediction depends predominantly on capturing instability mechanisms upstream of transition, and the subsequent turbulence production. It was found that the interaction of freestream turbulence at the leading-edge and development of streaks in the laminar region of the boundary layer were critical to capturing the correct transition and therefore loss mechanisms. Capturing the formation of these instabilities is dependent on the dispersion properties of the numerical scheme and mesh size. For Tam&Webb numerical scheme used for this study, a spanwise cell size of $\Delta_z/C_{ax} \approx 0.001$ was required to capture this phenomenon.

8.1.2 Unsteadiness in multi-stage compressors

In the second part of the thesis, the effects of unsteadiness within the multi-stage compressors are studied. For this purpose, a new type of high-fidelity simulation, which recreates the mid-span flowfield of an embedded stator in repeating-stage compressor was developed. This method does not rely on a-priori knowledge of the inflow turbulence and instead continuously recycles the disturbance field from a single-passage simulation to mimic multi-stage environment.

This setup was first used in Chapter 6 to examine unsteady energy transfers in compressors. Triply decomposed kinetic energy budgets were employed for this purpose. The results revealed an important role turbulence production (energy transfer from mean and periodic to turbulent flowfield) play in determining compressor performance. In addition, significant negative energy transfer rates were found in compressor passage manifesting an energy flow from periodic wakes to mean flowfield. This effect was linked to wake recovery effect, but its impact on loss generation is unclear.

In Chapter 7, the repeating passage model was used with two compressor geometries: NACA65 and CDA with three different rotor-stator gaps. The simulations showed that flowfield developed a broad turbulence spectrum in good agreement with Kolmogorov's $-5/3$ law. The unsteadiness levels varied between 3 and 5% for periodic unsteadiness and between 3 and 4% for turbulent unsteadiness intensity for considered cases. The results showed that the rotor-stator gap plays a critical role in turbulence

production and unsteadiness in the multi-stage environment. Consequently, the gap has a significant effect on the overall loss. This sensitivity of loss with axial gap was shown to be due to a feedback mechanism which occurs as the axial gap is varied.

As the gap is reduced, the strength of the wake interaction within the stator increased, driving increases in turbulence production within the freestream and within the boundary layers. This turbulence, whether it was generated in the boundary layers or the freestream was then convected into the freestream, and itself raised freestream turbulence intensity, driving further turbulence production. Eventually, the turbulence was dissipated, thus increasing overall loss. This mechanism appears to outweigh any beneficial effects due to wake recovery. This phenomenon was observed for both compressor geometries and led to an increase in loss of $5.5 - 9.5\%$ for the tested conditions.

It is important to mention that as the gap is reduced the strength of the unsteady potential effects on wake distortion and development would also increase. These interactions could also have a significant impact on the turbulence production and loss generation. However, they were not considered in this study as only vortical disturbances were recycled in the repeating-passage model. Nonetheless, testcases presented here offer a unique dataset that could be used as a validation for (U)RANS repeating-stage compressor studies focussed on turbulence modelling improvement. This is of particular interest with regards to the modelling of turbulent and deterministic unsteadiness.

8.2 Recommendations for future work

Accurate loss prediction analysis was performed primarily on cases which were weakly compressible ($Ma < 0.3$). Since high Mach numbers are common in compressors, it would be relevant to verify if resolution criteria presented here were also valid for flows which are highly compressible. This could be achieved by modifying Taylor-Green vortex test case and repeating the analysis done in Chapters 4 and 5.

Study of unsteady energy transfers revealed that periodic wakes transfer energy into the mean flow of a compressor and therefore have a potential to increase mechanical work potential. While the net effect of this transfer on loss was unclear, it would be of interest to study whether it could be exploited to improve compressor performance. This could be achieved through blade profile changes that aim at maximizing the amount of wake stretching and re-orientation.

Analysis of multi-stage compressor loss mechanisms showed that there is a feedback between freestream and boundary layer turbulence production mechanisms that ultimately determines flow unsteadiness and compressor performance. In the thesis, it was shown how turbulent kinetic energy embedded within the wake translated into larger wetted turbulent area. However, a more detailed investigation into unsteady boundary layer behavior is suggested, especially with regards to the impact of rotor wakes on suction side boundary layer loss under different running conditions.

Previous work on the effect of relative phase of upstream wake on compressor performance showed that wake-phasing could offer a potential benefit, Nolan et al. [73]. An addition of wake-phasing to the repeating passage model would allow for first of a kind high-fidelity study of this effect on multi-stage compressor flowfield in a highly controlled manner.

Chapter 7 uncovered high degree of inter-dependency of various flow features on one another. Given this complex interaction and its impact on the unsteadiness, it is suggested that minimization of multi-stage compressor loss requires an integrated approach. Such approach would need to consider losses generated within the compressor blade-row as well as those caused by the unsteadiness carried downstream. This is expensive to implement experimentally, but could be mimicked numerically with high-fidelity simulations. To become a design tool, the code would require several improvements, such as an addition of sliding planes so that geometries with unequal number of rotor and stator blades can be considered.

In a real machine with shorter inter-row gaps and higher operating Mach numbers previously mentioned unsteady potential effects may also have a large impact on loss generation. In the future it would be desirable to understand how the coupled effect of unsteadiness interactions and unsteady potential effects have on compressor performance. In addition, this work focused on the mid-span mechanisms. Along with these mechanisms there will be additional effects due to three dimensional flows and end-wall boundary layers. These effects would also impact the turbulence production and loss generation within the multi-stage machine and it remains to be understood what that impact is.

Lastly, given the highly unsteady nature of the flow it may be interesting to ex-

plore whether phase averaged flowfield is representative of flow dynamics governing multi-stage behavior given many competing and inter-connected mechanisms. This could be investigated by employing data-driven flow decomposition and dimension reduction techniques, e.g. Proper Orthogonal Decomposition (POD), Dynamic Mode Decomposition (DMD) and other methods from dynamical systems theory.

Bibliography

[1] Adamczyk, J. J. (1996). Wake mixing in axial flow compressors. *Proceedings of ASME Turbo Expo.*

[2] Alam, M. and Sandham, N. D. (2000). Direct numerical simulation of short laminar separation bubbls with turbulent reattachment. *J. Fluid Mech.*

[3] Andersson, P. H., Berggren, M., and Henningson, D. S. (1999). Optimal disturbances and bypass transition in boundary layers. *Physics of Fluids.*

[4] Arts, T. and Lambert de Rouvroit, M. (1992). Aero-thermal performance of a two dimensional highly loaded transonic turbine nozzle guide vane: A test case for inviscid and viscous flow computations. *J. Turbomach.*

[5] Bailly, C. and Bogey, C. (2006). An overview of numerical methods for acoustic wave propagation. *ECCOMAS CFD.*

[6] Bhaskaran, R. and Lele, S. K. (2010). Large eddy simulation of free-stream turbulence effects on heat transfer to a high-pressure turbine cascade. *J. Turbulence.*

[7] Bogey, C. and Bailly, C. (2004). A family of low dispersive explicit schemes for flow and noise computations. *J. Comput. Phys.*

[8] Bowen, H. K. (2006). Pratt & whitney: Engineering standard work. case study 9-604-084. *Harvard Business School.*

[9] Bull, J. R. and Jameson, A. (2015). Simulation of the taylor-green vortex using high-order flux reconstruction schemes. *AIAA.*

[10] Camp, T. R. and H.-W., S. (1994). Turbulence intensity and length scale measurements in multistage compressors. *ASME J. Turbomach.*

[11] Carpenter, M. H., Gottlieb, D., and Abarbanel, S. (1994). Time-stable boundary conditions for finite-difference schemes solving hyperbolic systems: Methodology and application to high-order compact schemes. *Journal of Computational Physics.*

[12] Carpenter, M. H., Nordstrom, J., and Gottlieb, D. (1999). A stable and conservative interface treatment of arbitrary spatial accuracy. *Journal of Computational Physics.*

[13] Celik, I., Klein, M., Freitag, M., and Janicka, J. (2006). Assessment measures for urans/des/les: An overview with applications. *J. Turbulence.*

[14] Chen, L. W., Pichler, R., and Sandberg, R. D. (2013). Compressible dns of a low pressure turbine subjected to inlet disturbances. *DLES9: Workshop on Direct and Large-Eddy Simulation*.

[15] Choi, H. and Moin, P. (2012). Grid-point requirements for large eddy simulation: Chapman's estimatesrevisited. *Phys. Fluids*.

[16] Cimarelli, A., Leonforte, A. De Angelis, E., Crivellini, A., and Angeli, D. (2018). On negative turbulence production phenomena in the shear layer of separating and reattaching flows. *Phys. Lett. A*.

[17] Collado Morata, E., Gourdain, N., Duchaine, F., and Gicquel, L. (2012). Effects of freestream turbulence on high pressure turbine blade heat transfer predicted by structured and unstructured les. *Int. J. Heat Mass Transf.*

[18] Commission, E. (2011). Flightpath 2050 europe's vision for aviation. *Tech. Rep. European Commission*.

[19] Cui, J., Rao, V. N., and Tucker, P. G. (2017). Numerical investigation of secondary flows in a high-lift low pressure turbine. *International Journal of Heat and Fluid Flow*.

[20] Cui, J. and Tucker, P. (2017). Numerical study of purge and secondary flows in a low-pressure turbine. *ASME J. Turbomach.*

[21] Davidson, P. A. (2004). *Turbulence: An Introduction to Fluid Dynamics*. Oxford University Press.

[22] de Wiart, C. C., Hillewaert, K., Duponcheel, M., and Winckelmans, G. (2014). Assessment of a discontinuous galerkin method for the simulation of vortical flows at high reynolds number. *J. Numer. Meth. Fluids*.

[23] DeBonis, J. R. (2013). Solutions of the taylor-green and vortex problem and using and high-resolution explicit and finite difference and methods. *51st Aerospace Sceneces Meeting*.

[24] Denton, J. D. (1993). Loss mechanisms in turbomachines. *ASME J. Turbomach.*

[25] Denton, J. D. (2010). Some limitations of turbomachinery cfd. *Proceedings of ASME Turbo Expo*.

[26] Deregel, P. and Tan, C. S. (1996). Impact of rotor wakes on steady-state axial compressor performance. *Proceedings of ASME Turbo Expo*.

[27] Durbin, P. and Wu, X. (2007). Transition beneath vortical disturbances. *Annu. Rev. Fluid Mech.*

[28] Ekaterinaris, J. A. (2005). High-order accurate, low numerical diffusion methods for aerodynamics. *Progress in Aerospace Sciences*.

[29] F., H. A. K. M. and C., R. W. (1970). The mechanics of an organized wave in turbulent shear flow. *J. Fluid Mech.*

[30] Fischberg, C. J., Rhie, C. M., Zacharias, R. M., Bradley, P. C., and DesSureault, T. M. (1995). Using hundreds of workstations for production running of parallel cfd applications. *Parallel Computational Fluid Dynamics: Implementations and Results Using parallel Computers*.

[31] Fransen, R., Collado Morata, E., Duchaine, F., Gourdain, N., Gicquel, L., Vial, L., and Bonneau, G. (2011). Comparison of rans and les in high pressure turbines. *Proceedings of the 3ème Colloque INCA, ONERA*.

[32] Gao, F., Zambonini, G., Boudet, J., Ottavy, X., Lu, L., and Shao, L. (2015). Unsteady behavior of corner separation in a compressor cascade: Large eddy simulation and experimental study. *Journal of Power and Energy*.

[33] Garai, A., Diosady, L., Murman, S., and Madavan, N. (2018). Scale-resolving simulations of bypass transition in a high-pressure turbine cascade using a spectral element discontinous galerkin method. *J. Turbomach.*

[34] Geurts, B. J. and Fröhlich, J. (2002). A framework for predicting accuracy limitations in large-eddy simulation. *Physics of Fluids*.

[35] Gourdain, N. (2015a). Prediction of the unsteady turbulent flow in an axial compressor stage. part 1: Comparison of unsteady rans and les with experiments. *Comput. Fluids*.

[36] Gourdain, N. (2015b). Prediction of the unsteady turbulent flow in an axial compressor stage. part 2: analysis of unsteady rans and les data. *Comput. Fluids*.

[37] Gourdain, N., Gicquel, L., and Collado, E. (2012). Comparison of rans and les for prediction of wall heat transfer in a highly loaded turbine guide vane. *J. Propuls. Power*.

[38] Gourdain, N., Sicot, F., Duchaine, F., and Gicquel, L. (2014). Large eddy simulation of flows in industrial compressors: a path from 2015 to 2035. *Phil. Trans. R. Soc. A*.

[39] Gullbrand, J. and Chow, F. K. (2002). Investigation of numerical errors, subfilter-scale models, and subgrid-scale models in turbulent channel flow simulations. *Annual Research Brief (Center for Turbulence Research)*.

[40] Hammer, F., Sandham, N. D., and Sandberg, R. D. (2018). The influence of different wake profiles on losses in a low pressure turbine cascade. *Int. J. Turbomach. Propuls. Power*.

[41] Henderson, A. D., Walker, G. J., and Hughes, J. D. (2008). Unsteady transition phenomena at a compressor blade leading stage. *ASME J. Turbomach.*

[42] Hilgenfeld, L. and Pfitzner, M. (2004). Unsteady boundary layer development due to wake passing effects on a highly loaded linear compressor cascade. *ASME J. Turbomach.*

[43] Hodson, H. P. (1998). Blade row interaction in low pressure turbines. *Blade row interference in axial turbomachinery stages, VKI Lecture Series*.

[44] Hodson, H. P. and Howell, R. J. (2005). Blade row interactions, transition, and high-lift aerofoils in low-pressure turbines. *Annu. Rev. Fluid Mech.*

[45] Hosseini, S. M., Simoni, D., and Hanifi, A. (2015). Direct numerical simulation of flow around a turbine blade: A transitional study. *Internal report.*

[46] Jee, S., Joo, J., and Medic, G. (2016). Large–eddy simulation of a high–pressure turbine vane with inlet turbulence. *Proceedings of the ASME Turbo Expo.*

[47] Kennedy, C. A. and Gruber, A. (2008). Reduced aliasing formulations of the convective terms within the navier–stokes equations for a compressible fluid. *Journal of Computational Physics.*

[48] Kim, J., Parviz, M., and Moser, R. (1987). Turbulence statistics in fully developed channel flow at low reynolds number. *J. Fluid Mech.*

[49] Klein, M. (2005). An attempt to assess the quality of large eddy simulations in the context of implicit filtering. *Flow, Turbul. Combust.*

[50] Koschichow, D., Fröhlich, J., Kirik, I., and Niehuis, R. (2014). Dns of the flow near the endwall in a linear low pressure turbine cascade with periodically passing wakes. *Proceedings of ASME Turbo Expo.*

[51] Lamb, H. (1945). *Hydrodynamics, 6th ed.* Dover Publications.

[52] Lardeau, S., Leschziner, M., and Zaki, T. (2012). Large eddy simulation of transitional separated flow over a flat plate and a compressor blade. *Flow Turbul. Combust.*

[53] Laskowski, G. M., Kopriva, J., Michelassi, V., Shankaran, S., Paliath, U., Bhaskaran, R., Wang, Q., Talnikar, C., Wang, Z. J., and Jia, F. (2016). Future directions of high fidelity cfd for aerothermal turbomachinery analysis and design. *46th AIAA Fluid Dynamics Conference.*

[54] Leggett, J., Priebe, S., Shabbir, A., Michelassi, V., Sandberg, R., and Richardson, E. (2018). Loss prediction in an axial compressor cascade at off-design incidences with free stream disturbances using large eddy simulation. *ASME J. Turbomach.*

[55] Lei, V. M., Spakovszky, Z. S., and Greitzer, E. M. (2008). A criterion for axial compressor hub-corner stall. *ASME J. Turbomach.*

[56] Marconcini, M., Pacciani, R., Arnone, A., Michelassi, V., Pichler, R., Zhao, Y., and Sandberg, R. D. (2018). Les and rans analysis of the end-wall flow in a linear lpt cascade with variable inlet conditions, part ii: Loss generation. *Proceedings of ASME Turbo Expo.*

[57] Matsubara, M. and Andersson, P. H. (2001). Disturbance growth in boundary layers subjected to free-stream turbulence. *Physics of Fluids.*

[58] Mayle, R. E. (1991). The role of laminar-turbulent transition in gas turbine engines. *ASM. J. Turbomach.*

[59] McKenzie, A. B. (1997). *Axial Flow Fans and Compressors: Aerodynamic Design and Performance*. Ashgate Publishing.

[60] McMullan, W. and Page, G. (2011). Large eddy simulation of a controlled diffusion compressor cascade. *Flow Turbul. Combust.*

[61] Medic, G. and Sharma, O. (2012). Large-eddy simulation of flow in a low-pressure turbine cascade. *ASME. J. Turbomach.*

[62] Michelassi, V. (2015). Modeling and resolving turbulence in turbomachinery flows. *Tutorial at 2015 ASME Turbo Expo*.

[63] Michelassi, V., Chen, L., Pichler, R., and Sandberg, R. D. (2015). Compressible direct numerical simulation of low-pressure turbines—part ii: Effect of inflow disturbances. *ASME J. Turbomach.*

[64] Michelassi, V., Chen, L., Pichler, R., Sandberg, R. D., and Bhaskaran, R. (2016). High-fidelity simulations of low-pressure turbines: Effect of flow coefficient and reduced frequency on losses. *ASME J. Turbomach.*

[65] Michelassi, V., Wissink, J., Fröhlich, J., and Rodi, W. (2003a). Large-eddy simulation of flow around low-pressure turbine blade with incoming wakes. *AIAA Journal*.

[66] Michelassi, V., Wissink, J., and Rodi, W. (2003b). Direct numerical simulation, large eddy simulation and unsteady reynolds-averaged navier–stokes simulations of periodic unsteady flow in a low-pressure turbine cascade: a comparison. *J. Power and Energy*.

[67] Michelassi, V. and Wissink, J. G. (2015). Turbulent kinetic energy production in the vane of a low-pressure linear cascade with incoming wakes. *International J. of Rotating Machinery*.

[68] Moin, P. (2014). Progress and challenges in numerical simulation of multi-physics turbulent flows in aerospace applications. *Presentation at Royal Academy of Engineering*.

[69] Montomoli, F., Naylor, E., Hodson, H. P., and Lapworth, L. (2013). Unsteady effects in axial compressors: A multistage simulation. *Journal of Propulsion and Power*.

[70] Mortensen, M. and Langtangen, H. P. (2016). High performance python for direct numerical simulations of turbulent flows. *Computer Physics Communications*.

[71] Nagabhushana Rao, V., Jefferson-Loveday, R., Tucker, P., and Lardeau, S. (2014). Large eddy simulations in turbines: Influence of roughness and free-stream turbulence. *Flow Turbul. Combust.*

[72] Nagabhushana Rao, V., Tucker, P. G., Jefferson-Loveday, R. J., and Coull, J. D. (2013). Large eddy simulations in low-pressure turbines: Effect of wakes at elevated free-stream turbulence. *International Journal of Heat and Fluid Flow*.

[73] Nolan, S. P. R., Botros, B. B., Tan, C. S., Adamczyk, J. J., Greitzer, E. M., and Gorrell, S. E. (2011). Effects of upstream wake phasing on transonic axial compressor performance. *ASME. J. Turbomach.*

[74] Odier, N., Sanjose, M., Gicquel, L., Poinsot, T., Moreau, S., and Duchaine, F. (2019). A characteristic inlet boundary condition for compressible, turbulent, multispecies turbomachinery flows. *Computers and Fluids.*

[75] Papadogiannis, D., Duchaine, F., Sicot, F., Gicquel, L., Wang, G., and Moreau, S. (2014). Large eddy simulation of a high pressure turbine stage: effects of sub-grid scale modeling and mesh resolution. *In Proceedings of the ASME Turbo Expo.*

[76] Phillips, L. and Fyfe, D. (2011). Turbid: a routine for generating random turbulence inflow data. Technical report, Naval Research Laboratory.

[77] Pichler, R., Kopriva, J., Laskowsi, G., Michelassi, V., and Sandberg, R. (2017). High-fidelity simulations of a linear hpt vane cascade subject to varying inlet turbulence. *In Proceedings of the ASME Turbo Expo.*

[78] Pichler, R., Kopriva, J., Laskowski, G., Michelassi, V., and Sandberg, R. D. (2016a). Highly resolved les of a linear hpt vane cascade using structured and unstructured codes. *Proceedings of ASME Turbo Expo.*

[79] Pichler, R., Michelassi, V., Sandberg, R., and Ong, J. (2018a). Highly resolved les study of gap size effect on low-pressure turbine stage. *ASME. J. Turbomach.*

[80] Pichler, R., Sandberg, R. D., and Michelassi, V. (2016b). Assessment of grid resolution requirements for accurate simulation of disparate scales of turbulent flow in low-pressure turbines. *Proceedings of ASME Turbo Expo.*

[81] Pichler, R., Zhao, Y., Sandberg, R. D., Michelassi, V., Pacciani, R., Marconcini, M., and Arnone, A. (2018b). Les and rans analysis of the end-wall flow in a linear lpt cascade with variable inlet conditions, part i: Flow and secondary vorticity fields. *Proceedings of ASME Turbo Expo.*

[82] Poinsot, T. J. and Lele, S. K. (1992). Boundary conditions for direct ssimulation of compressible viscous flows. *J. Comput. Phys.*

[83] Przytarski, P. and Wheeler, A. P. S. (2018). Accurate prediction of loss using high fidelity methods. *Proceedings of ASME Turbo Expo.*

[84] Pulliam, T. H. and Steger, J. L. (1978). On implicit finite-difference simulations of three-dimensional flow. *AIAA Journal.*

[85] Raverdy, B., Mary, I., Sagaut, P., and Liamis, N. (2003). High-resolution large-eddy simulation of flow around low-pressure turbine blade. *AIAA Journal.*

[86] Rezaeiravesh, S. and Liefvendahl, M. (2018). Effect of grid resolution on large eddy simulation of wall-bounded turbulence. *Physics of Fluids.*

[87] Sandberg, R. D. and Michelassi, V. (2019). The current state of high-fidelity simulations for main gas path turbomachinery components and their industrial impact. *Flow, Turbul. Combust.*

[88] Sandberg, R. D., Michelassi, V., Pichler, R., Chen, L., and Johnstone, R. (2015). Compressible direct numerical simulation of low-pressure turbines—part i: Methodology. *ASME J. Turbomach.*

[89] Sarkar, S. (2009). Influence of wake structure on unsteady flow in a low pressure turbine blade passage. *ASME. J. Turbomach.*

[90] Scillitoe, A. (2017). Towards predictive eddy resolving simulations for gas turbine compressors. *PhD Thesis, University of Cambridge*.

[91] Scillitoe, A., Tucker, P., and Adami, P. (2017a). Large eddy simulation of boundary layer transition mechanisms in a gas-turbine compressor cascade. *ASME J. Turbomachinery*.

[92] Scillitoe, A., Tucker, P., and Adami, P. (2017b). Numerical investigation of three-dimensional separation in an axial flow compressor: the influence of freestream turbulence intensity and endwall boundary layer state. *ASME J. Turbomachinery*.

[93] Segui, L., Gicquel, L., Duchaine, F., and de Laborderie, J. (2017). Les of the ls89 cascade: Influence of inflow turbulence on the flow prediction. *In Proceedings of the 12th European Conference on Turbomachinery Fluid Dynamics and Thermodynamics*.

[94] Slotnick, J., Khodadoust, A., Alonso, J., Darmofal, D., Gropp, W., Lurie, E., and Mavriplis, D. (2014). Cfd vision 2030 study: A path to revolutionary computational aerosciences. *Technical Report March, NASA, Langley Research Center*.

[95] Smith, L. H. (1966). Wake dispersion in turbomachines. *ASME Transactions, J. Basic Engineering*.

[96] Souza, L. F., Mendonca, M. T., and Medeiros, A. F. (2005). The advantages of using high-order finite differences schemes in laminar-turbulent transition studies. *Int. J. Numer. Meth. Fluids*.

[97] Stieger, R. D. and Hodson, H. P. (2005). The unsteady development of a turbulent wake through a downstream low-pressure turbine blade passage. *ASME J. Turbomach.*

[98] Sutera, S. P., Maeder, P. F., and Kestin, J. (1963). On the sensitivity of heat transfer in the stagnation-point boundary layer to free-stream vorticity. *J. Fluid Mech.*

[99] Tam, C. K. W. and Webb, J. C. (1993). Dispersion-relation-preserving finite difference schemes for computational aeroacoustics. *J. Comput. Phys.*

[100] Thomas, P. D. and Lombard, C. K. (1979). Geometric conservation law and its application to flow computations on moving grids. *AIAA Journal*.

[101] To, H. and Miller, R. J. (2015). The effect of aspect ratio on compressor performance. *ASME J. Turbomach.*

[102] Tucker, P. (2011). Computation of unsteady turbomachinery flows: Part 1–progress and challenges. *Prog. Aerosp. Sci*.

[103] Tucker, P. (2013). Trends in turbomachinery turbulence treatments. *Prog. Aerosp. Sci.*

[104] Tyacke, J., Vadlamani, N. R., Trojak, W., Watson, R., Ma, Y., and Tucker, P. G. (2019). Turbomachinery simulation challenges and the future. *Progress in Aerospace Sciences.*

[105] US Dept. of Energy, A. S. C. A. C. S. o. e. C. (2010). The opportunities and challenges of exascale computing. *http://science.energy.gov/ascr/ascac/.*

[106] van Rees, M., Leonard, A., Pullin, D. I., and Koumoutsakos, P. (2011). A comparison of vortex and pseudo-spectral methods for the simulation of periodic vortical flows at high reynolds number. *J. Comput. Phys.*

[107] Van Zante, D., Adamczyk, J. J., Strazisar, A. J., and Okiishi, T. H. (2002). Wake recovery performance benefit in a high-speed axial compressor. *ASME J. Turbomach.*

[108] Wang, Z. J., Fidkowski, K., Abgrall, R., Bassi, F., Caraeni, D., Cary, A., Deconinck, H., Hartmann, R., Hillewaert, K., Huynh, H. T., Kroll, N., May, G., Persson, P. O., van Leer, B., and Visbal, M. (2012). High-order cfd methods: Current status and perspective. *Int. J. Numer. Meth. Fluids.*

[109] Wheeler, A. and Sandberg, R. (2016). Numerical investigation of the flow over a model transonic turbine blade tip. *J. Fluid Mech.*

[110] Wheeler, A., Sandberg, R., Sandham, N., Pichler, R., Michelassi, V., and Laskowski, G. (2016). Direct numerical simulations of high-pressure turbine vane. *J. Turbomach.*

[111] Wheeler, A. P., Miller, R. J., and Hodson, H. P. (2007). The effect of wake induced coherent structures on compressor boundary layers. *ASME J. Turbomach.*

[112] Wheeler, A. P., Sofia, A., and Miller, R. J. (2009). The effect of leading-edge geometry on wake interactions in compressors. *ASME J. Turbomach.*

[113] Wheeler, A. P. S., Dickens, A. M. J., and Miller, R. J. (2018). The effect of non-equilibrium boundary layers on compressor performance. *ASME J. Turbomach.*

[114] Wissink, J., Zaki, T., Rodi, W., and Durbin, P. (2014). The effect of wake turbulence intensity on transition in a compressor cascade. *Flow Turbul. Combust.*

[115] Wissink, J. G. (2003). Dns of separating, low reynolds number flow in a turbine cascade with incoming wakes. *Journal of Heat and Fluid Flow.*

[116] Wissink, J. G. and Rodi, W. (2006). Direct numerical simulation of transitional flows in turbomachinery. *ASME J. Turbomach.*

[117] Wissink, J. G., Rodi, W., and Hodson, H. (2006). Influence of disturbances carried by periodically incoming wakes on the separating flow around a turbine blade. *Int. J. Heat Fluid Flow.*

[118] Wu, X. and Durbin, P. A. (2000). Boundary layer transition induced by periodic wakes. *ASME J. Turbomach.*

[119] Wu, X. and Durbin, P. A. (2001). Evidence of longitudinal vortices evolved from distorted wakes in a turbine passage. *J. Fluid Mech.*

[120] Wu, X., Jacobs, R. G., Hunt, J. C. R., and Durbin, P. A. (1999). Simulation of boundary layer transition induced by periperiodic passing wakes. *J. Fluid Mech.*

[121] You, D., Wang, M., Moin, P., and Mittal, R. (2006). Effects of tip-gap size on the tip-leakage flow in a turbomachinery cascade. *Physics of Fluids.*

[122] You, D., Wang, M., Moin, P., and Mittal, R. (2007). Large-eddy simulation analysis of mechanisms for viscous losses in a turbomachinery tip-clearance flow. *J. Fluid Mech.*

[123] Yu, R. (2016). Introduction of compressible turbulence. *www.fm.energy.lth.se/fileadmin/fm/Education/Courses/CFD/turb_modeling2_2016.pdf.*

[124] Zaki, T. A., Durbin, P. A., Wissink, J., and Rodi, W. (2006a). Direct numerical simulation of bypass and separation induced transition in a linear compressor cascade. *Proceedings of ASME Turbo Expo.*

[125] Zaki, T. A., Durbin, P. A., and Wu, X. (2006b). Separation and transition to turbulence in a compressor passage. *Center for Turbulence Research Proceedings of the Summer Program.*

[126] Zaki, T. A., Wissink, J. G., Durbin, P. A., and Rodi, W. (2009). Direct computations of boundary layers distorted by migrating wakes in a linear compressor cascade. *Flow, Turbulence and Combustion.*

[127] Zaki, T. A., Wissink, J. G., Rodi, W., and Durbin, P. A. (2010). Direct numerical simulation of transition in a compressor cascade: the influence of free-stream turbulence. *J. Fluid. Mech.*

[128] Zang, T. A., Krist, S. E., and Hussaini, M. Y. (1989). Resolution requirements for numerical simulations of transition. *Journal of Scientific Computing.*

[129] Zhang, W., Zou, Z., Qi, L., Ye, J., and Wang, L. (2015). Effects of freestream turbulence on separated boundary layer in a low-re high-lift lp turbine blade. *Comput. Fluids.*

[130] Zhao, Y. and Sandberg, R. (2020). Bypass transition in boundary layers subject to strong pressure gradients and curvature effects. *J. Fluid Mech.*

Appendix A

A.1 Double decomposition of kinetic energy

The flow is decomposed using classical Reynolds decomposition into mean and fluctuating components:

$$f = \bar{f} + f' \tag{A.1}$$

For the purpose of the decomposition, all quantities are Favre averaged:

$$\bar{f} \equiv \frac{\overline{\rho f}}{\bar{\rho}} \tag{A.2}$$

leading to the following set of compressible kinetic energy equations for mean (m) and fluctuating turbulent (f) fields (full derivation available e.g. at [123]):

$$\begin{aligned}\underbrace{\frac{\bar{D}}{Dt}\left(\bar{\rho}\frac{1}{2}\bar{u_i}\bar{u_i}\right)}_{c_m} =& \underbrace{-\left(-\overline{\rho u_i' u_j'}\frac{\partial \bar{u_i}}{\partial x_j}\right)}_{t_{mf}} - \underbrace{\frac{\partial}{\partial x_j}\left[\bar{u_i}\left(\overline{\rho u_i' u_j'}\right)\right]}_{d_m} \\ &+ \underbrace{\frac{\partial \bar{\tau_{ij}}\bar{u_i}}{\partial x_j}}_{v.d._m} - \underbrace{\bar{\tau_{ij}}\frac{\partial \bar{u_i}}{\partial x_j}}_{\phi_m} - \underbrace{\bar{u_i}\frac{\partial \bar{p}}{\partial x_i}}_{p.w._m}\end{aligned} \tag{A.3a}$$

$$\begin{aligned}\underbrace{\frac{\bar{D}}{Dt}\left(\bar{\rho}\frac{1}{2}\overline{u_i' u_i'}\right)}_{c_f} =& \underbrace{+\left(-\overline{\rho u_i' u_j'}\frac{\partial \bar{u_i}}{\partial x_j}\right)}_{t_{mf}} - \underbrace{\frac{\partial}{\partial x_j}\left[\overline{\rho u_j'\left(\frac{1}{2}u_i' u_i'\right)}\right]}_{d_f} \\ &+ \underbrace{\frac{\partial \overline{\tau_{ij}' u_i'}}{\partial x_j}}_{v.d._f} - \underbrace{\overline{\tau_{ij}'\frac{\partial u_i'}{\partial x_j}}}_{\phi_f} - \underbrace{\bar{u_i'}\frac{\partial \bar{p}}{\partial x_i}}_{p.w._f} - \underbrace{\frac{\partial \overline{p' u_i'}}{\partial x_i}}_{p.d_f} + \underbrace{\overline{p'\frac{\partial u_i'}{\partial x_i}}}_{p.l._f}\end{aligned} \tag{A.3b}$$

where

$$\frac{\bar{D}}{Dt} \equiv \frac{\partial}{\partial t} + \bar{u_j}\frac{\partial}{\partial x_j} \tag{A.4}$$

and

c - convection of kinetic energy

t - energy transfer between mean and fluctuating flowfield

d - diffusion due to unsteadiness

$v.d.$ - viscous diffusion

ϕ - viscous dissipation

$p.w.$ - pressure work

$p.d.$ - pressure diffusion

$p.l.$ - pressure dilation

Energy transfer term t is also commonly refereed to as turbulence production as it most often represents the extraction of energy from the mean to fluctuating flowfield. To quantify each of these terms all the quantities in Equations A.3a and A.3b were integrated in volume, Ω, from the inlet of the domain to the sampling plane. The integrated quantities are capitalized, for instance the integrated dissipation is:

$$\Phi = \int_{\Omega} \phi d\Omega \tag{A.5}$$

Due to their negligible impact pressure dilation and pressure diffusion terms were ignored for the turbulent kinetic energy budget. Tables A.1 and A.2 show Reynolds decomposed energy budget computed for the repeating passage model flowfield with three axial gaps.

Table A.1 shows that mean kinetic energy budgets is satisfied. For turbulent kinetic energy budget the balance was achieved when artificial dissipation due to filtering, ϵ_N was added to the resolved dissipation, Table A.2.

Interestingly, the turbulent kinetic budget shows that integrated turbulent dissipation (resolved+artificial) and energy transfer term are of different magnitude and have opposite trends, Figure A.1. This is a consequence of using classical Reynolds decomposition which treats periodic oscillations and turbulent fluctuations together. To be able to distinguish turbulence fluctuations from organised (oscillating) motion of the wake, Hussain and Reynolds [29] proposed a triple decomposition of the velocity field. This decomposition is was used in Chapter 6 to study energy transfers in more detail.

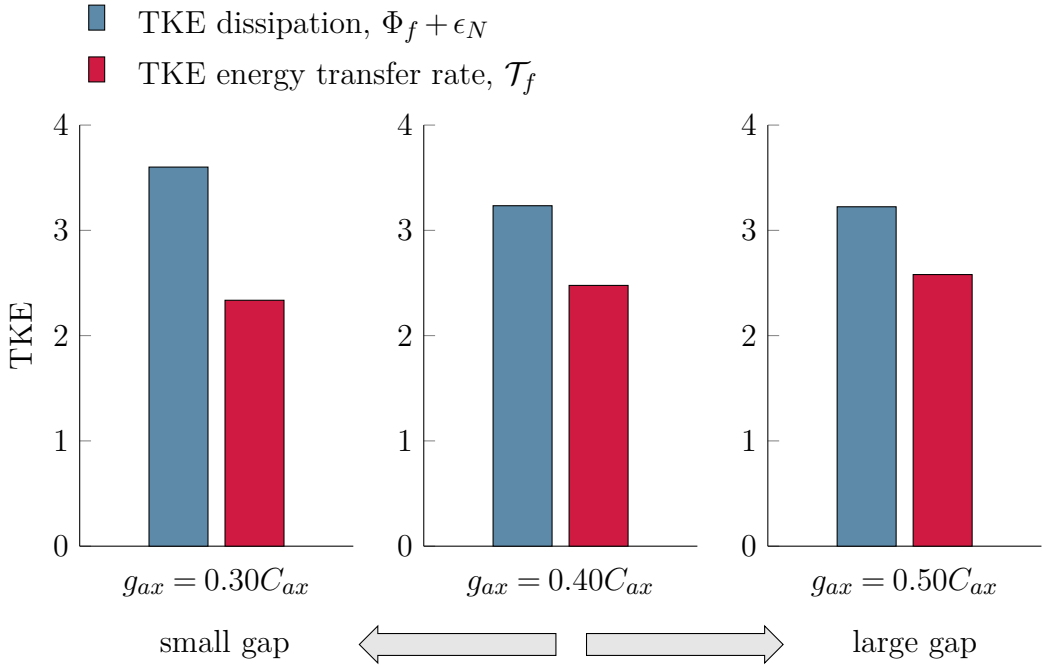

Figure A.1: The comparison of integrated turbulent dissipation ($\Phi_f + \epsilon_N$) and energy transfer term ($\mathcal{T}_{mf}$) for three considered gaps.

Table A.1: Double decomposition - mean kinetic energy budget

Eq. A.3a	$C_m = -\mathcal{T}_{mf} - D_m + V.D._m - \Phi_m - P.W._m$		
	$g_{ax} = 0.30C_{ax}$	$g_{ax} = 0.40C_{ax}$	$g_{ax} = 0.50C_{ax}$
C_m	-107.716	-109.583	-109.977
$\mathcal{T}_{mf}$	2.336	2.477	2.580
D_m	-3.982	-2.549	-2.075
$V.D._m$	0.012	0.013	0.014
Φ_m	3.419	3.472	3.554
$P.W._m$	105.906	106.287	105.678
NET	0.048	-0.091	0.253

Table A.2: Double decomposition - turbulent kinetic energy budget

Eq. A.3b	$C_f = \mathcal{T}_{mf} - D_f + V.D._f - \Phi_f - P.W._f - P.D._f + P.L._f$		
	$g_{ax} = 0.30C_{ax}$	$g_{ax} = 0.40C_{ax}$	$g_{ax} = 0.50C_{ax}$
C_f	2.105	1.527	1.248
$\mathcal{T}_{mf}$	2.336	2.477	2.580
D_f	0.716	0.649	0.518
$V.D._f$	0.007	0.006	0.006
$\Phi_f + \epsilon_N$	2.926 + 0.675	2.624 + 0.610	2.563 + 0.661
$P.W._f$	–	–	–
$P.D._f$	-0.078	-0.052	-0.019
$P.L._f$	–	–	–
NET	0.053	0.074	0.073